Study of lepton flavor violation with a high-resolution tracking device for Belle II experiment

Dong Van Thanh

Doctor of Philosophy

Department of Particle and Nuclear Physics
School of High Energy Accelerator Science
SOKENDAI (The Graduate University for Advanced Studies)

SOKENDAI (THE GRADUATE UNIVERSITY FOR ADVANCED STUDIES)

Study of lepton flavor violation with a high-resolution tracking device for Belle II experiment

by

Dong Van Thanh

A thesis submitted in partial fulfillment for the degree of Doctor of Philosophy

in the

Department of Particle and Nuclear Physics

School of High Energy Accelerator Science

Advisor: Prof. Dr. Shoji Uno

June 2018

Acknowledgements

Firstly, I would like to express my sincere gratitude to my advisor Prof. Shoji Uno for his patient guidance, enthusiastic encouragement of this PhD research as well as his help with my life in Japan; and Dr. Makoto Uchida (Tokyo Tech.) for his assistance with my works since my first day in the central drift chamber (CDC) group until now.

I would also like to thank Dr. Hitoshi Ozaki for his valuable and constructive suggestions; Dr. Sadaharu Uehara for his kindly help in revising of my thesis; other memebers of the CDC group for their support: Dr. Nanae Taniguchi, Prof. Eiichi Nakano and Assoc. Prof. Karim Trabelsi. I would also extend my thanks to Nils Braun and Thomas Hauth for their helps in using of tracking software; and members of my committee for spending their time to read my thesis and for their constructive comments.

My grateful thanks are also extended to KEK staffs and friends in the Belle II collaborator. Especially, I want to thank Dr. Hulya Amatan for her help and her encouragement; staffs of KEK SOKENDAI office for their support during my PhD research at KEK.

Finally, I wish to thank my family and my friends in Vietnam for their encouragement throughout this three years.

Contents

List of Figures

List of Tables

Abbreviations

IP	**I**nteraction **P**oint
VXD	**V**erte**x** **D**etector
PXD	**P**i**X**el **D**etector.
SVD	**S**ilicon **V**ertex **D**etector
CDC	**C**entral **D**rift **C**hamber
ECL	**E**lectromagnetic **C**a**L**orimeter
TOP	**T**ime **O**f **P**ropagation counter
ARICH	**A**erogel **R**ing **I**maging **CH**erenkov counter
KLM	**KL**ong and **M**uon detector
PID	**P**article **ID**entification detector

Introduction

In the 20^{th} century, after many elementary particles and new phenomena are discovered, scientists have built a set of very successful models to describe elementary particles and interactions among them, which is well known as the Standard Model of elementary particles (SM). Its validity was confirmed by many discoveries of predicted particles during the several decades. In 2012, after the many years to hunt for the last important piece of the SM, Higgs boson was found by ATLAS and CMS experiments at the LHC collider [6, 7].

The SM has successfully explained or predicted many phenomena of the particle physics. Despite its enormous successes, however, the SM is still incomplete theory. One obvious thing is the fact that the gravity, one of the four natural forces, is not included. There are still many remaining questions which cannot be explained by the SM such as the dominance of matter in the universe cannot be explained only by the current observed CP-violation sources, the existence of dark matter which is conjectured by astronomical observations. To explain such problems, many extensions of the SM such as Super-Symmetry (SUSY) are suggested.

Moreover, neutrino oscillation was discovered by Kamiokande collaboration in 1998 [8]. It is the phenomenon that the neutrino flavors change among them during the propagation. This discovery leads to new questions of the neutrino mass and possible of flavor changing phenomenon in the charged lepton sector. For the charged lepton, the expected branching fraction of lepton flavor violation

(LFV) decays predicted by the SM is very small, but in the extensions of the SM [9–11], they are predicted to be large and detectable with the current and planned experiments. Therefore an observation of an LFV decay will provide a clear signature for new physics.

Belle II is an upgrade of the Belle experiment at the SuperKEKB accelerator at High Energy Accelerator Organization (KEK) Tsukuba, Japan to search for new physics in rare and forbidden decays in the SM and to hunt new particles such as dark photon. For those purposes, Belle II is designed to be operated at 40 times higher luminosity, and expected to accumulate a 50 times higher integrated luminosity comparing with the existent record at Belle. Although SuperKEKB is designed mainly for producing $B\bar{B}$ meson, $\tau^+\tau^-$ pair is produced with almost the same rate. Hence, the Belle II experiment will provide a very good opportunity to search for LFV in decays of τ. In such an LFV search, the resolutions of reconstructed mass and energy of τ which are measured by tracking detectors are important keys for reducing backgrounds. They are also important in analysis for other physics.

This thesis presents a study of Lepton Flavor Violation in the decay $\tau^- \to \mu^-\mu^+\mu^-$ with a high-resolution tracking device for the Belle II experiment. We have made efforts to develop calibration and alignment procedures for the central tracking device of the Belle II detector, Central Drift Chamber (CDC). The LFV study is performed assuming a 1 ab^{-1} data sample (equivalent to the accumulated data of Belle). Thesis is organized as follows:

- **Chapter 1:** Physics and experimental motivations of lepton flavor violation searches are presented.
- **Chapter 2:** The SuperKEKB accelerator and the Belle II detector are introduced briefly.

- **Chapter 3:** Structure, calibration and alignment procedures of the CDC are described in detail.
- **Chapter 4 and 5:** An LFV analysis of the decay $\tau \to \mu^-\mu^+\mu^-$ with 1 ab^{-1} MC sample is demonstrated.
- **Chapter 5:** Conclusion of this thesis is presented.

Chapter 1

Lepton Flavor Violation

1.1 The Standard Model and Lepton Flavor Violation

The standard model of elementary particles was developed in the 1970's to describe the known constituents of matter and interactions among them. All matter is constructed from a small number of elements with a spin 1/2 called fermions. They are classified into two groups: 6 flavors of quarks and 6 flavors of leptons. The interactions between them are modeled by quantum field theory, in which forces are mediated by bosons with a spin 1, that is, photon (γ) for the electromagnetic interaction, $W^{\pm}$ and Z^0 for the weak interaction and gluons for the strong interaction.

According to Noether's theorem, every symmetry of the action of a physical system has a corresponding conservation law. For instance, the invariance with respect to the time translation corresponds to the well-known law of energy conservation. Lepton number and lepton flavor conservation, however, have no corresponding symmetry [12]; they have been introduced to explain the known

absence of reactions and decays such as

$$\bar{\nu} + p \rightarrow n + e^{+} \tag{1.1}$$

happen, while a reaction

$$\bar{\nu} + n \rightarrow p + e^{-} \tag{1.2}$$

and a decay

$$\tau \rightarrow \mu + \gamma \tag{1.3}$$

have not been observed.

The SM is constructed with an assumption that the neutrinos are massless. However, neutrino oscillation has been observed by Sudbury Neutrino Observatory (SNO) [13] and Super-Kamiokande collaborations [8]. The observations have proved that neutrinos have mass, and magnitude of the oscillation depends on the mass difference between their flavors. Therefore, neutrino masses are physical quantities which can still be a challenge of measurement.

The existence of a neutrino mass leads to a possibility to change flavors of the charged leptons. The process is expected to be the same as flavor-changing neutral currents (FCNC) in the quark sector. Feynman diagram for the decay of τ is given in Figure 1.1. The process, however, is suppressed by Glashow-Iliopoulos-Maiani (GIM) factor, $(\Delta M_\nu / M_W)^4$ [14], where ΔM_ν is the mass difference of the neutrino flavors. The predicted branching fraction of the process is less than 10^{-40}. Another type of Feynman diagram for the decay $\tau^- \rightarrow \mu^- \mu^+ \mu^-$ is shown in Figure 1.2. This type of the process is not strongly suppressed by GIM factor; it is proportional to $\log(\mathrm{M}_\nu^2/\mathrm{M}_\mathrm{W}^2)$, nevertheless the branching fraction $\sim 10^{-14}$ [14] is still inaccessible with current experiments.

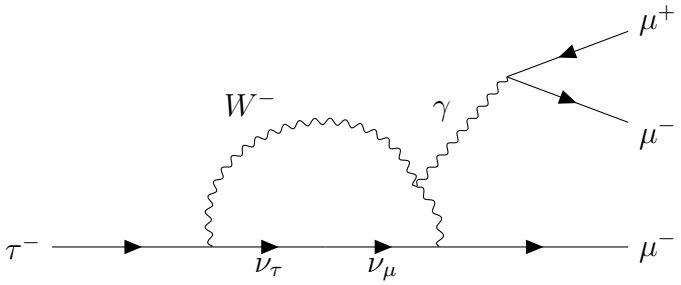

Figure 1.1: Feynman diagram for the $\tau^- \to \mu^-\mu^+\mu^-$ LFV decay through $\nu_\tau \to \nu_\mu$ oscillation.

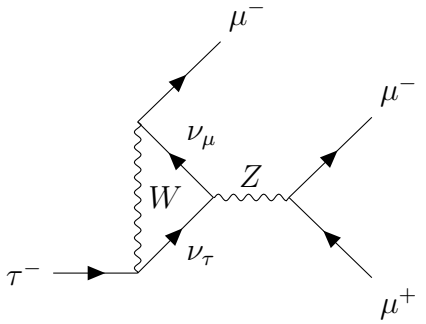

Figure 1.2: One-loop flavor changing decay for $\tau^- \to \mu^-\mu^+\mu^-$

1.2 Lepton Flavor Violation Beyond the Standard Model

Many extensions of the SM are proposed in order to solve the remaining problems which are unable to explain within the SM. For instance, the Super-symmetry (SUSY) theory with seesaw mechanism is suggested to explain the tiny mass of neutrinos. Most of them naturally introduce LFV decays with the order which can be reached in the current and future-planned experiments.

Strength of interactions related to new-physics phenomena is naively expected to be mass-dependent. Hence decays of τ have an advantage in the LFV searches. Moreover, as lepton decays are not strongly affected by uncertainties from hadronic interaction, they will allow a clear distinction of new physics scenarios. In particularly, if several branching fractions are determined, the model for new physics could be clearly distinguished.

Among many LFV decays of τ, two kinds of decays $\tau \to lll$ and $\tau \to l\gamma$ are expected to be the most sensitive to new physics with a larger branching fraction than the other decays. When the decays $\tau \to lll$ are mediated by a photon exchange, their branching fraction might be smaller than that of the decays $\tau \to l\gamma$ with a factor $1/\alpha$, because of the second vertex for a pair production ($\gamma \to ll$). In contrast, if the $\tau \to lll$ decays are mediated by a new heavy particle, its branching fraction can be larger than that of $\tau \to l\gamma$.

The SUSY is the most popular extension of the SM. The symmetry between the bosons and fermions is proposed, there, and the numbers of fermions and of bosons are the same in natural. Each fermion has a SUSY boson partner and vice versa. For example, the super-partner of electron is scalar electron called selectron. Even though no any supersymmetric particles have been found yet, this theory is still very attractive because many problems of particle physics such as the hierarchy and gauge unification problems can be solved in its context.

In the SUSY, the tiny mass of neutrino is explained by seesaw mechanism. The right-handed neutrinos are introduced, which are super heavy so that they have not been seen in experiments; the right-handed neutrino mass is $\sim 10^{14}$ GeV. The decay $\tau^- \to \mu^-\mu^+\mu^-$ via an exchange of Higgs bosons within the SUSY context and seesaw mechanism has been demonstrated by Babu and Kolada [9]. The branching fraction is predicted proportional to $\tan^6\beta$, ($\tan\beta = \langle \mathrm{H_u} \rangle \,/\, \langle \mathrm{H_d} \rangle$, the ratio of the two vacuum expectation values for the two neutral Higgs boson). The Feynman diagram for this process is shown in Figure 1.3. The branching fraction of the process depends on several parameters, and Eq. 1.4 is the prediction of the branching fraction based on a specific assumption. The detailed description of the assumption of parameters and the calculation can be found in the article [9].

$$\mathcal{B}\mathrm{r}(\tau \to \mu\mu\mu) \simeq \left(1 \times 10^{-7}\right) \times \left(\frac{\tan\beta}{60}\right)^6 \times \left(\frac{100\ \mathrm{GeV}}{\mathrm{m_A}}\right)^4, \qquad (1.4)$$

where M_A is mass of the SUSY Higgs.

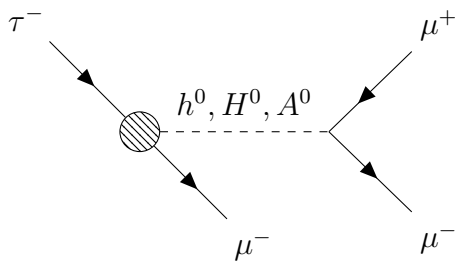

Figure 1.3: Feynman diagram which contributes to the $\tau \to \mu\mu\mu$ decay.

There are many other well-motivated physics models which predict a large branching fraction for LFV, such as the decay via Non-universal boson Z' [11] and the standard model with presence of the 4^{th} generation [10]. Some of the largest predicted branching fractions from different theories are summarized in Table 1.1.

Table 1.1: The largest predicted branching fractions for the decays $\tau \to \mu\gamma$ and $\tau \to \mu\mu\mu$ from different theories.

Model	$\mathcal{B}(\tau \to \mu\gamma)$	$\mathcal{B}(\tau \to 3\mu)$	Reference
SM + ν mixing	$< 10^{-40}$	10^{-14}	[14]
SM + heavy Majorana ν_R	10^{-9}	10^{-10}	[15]
Non-universal Z'	10^{-9}	10^{-8}	[11]
SUSY + seesaw (mediated by Higgs)	10^{-10}	10^{-7}	[9]
SM with 4^{th} generation	10^{-8}	10^{-8}	[10]

1.3 Previous LFV Searches for the Decay $\tau \to \mu\mu\mu$

Searching for LFV in the charged lepton sector is a very active field in particle physics. Particularly, after phase 2 of LHC, though the existence of Higgs boson is confirmed, many expected new physics candidates such as mini-blackhole and SUSY particles have not appeared [16, 17]. New hints are needed to go beyond the SM to solve remaining questions of particle physics, and thus LFV searches

are highly motivated. An observation of LFV would provide a clear signal for new physics beyond the SM. Even an improvement of the limits can constrain theoretical models in their parameters.

The LFV phenomena have been searched in many decay modes of muon and τ, and the conversion of muons to electrons in nuclear field $\mu^- + N \to e^- + N$. The LFV searches using muon has an advantage that producing a larger amount of muon is easier than that of the τ lepton, and thus experimental apparatus can be smaller than in the case of the τ lepton. On the other hand, the τ lepton belongs to the third generation, which is the heaviest lepton, and can decay to the first and second lepton generations (electron and muon) and also hadronically. Its large mass offers wide program for searching for LFV. Currently, searches for LFV through 48 channels are performed by several experiments, mostly at electron-positron colliders. The upper limits at 90% confident level are summarized by the HFLAV (Heavy Flavor Averaging) group and shown in Figure 1.4.

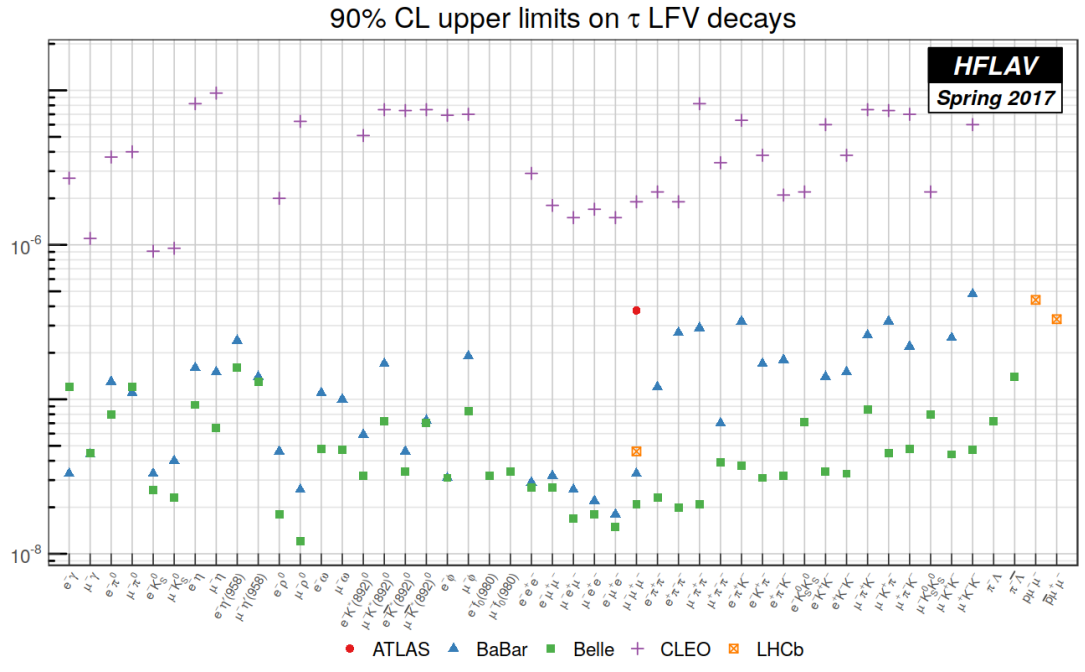

Figure 1.4: Upper-limit summary plot for τ LFV decay branching fractions taken from Ref. [1].

The most stringent upper limits of the decay $\tau^- \to \mu^-\mu^+\mu^-$ are set recently by the Belle [2] and BaBar [18] experiments. Both experiments are designed to study B physics by collisions of electrons and positrons at the resonance energy of $\Upsilon(4S)$. $\tau^+\tau^-$ pairs are produced via the process $e^+e^- \to \tau^+\tau^-(\gamma)$ with cross section of 0.919 nb.

These analyses for $\tau \to \mu\mu\mu$ are performed by selecting signal candidate events with a 1-3 topology, where one τ decays to three muons, while the other τ decays to one charged particle and one or more neutral particles. Events consisting of four well-reconstructed charged tracks with their zero net charge are selected. Particles in each selected event are then divided into two hemispheres in the e^+e^- center of mass system by the plane perpendicular to the thrust axis, that is calculated from momentum vectors of the four charged tracks and photons. The muon identification (ID) is required for all the three charged tracks at the signal 3-prong side with likelihood probability $\mathcal{P}(\mu) > 0.9$; this selection is very powerful to reject the continuum processes (pair production of u, d, s or c quark) and the generic $\tau^+\tau^-$ decay backgrounds. However, the muon-ID efficiency is low for low-momentum charged tracks because they do not reach the muon detector system which is located at the outermost of the detector system, and that leads to a low efficiency of the whole analyses. The efficiency of the analysis is 6.6% in BaBar, while in Belle, it is slightly higher, 7.6 %. The upper limits and background estimations in the experiments are summarized in Table 1.2; the results of CLEO experiment [19] is also included in the table.

The result of the analyses is obtained as two dimensions plot of $M - \Delta E$ (Belle) or $\Delta M - \Delta E$ (BaBar) variables, where M is the reconstructed invariant mass of the three charged tracks and $\Delta M = M - 1.777$ (GeV/c^2), and ΔE is the difference between the beam energy and the energy of reconstructed τ candidate in the e^+e^- center of mass system. The result of Belle experiment is shown in

Figure 1.5. The distribution has a tail for the negative ΔE because of the initial state radiation.

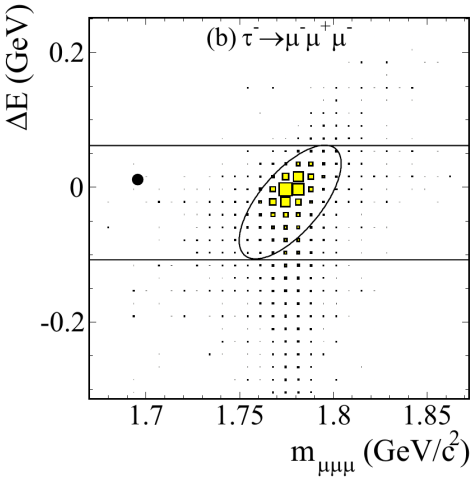

Figure 1.5: Scatter plot of $M_{\mu\mu\mu} - \Delta E$ from the Belle experiment [2]. The yellow filled boxes are MC signal distribution with an arbitrary normalization, and the closed black circle is the data. The signal yield is evaluated within the elliptical region, and the side-band region defined by the two horizontal lines excluding the signal region is used to estimate the background expected in the elliptical region.

Table 1.2: Summary results of the previous analyses

Experiment	$\mathcal{L}$	Efficiency (%)	$N_{observed}$	$N_{background}$	UL (90% C.L.)
CLEO [19]	3 fb^{-1}	15.0	0	0.11	1.9×10^{-6}
Belle [2]	782 fb^{-1}	7.6	0	0.13 ± 0.06	2.1×10^{-8}
BaBar [18]	468 fb^{-1}	6.6	0	0.44 ± 0.17	3.3×10^{-8}

The LHCb and ATLAS experiments also published their searches for LFV in the decay $\tau^- \to \mu^-\mu^+\mu^-$ in 2013 (LHCb) and 2015 (ATLAS). ATLAS performed a search using τ^- which originates from the decay $W^- \to \tau^-\bar{\nu}_\tau$, using a 20.3 fb^{-1} data sample, containing 2.41×10^9 $\tau's$, collected at 8 TeV in 2012. The efficiency of the analysis is 2.31 %. The upper limit is set by ATLAS at $\mathcal{B}(\tau \to \mu\mu\mu) < 3.76 \times 10^{-7}$ at 90% confidence level (C.L) [20]; it is one order of magnitude worse than the Belle result. The LHCb experiment has performed the search in τ from decays of beauty or charm hadrons. The full Run1 data of 3 fb^{-1}, corresponding to about 9×10^{10} $\tau's$ were used for the analysis. The upper limit is set at $\mathcal{B}(\tau \to \mu\mu\mu) < 4.6 \times 10^{-8}$ at 90% C.L. [21]: it is about 2.5 times worse

than the Belle result. The results show that e^+e^- colliding beam experiments are much more suitable for studying rare decays of τ lepton.

1.4 Motivation of this Work

Resolutions in the M and ΔE measurement are very important to define the signal region in order to reduce the background in the LFV search. They are largely affected by the momentum resolution in measurement by the tracking devices (Central Drift Chamber and Vertex Detector for the Belle II case). Therefore, efforts to develop the calibration and alignment procedures for the central tracking device are essential in order to obtain the best momentum resolution. An improvement of the momentum resolution is also benefit to other analyses.

Among many decay modes of lepton violating τ decays, the M and ΔE resolutions obtained in the decay $\tau^- \to \mu^-\mu^+\mu^-$ are the best, because other decays may contain photons or electrons in the final state. The energy resolution of a photon cluster is worse than that of the momentum determined by tracking devices. The final state radiation including bremsstrahlung also degrades the resolutions in decays to the states including an electron.

Since an improvement of the efficiency is crucial for LFV searches, the efficiency is tried to enhance by applying selection criteria mainly at the tag side, instead of applying tight cuts of muon-ID at the signal side. In addition, with a high beam-intensity environment of Belle II, beam-associated background will be drastically increased; about 20 times higher than that in Belle is expected. This huge beam background affects the tracking performance through fake, clone and background tracks which could degrade the whole analyses. A comprehensive sensitivity of the Belle II detector for a search of the decay $\tau^- \to \mu^-\mu^+\mu^-$ is performed.

Chapter 2

Belle II Experiment

The Belle II / SuperKEKB experiment is an upgrade of the successful Belle / KEKB experiment with the target total integrated luminosity 50 times higher than that achieved by the Belle experiment [3, 22]. Collecting a large number of B, D mesons and τ leptons, Belle II enables us to perform a rich physics program to search for new physics signal in CP violation, rare decay modes and decays which are forbidden in the SM of elementary particles, as well as exploration of exotic particles like four-quark state. A nano-beam scheme is employed in the SuperKEKB accelerator to obtain a 40 times higher luminosity than that of KEKB [23]. The Belle II detector is upgraded to cope with high event rates (30 kHz) under the environment of high beam-associated backgrounds and to improve measurement precisions. The collisions at the SuperKEKB accelerator started on April 26, 2018.

2.1 SuperKEKB Accelerator

The KEKB accelerator is an asymmetric electron-positron collider at KEK, Tsukuba, Ibaraki, Japan. The collider was designed for studying decays of B mesons. It was

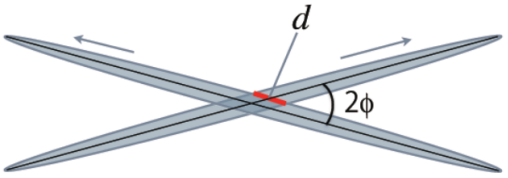

Figure 2.1: Nano-Beam scheme at collision of SuperKEKB, taken from Ref. [3].

operated at the center of mass energy around the mass of the $\Upsilon(4S)$, $\sqrt{s} \simeq 10.58$ GeV, to optimize $B\bar{B}$ meson pair production rate. To measure the time-dependent CP asymmetry, the collider had asymmetric beam energies, 8.0 GeV for the electrons and 3.5 GeV for positrons, enabling $B\bar{B}$ mesons to fly forward from the collision point.

The KEKB accelerator complex consists of a linear accelerator system and two separate storage rings for electrons and positrons. The linear accelerator has a length of about 600 meters including an extended part connected by a half-turn beam line. Each of the two rings has a circumference of 3.016 km. The storage ring for the positron beam is called Low Energy Ring (LER), while the electron storage ring has a larger energy, so it is called High Energy Ring (HER). The two rings are crossing in the Tsukuba experimental hall, where Belle detector is located and the electron and positron beams collide there.

The KEKB was successfully operated for 10 years with the world-highest luminosity, 2.1×10^{34} cm^{-2}s^{-1} at the highest record and delivered an integrated luminosity of about 1 ab^{-1}. The SuperKEKB is an upgraded accelerator with the nano-beam idea [24]. There, the beam size is squeezed to a smaller size at the collision point as shown in Figure 2.1, and the beam currents are almost doubled for each. The designed luminosity of the SuperKEKB is 8×10^{35} cm^{-2}s^{-1}, 40 times higher than the peak of KEKB. The beam parameters of the SuperKEKB are summarized in Table 2.1 with those of its predecessor. A smaller beam size would lead to an increase of the emittance and a short beam life time via intra-beam scatterings. Therefore, the positron energy is changed from 3.5 to 4.0 GeV.

The corresponding change for the electron beam is needed to keep the SuperKEKB operating at the $\Upsilon(4S)$ resonance: it is reduced from 8 to 7 GeV. The lower energy of the electron beam also has an advantage in reducing the beam emittance. The schematic view of the SuperKEKB is depicted in Figure 2.2. The accelerator complex reuses most of the facilities of the KEKB [25].

Table 2.1: Beam parameters at the interaction point of KEKB and SuperKEKB for the LER/HER rings.

Parameters	KEKB Achieved	SuperKEKB
Energy (GeV)	3.5/8.0	4.0/7.0
Current (A)	1.64/1.19	3.6/2.6
Vertical beta function β_y^* (mm)	5.9/5.9	0.27/0.41
Vertical beam-beam parameter ξ_y^*	0.129/0.090	0.090/0.088
Luminosity ($10^{34}\mathrm{cm}^{-2}\mathrm{s}^1$)	2.11	80

In order to accommodate the designed parameters of the accelerator, many components need to be upgraded or newly build: the electron gun and the positron source are replaced by new ones to increase the current and improve stability. A new damping ring for the positrons has been constructed to be compatible with the LER dynamic aperture for reducing the beam emittance.

2.2 Belle II Detector

The Belle II detector is designed to measure vertex, energy and momentum of all the neutral (except neutrino) and charged particles, as well as to identify particle species with a high precision. The components of the Belle II detector must have an ability to take the data at a high event rate (30 kHz) under the high beam-associated background environment.

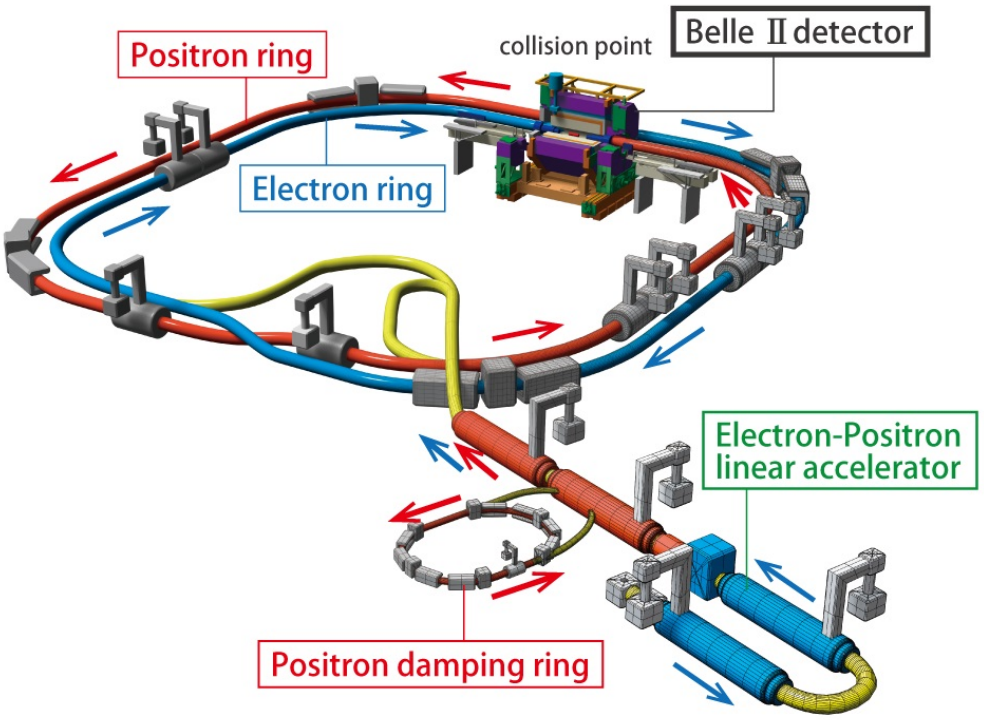

Figure 2.2: SuperKEKB accelerator complex.

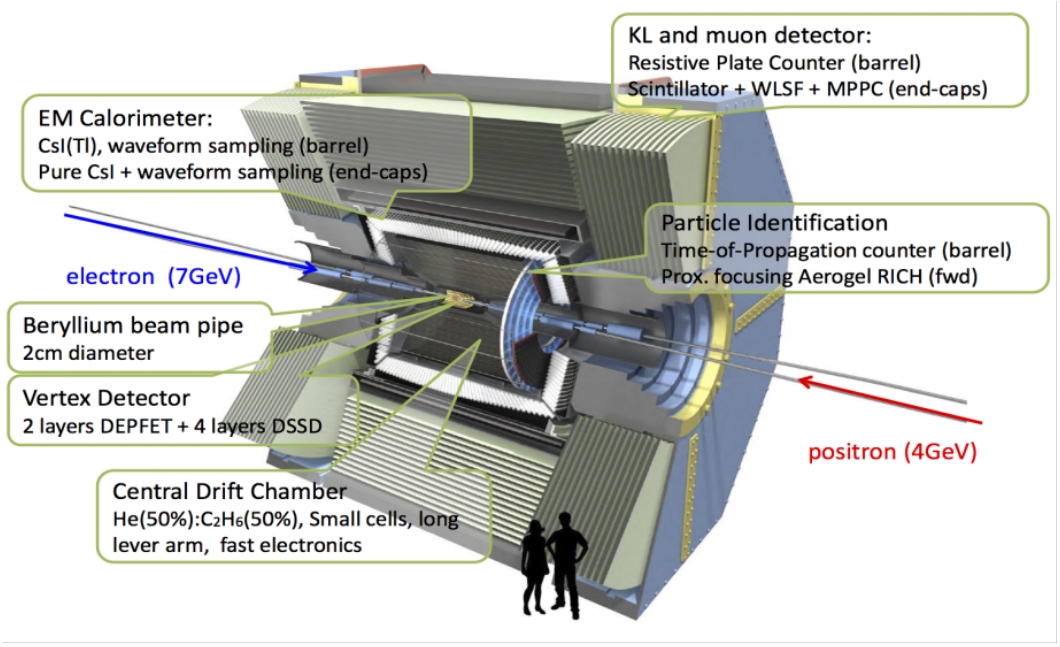

Figure 2.3: The 3D view of the Belle II detector

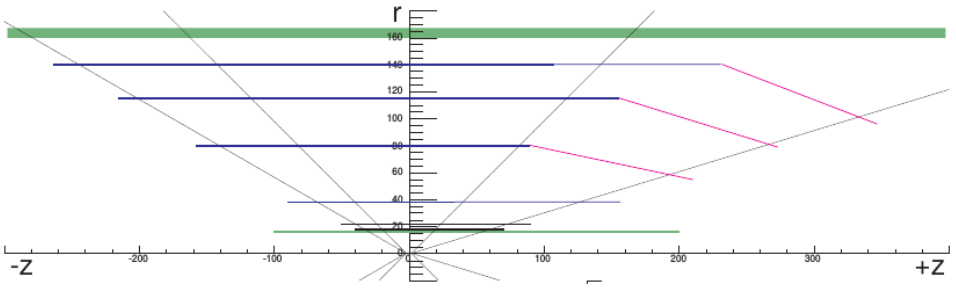

Figure 2.4: The configuration of the Belle II vertex detector.

2.2.1 VXD - Vertex Detector

A vertex detector is located at the innermost part of the Belle II detector. It plays a role to measure the vertices of charged particles, precisely. In comparison with the Belle detector, the radius of beam pipe at the IP is reduced from 1.5 cm to 1 cm, so that the innermost layer is much closer to the IP, and a decay vertex can be determined more precisely. The number of layers is increased from 4 to 6 layers. The inner layers will face the large beam backgrounds due to the increase of luminosity and the reduction of the inner radius. The Belle detector adopted Double-Sided Silicon Strip Detector (DSSD) for the vertex detector. However, under a high occupancy condition of the Belle II experiment, it is impossible to reconstruct the vertices with a strip detector. In order to reduce occupancy, a pixel detector is used for the innermost two layers, and the four outer layers are made of strip detectors.

- **PXD - Pixel Detector**

Because the final-state particles observed from decay processes in the Belle II experiment have relatively low energy, typically lower than 3 GeV, the multiple scattering effect is significant in them. Therefore, the thickness of the innermost detector must be very thin, so that amount of charge deposit in each pixel is very small, and difficult to readout. To cope with such conditions, Depleted Field Effect Transistor (DEPFET) technology is adopted for the Belle II pixel detector, PXD

[3].

The PXD has two layers, the inner (outer) layer consists of 8 (12) sensor ladders with as width of 1.5 cm (1.5 cm) and a length of 9 cm (12.3 cm) located at radius of 1.4 cm (2.2 cm). The two layers contain about 8 million pixels, in total. This large number of pixels affords a low occupancy under the high hit rate [3]. The readout electronics are mounted at the backward side of the detector.

• **Silicon Vertex Detector - SVD**

SVD consists of four-layer DSSD detectors. It is located between the CDC and PXD, and the radial position of the innermost (outermost) layer is 3.8 cm (14 cm). Following the designed acceptance of the Belle II detector, it covers the polar angles from 17 to 150 degrees. The forward side of the three outer layers are slanted in order to reduce the length of sensors.

2.2.2 CDC - Central Drift Chamber

The CDC is the central tracking device of the Belle II detector and is dedicated to reconstructing charged particle trajectories. It is immersed in a 1.5 T magnetic field provided by a super-conducting solenoid magnet. The Belle II CDC is larger than that in Belle [26] to fill the space left by replacing the Aerogel Cherenkov Counter by the Time Of Propagation counter (TOP), as to be is explained later. This geometry change provides an improvement for resolutions of the momentum and dE/dx. Smaller cell sizes are adopted for the innermost 8 layers to reduce occupancy of backgrounds [27]. The readout electronics are newly developed with full functionality on a single board and have ability to process data at a high event rate without dead time using the FPGA [28]. The CDC was successfully constructed and incorporated into the Belle II detector in 2016. The detailed design of the CDC is introduced in Chapter 3.

2.2.3 ARICH - End-Cap Particle Identification Detector

Particle identification (PID) detector plays a role to identify particle species. The Belle detector [29] employed an Aerogel Cherenkov Counter (ACC) system for PID. It consists of radiators and photomultiplier tubes (PMT). The radiator is made of silica aerogel with a small refractive index. When a charged particle passes through the radiator with a speed high enough, faster than the light in the radiator, it emits Cherenkov light. Cherenkov light is then detected by PMTs. Since Cherenkov angle is proportional to the charged particle velocity, particle type can be identified by combining the Cherenkov angle and the momentum information measured from tracking detectors. As Belle ACC worked as a counter, it was unable to measure Cherenkov angle, it only provided information whether Cherenkov radiation was emitted or not and a limit of the velocity only was obtained.

The PID detector at the forward end-cap of Belle II is Aerogel Ring Imaging Cherenkov (ARICH) counter. It is also composed by radiators and photon detector system. However, Hybrid Avalanche Photo Detector (HAPD) [3] is employed instead of PMTs as for Belle case. ARICH gets to be sensitive to the angle of Cherenkov light emission, thus the image of a Cherenkov ring is reconstructed, and the particle velocity can be measured for identification of particle types. The radiator is composed by two types of aerogel material with different refractive indices to increase the resolution of Cherenkov image. In total, 420 HAPDs are used for the Belle II ARICH.

2.2.4 TOP - Barrel Particle Identification Detector

The Belle Detector employed ACC and Time Of Flight (TOF) Counter as PID detectors in the barrel region. The ACC detector worked as the same as forward one. The TOF system consists of plastic scintillation counters which have a good

timing resolution and is used to measure the flight time of charged particles from the IP. This design provided a good PID for the Belle detector. However, a large amount of material of ACC and TOF degraded responses of the electromagnetic calorimeters, as to be mentioned in Section 2.2.5.

Time Of Propagation (TOP) technique is used for barrel particle identification of Belle II. It is a Cherenkov detector which consists of quartz radiators and photon detector system attached at the backward side. A radiator consists of a long quartz bar to generate Cherenkov light by an incident charged particle, and the Cherenkov light propagates to the end of the bar by repeating total internal reflection. A prism is attached at the region between the radiator bar and the photon detectors to expand Cherenkov rings in front of the photon detectors. MCP-PMT sensors are utilized for photon detection (see chap. 8 of Ref. [3]). Because of the good timing resolution (<50 ps), it allows to reconstruct Cherenkov ring images by determining the arrival time of each Cherenkov photon. Amount of the material in front of the calorimeters is reduced and has become more uniform comparing with the Belle case. This replacement has also enabled us to extend the outer radius of the CDC as mentioned before.

2.2.5 ECL - Electromagnetic Calorimeter

The ECL plays an important role to detect photons with a high efficiency, as well as to provide its direction and energy. It is also used for to identify electrons from other charged particles based on the ratio of energy deposit to the momentum and the shower shape. The ECL is also useful for trigger and luminosity measurement. Another function of ECL is to detect K_L^0 (K-long) mesons together with the KLM detector.

The ECL consists of the barrel and end-cap parts. It covers an acceptance in the polar angle range, $12.4 < \theta < 155.1$ degrees, which is a little larger than the

CDC acceptance. The ECL contains 8736 CsI(Tl-doped) crystals with a weight of about 43 tons, in total. Each crystal has a tapered shape with the average size about 6×6 cm^2 and 30 cm in length ($16.1X_0$). Two pieces of photodiode are attached at the rear side of the crystal to readout scintillation light. The intrinsic energy resolution of ECL as a function of energy is described by the following formula (see chap. 9 in Ref. [3]):

$$\frac{\sigma_E}{E} = \sqrt{\left(\frac{0.066\%}{E}\right)^2 + \left(\frac{0.81\%}{\sqrt[4]{E}}\right)^2 + (1.34\%)^2}, \tag{2.1}$$

where E is photon energy and measured in GeV.

2.2.6 KLM - K_L^0 and Muon Detector

The KLM is the outermost part of the Belle II detector, located outside the superconducting solenoid coil. It plays an important role to measure K_L^0 together with ECL and to identify muons from the other particles. Detector consists of alternating sandwich of iron and detector plates. An iron plate has a thickness of 4.7 cm, equivalent to 3.9 interaction length, in addition to a 30 cm length of CsI(Tl) crystal which corresponds to 0.8 interaction length. The iron plates also serve as magnetic flux return for the solenoid coil. The barrel part has octagonal shape, containing 15 detector layers and 14 iron-plate layers. Each of the two end-caps has 14 detector layers and 14 iron plates. The KLM system covers an acceptance close to the common design of Belle II, from 20 degree to 155 degrees in the polar angle.

K_L^0 mesons undergo hadron interactions in the heavy material (iron plates). Daughter particles of the shower are then recorded by the detector plates as an energy measurement. Since the muon mass is almost the same as the pion mass, it is very difficult to identify a muon from pion using energy loss of the charged

particles in the tracking detectors or PID detectors. Fortunately, a muon interacts with material only via ionization, while hadrons such as pion also interact hadronically. Hence, most of hadrons stop in the iron plates, while muons pass through the iron plates of KLM if it has enough high momentum to reach.

Two types of detector plates are employed for KLM. The glass-electrode based Resistive Plate Chambers (RPC) which have shown a good performance in the Belle experiment [29] are re-used for most of the barrel part. The two innermost layers of barrel and end-cap parts are replaced by the scintillation-based detector (see chap. 10 in Ref. [3]) to cope with the high beam-background rate.

2.3 Track Reconstruction

2.3.1 Track Finding

The purpose of track finding is to classify all the hits in each event into groups. Hits in each group are created by the same charged particle which passes through the tracking detector. Each group of hits is called "track". The track finder for the Belle II CDC is a combination of two algorithms: The Legendre track finder which is called the global track finder, and the cell automaton track finder is the local track finder.

The Legendre track finder uses the Legendre transformation to transfer hit information from the normal space to Legendre space, and then the Quad-tree method is used to search for intersections of the representative lines of hits in the Legendre space. The Legendre finder is fast and has a high efficiency for high P_T tracks which come from the IP. It is able to work with the missing hits. Detailed description of the Legendre finder can be found in Ref. [30].

The local track finder with the cell automaton algorithm is used to search for segments and tracks. It searches for hits using information in the neighborhood. With the super-layer structure of the CDC, firstly the segment in each super-layer is formed, and then they are combined to be tracks. It is more robust than the Legendre finder for cases: low momentum tracks where the energy loss and multiple scattering effects are large, and tracks do not come from the IP. More information about the implementation of the local track finder for the Belle II CDC can be found in the Ref. [31].

A CDC track is then extrapolated to the VXD detector in order to associate SVD hits with the track. The standalone track finding for SVD [32] is also developed. The SVD and CDC tracks are merged later in this approach.

2.3.2 Track Fitting

The role of track fitting is to fit a model of trajectories to the measurement points of the track hits in order to obtain track information such as the momentum and vertex of charged particles. Belle II tracks are fitted with genfit2 [33], an external library of basf2. Since the track finder selects hits with loose selection criteria, under the high background environment many background hits are assigned to tracks. That affects the track quality. To deal with such a high background conditions and the left-right ambiguity of CDC hits, Determined Annealing Filter (DAF) algorithm [34] is utilized for track fitting, where hits are weighted based on its residual and an annealing procedure is applied to obtain the best fit result.

2.3.3 Helix Parameters

After the track fitting for each track, the fit result of the closest hits to the IP is used to extrapolate toward the IP to find the Point Of Closest Approach (POCA).

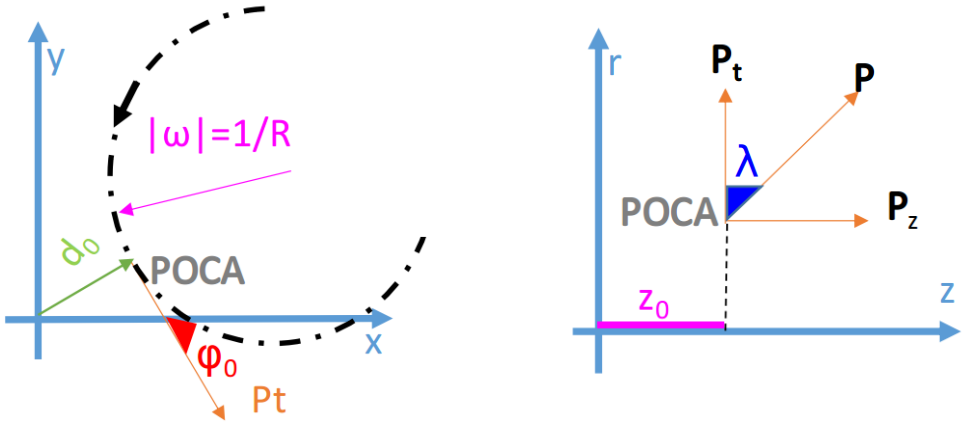

(a) (b)

Figure 2.5: Belle II helix parameters in views on x-y plane (a) and r-z plane (b).

Track parameters, called "helix parameter", are then obtained and stored. Belle II helix contains of five parameters (d_0, z_0, φ, ω, $\tan\lambda$), as shown in Figure 2.5, where

- d_0: the signed distance of the POCA from the IP in x-y plane. The sign depends on the direction of the angular momentum of the track at the POCA with respect to the magnetic field.
- z_0: the longitudinal signed distance of POCA from the IP.
- φ_0: the azimuthal angle of the transverse momentum at POCA with respect to the x axis.
- ω: the curvature, signed by electric charge of track.
- $\tan\lambda = P_z/P_T$, tangent of the angle between the momentum direction at POCA and the x-y plane (dip angle).

2.4 Charged Particle Identification

2.4.1 Muon Reconstruction and Identification

Each fitted track is extrapolated outward using Geant4e [35] for the outer detectors reconstruction, where pion mass hypothesis is assumed and it does not decay in flight. The Belle II geometry is used to take energy loss into account for determining the range of the track. The hit positions on each detector are stored for the reconstruction. For instance, the hit position at ECL is used for matching the track with clusters.

If the extrapolation points match KLM hits, these hits are assigned to the track. The expected range is compared with the real one which is determined by the number of KLM hits. If the difference between them is large enough, that track is regarded as a hadron. Otherwise, the extrapolation is performed again with Kalman filter algorithm and muon hypothesis. The χ^2 distribution of the hits from the extrapolation is also used for distinguishing a muon from hadrons.

2.4.2 Charged Particle Likelihood

Charged particle ID in Belle II relies on likelihood-based selectors. Information from each detector system is analyzed separately to estimate log likelihood for six long-lived charged particle hypotheses (electron, muon, pion, kaon, proton and deuteron). The difference in log likelihood between two particle hypotheses is used to calculate a PID value $\mathcal{L}(\alpha : \beta)$ as

$$\mathcal{L}(\alpha : \beta) = \frac{1}{1 + e^{\ln\mathcal{L}_\alpha - \ln\mathcal{L}_\alpha}} = \frac{\prod_{\text{det}} \mathcal{L}(\alpha)}{\prod_{\text{det}} \mathcal{L}(\alpha) + \prod_{\text{det}} \mathcal{L}(\beta)},$$

where α and β are two different particle hypotheses, and the product is over all the active detectors which provide PID information. By default, β is pion, and for that case the log likelihood ratio $\mathcal{L}(\alpha : \beta)$ can be written as $\mathcal{L}(\alpha)$.

The PID likelihood ratio, or PID value (for short), is calculated as a combination of all the sub-detectors. When a low-energy charged particle does not reach the outer detectors, the PID likelihood is calculated from the energy loss information of CDC and VXD detectors. When energy of the particle is high enough, an electron is basically identified by the ratio of the energy deposit in ECL and its momentum E/p, as well as dE/dx information from the inner detectors. Kaon and pion are identified by TOP and ARICH detectors. Muons are separated from the other hadrons by information from the KLM detector system.

Chapter 3

Belle II Central Drift Chamber

3.1 CDC Design

The Belle II CDC has a cylindrical shape with an inner radius of 16 cm and an outer radius of 113 cm. The length is 232.5 cm at the outermost radius. The CDC is asymmetric in z direction to deal with asymmetric-energy collisions. The structure of the CDC is shown in Figure 3.1. The two end-plates are made of aluminum. A thin carbon-fiber reinforced plastic (CFRP) is employed for the inner and outer cylinders to reduce the multiple scattering of particles. The thickness of the outer cylinder is 5 mm, and it plays an important role in supporting the wire tension of about 4 tons. The inner cylinder has a thickness of 0.5 mm in order to minimize the multiple scattering, and it supports the tension of the wires in the small cell chamber.

The CDC has two types of wire layer, axial layers and stereo layers. The axial wires ("A") are parallel with the z-axis as depicted in Figure 3.2a. The stereo wires are skewed to the z-axis with a small angle. The type with the positive stereo angles is labeled as "U" and that with the negative angles as "V". The typical stereo angle of the Belle II CDC is 70 mrad. The U type is sketched in Figure 3.2b.

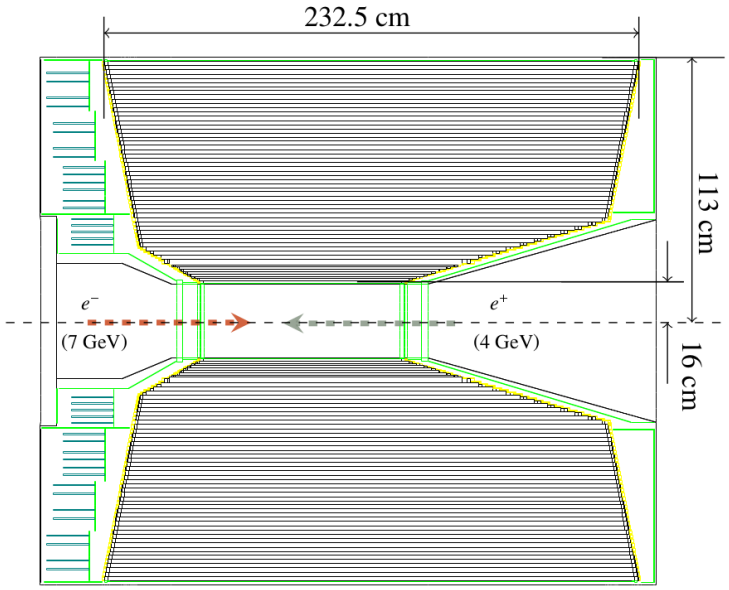

Figure 3.1: Longitudinal section the CDC detector.

The z position of a track is determined by the stereo layer hits. Because of the small stereo angle, the spatial resolution in z direction is worse than the resolution in r-ϕ plane. For instance, if the resolution of impact parameter in r-ϕ plane is 120 μm, the resolution in z direction is in the order of millimeter, $\sim$120(μm)/0.07 = 1.7 mm by the CDC alone.

The CDC contains 14336 cells in total. They are arranged in 9 super-layers for a total of 56 layers. Each super-layer has 6 layers with the same wire type except the innermost super-layer which contains two addition layers. These two layers might have very high occupancy due to the wall effect and might not work, because the applied high-voltage should be reduced in such case, the remaining 6 layers still work correctly. The 9 super-layers are arranged alternatively as A-U-A-V-A-U-A-V-A as shown in Figure 3.3, where the two types of stereo super-layer (U,V) are also arranged, alternatively. Parameters for the super-layers are summarized in Table 3.1.

Each cell consists of a sense wire surrounded by 8 field wires as shown in Figure 3.4. The cell shape is almost square. The smallest cell size is 6.59 mm of the

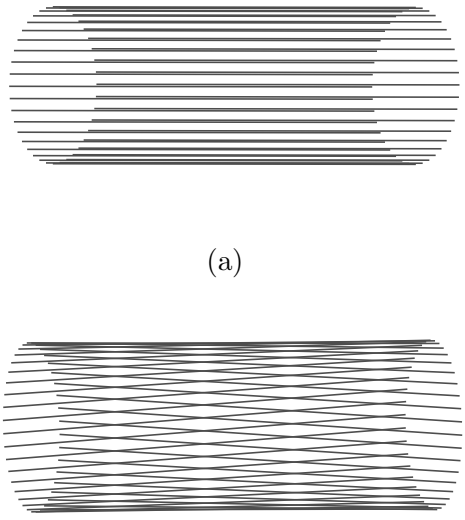

(a)

(b)

Figure 3.2: Depiction of the CDC wire types, (a) axial layer, (b) stereo layer with a nominal stereo angle of 70 mrad.

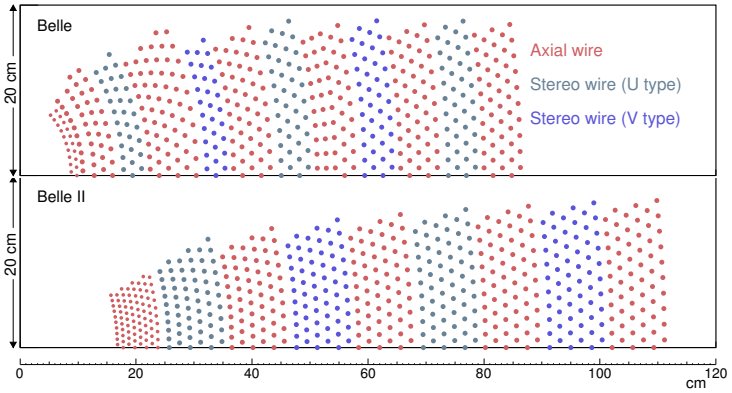

Figure 3.3: Layer configurations of the Belle and Belle II CDC.

layer 0 and the biggest is 18.18 mm the layer 55, the outermost layer. The sense wires are made of gold-plated tungsten, and the field wires are made of aluminum. Their diameters are 30 μm and 126 μm, respectively. The tension is 50 (80) g for a sense (field) wire. In comparison with the Belle CDC, the tension of field wires is reduced from 120 g to 80 g to reduce the deformation of the end-plates. The wire tensions are carefully measured and used for correction of the gravitational sag effect. A total of 42240 field wires are used for 14336 cells and the CDC has

56576 wires.

The CDC is filled with mixed gas, C_2H_6 (50%) – He (50%), as same as in the Belle CDC case. With the energy spectrum of charged particles in Belle II (typically lower than 3 GeV), this mixed gas has many good properties such as low radiation length, good spatial resolution, good energy loss resolution, low cross section for synchrotron radiation X-rays and small radiation degradation. Moreover, the drift velocity of an electron in this mixed gas is higher than other types of He-based mixture: the average drift velocity is about 33 μm/ns, the maximum drift time is around 350 ns for the largest cell (18 mm). The short drift time enables us to take data under the high event-rate condition of the Belle II experiment.

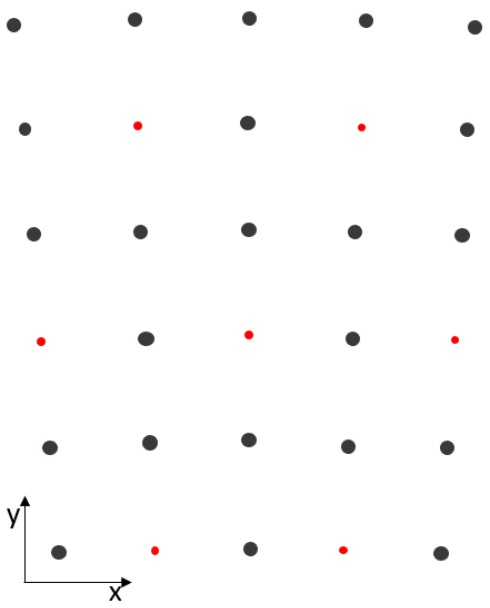

Figure 3.4: Wire configuration in cells of the Belle II CDC. The red circles are sense wires, and black circles are field wires.

The front-end (FE) readout electronics is designed to measure the pulse-height and the hit timing with the timing resolution of 1 ns and 5 μs delay for the trigger signal under a high event-rate (30 kHz) condition. The FEs are mounted at the backward side of the CDC, that is the blue-colored region at the left side in Figure 3.1. The power supply for the FEs and the high-voltage system are located

Table 3.1: The wire configuration parameters of the CDC

Super-Layer		No. of	No. of	Radius	Cell size	Stereo angle
ID	Type	layers	sense wires	(mm)	(mm)	(mrad)
0	A	8	160	168.0 - 238.0	6.59 – 9.34	0.
1	U	6	160	257.0 - 348.0	10.09 – 13.66	70.36 – 71.85
2	A	6	192	365.2 - 455.7	11.95 – 14.91	0.
3	V	6	224	476.9 - 566.9	13.37 – 15.89	-58.57 – -68.46
4	A	6	256	584.1 - 674.1	14.33 – 16.54	0.
5	U	6	288	695.3 - 785.3	15.16 – 17.12	67.38 – 74.88
6	A	6	320	802.5 - 892.5	15.75 – 17.52	0.
7	V	6	352	913.7 - 1003.7	16.30 – 17.91	-73.38 – -79.35
8	A	6	384	1020.9 - 1111.4	16.70 – 18.18	0.

in the Electronics Hut next to the Belle II detector. In total, 299 electronics boards are installed, and each board contains 48 channels. All functionalities such as pre-amplification, shaping, discrimination, ADC and TDC are implemented in a single board. Data are transferred to a central system of data acquisition (DAQ) through optical fibers [28].

A signal from chamber is fed into the FE, and then it is processed by ASD (Amplifier-Shaper-Discriminator) which is optimized for signal to noise ratio, dynamic range, timing resolution and power consumption. The analog output of ASIC is then digitized by a 10-bit 30 MHz ADC. In parallel, the timing signal is measured by a 1 ns timing resolution TDC implemented in FPGA. A typical threshold is set at 10pC (at the input of comparator) [36]. The digital data from ADC and TDC are stored in a ring buffer implemented in the FPGA to wait for the L1 trigger signal from the trigger system. When a trigger signal is asserted, the data in the ring buffer are transferred to a local readout buffer for suppression and formatting before being sent to the DAQ system.

3.2 Cosmic-ray Data Taking and Track Reconstruction

We have used data of comic-ray trajectories for calibration and tuning alignment of CDC.

• *Cosmic-ray data acquired without a magnetic field*: This set of data was triggered using a plastic scintillator, 100 cm (length) × 6 cm (width), located inside the inner cylinder of the CDC. Also, a track segment (TS) in the super-layer 2 of the CDC was required for the data taking, where a TS is an element which constructs a region for track trigger [3, 37]. The trigger timing was determined with the scintillator.

• *Cosmic-ray data acquired in the presence of a 1.5 T magnetic field*: This set of data was obtained in July and August 2017 using the Belle II DAQ system [38] and the following outer sub-detectors: Electromagnetic Calorimeter (ECL), time of propagation Cherenkov counter, and a barrel K_L and muon detector [3]. In order to record cosmic rays without using a plastic scintillator, a CDC TS at the super layer 2 and ECL signals are required. The trigger timing was provided by the ECL signals. This data was acquired concurrently with a magnetic field measurement at the IP region, and were affected by the presence of the measurement device (see Section 6), that had three aluminum plates with each 1.2 cm thick.

Performance of the CDC is also evaluated with Monte-Carlo simulation. Cosmic rays are generated by CRY generator software [39], and detector responses are simulated by Geant4 [35]. To realize the same acceptance and momentum distribution as the real data, the trigger conditions is applied to the detector simulation. All the steps are done in basf2 software (Belle II Analysis Software Framework) [40].

Cosmic tracks in both real and simulated cosmic data are reconstructed by the same procedure using the basf2. The Belle II track finder is suitable for cosmic-ray data analysis, in which all tracks are regarded as downward-going, instead of outward-going as in the case of the collision data. Tracks are then fitted by the genfit2 using the Deterministic Annealing Filter algorithm. Both biased and unbiased fitted parameters (drift distances and residuals) of each hit are stored for calibration and alignment purposes. A given hit is included (excluded) in the biased (unbiased) track fitting.

3.3 Calibration

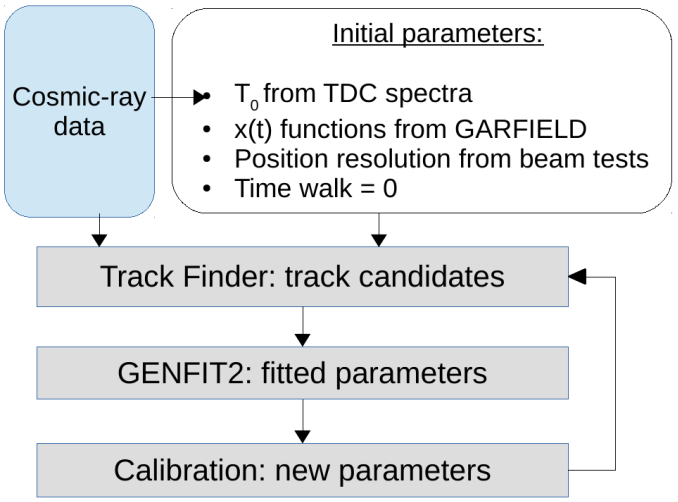

Figure 3.5: Flow chart of data analysis. Parameters used for the first iteration: the T_0 values for each channel, obtained from the TDC-count spectrum (see Section 3.3.2 for details) and the initial x(t) relations obtained from Garfield [4] simulation (see Section 3.3.3.

In this section, first, we describe the calibration procedure used for each parameter separately and follow it with an explanation of the entire calibration procedure. Each iteration (which is discussed later in this paper) includes a track

reconstruction, an acquisition of the fitted information of the associated hits, execution of the algorithms for the calibration, and then an update of constants for the next iteration (see Fig. 3.5).

3.3.1 Time Relation

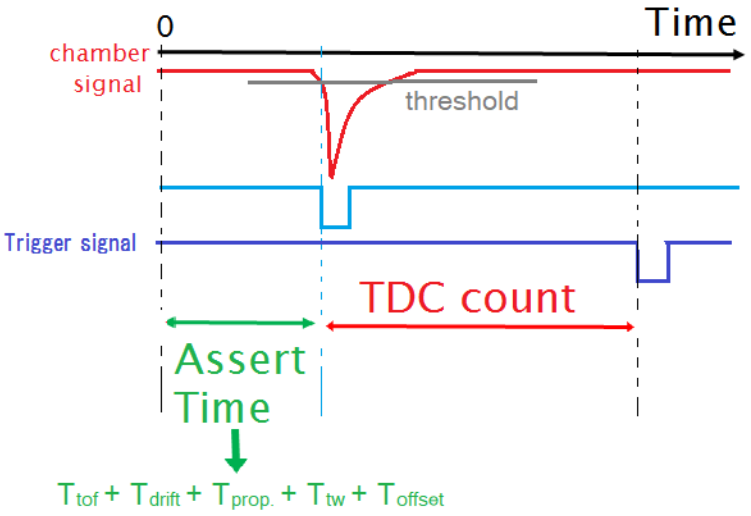

Figure 3.6: Time relation of CDC and trigger signals.

The TDC for the Belle II CDC is operated in the common stop mode as described in Figure 3.6. It is started by each hit signal of the CDC, T_{assert}, and stopped by the trigger signal T_{stop}. The Stop signal is released by GDL (Global Decision Logic), with a fixed latency, $T_{GDL} \simeq 5\mu s$. It is adjustable. The time relation is expressed as follows:

$$\mathrm{TDC} \cdot c = T_0 - T_{evt} - T_{tof} - T_{drift} - T_{prop.} - T_{tw}, \tag{3.1}$$

where,

- c (ns/bin) is the TDC resolution in its digitization, where c = $1/f$, and f is the frequency of a clock for driving TDC (f = 1.017774 GHz).

- T_0 is the sum of T_{GDL} and T_{offset}, where T_{offset} is the propagation time of signal on the cable between the backward end-plate and the FE electronics board and the processing time in the electronic boards, and it is different channel by channel. Hence T_0 is a constant and need to be calibrated for every channel.

- T_{evt} is the uncertainty of the stop signal which is different event by event called event timing or event T0.

- T_{tof} is the particle flight time from the trigger position (cosmic-ray) or the IP (beam data) to the ionization position.

- T_{drift} is the time for electrons drift to the sense wire.

- $T_{prop.}$ is the propagation time of signal along the sense wire to the backward end-plate.

- T_{tw} is the delay time due to the time walk effect. It will be corrected based on the dependence on the pulse height.

T_{tof} and $T_{prop.}$ are different for each hit (dependence of hit position) and are computed from the track information. An example of TDC count spectrum is shown in Figure 3.7, where a larger TDC count corresponds to shorter drift time.

There are two sources of T_{evt}. One is due to the trigger system, amounting to ± 4 ns, according to its operation frequency, that is a quarter of the accelerator RF frequency [38] resulting in $\sim$8 ns resolution. The other is the uncertainty of the reference timing signal. The magnitude of the latter components depends on the signal which is used for determining the L1 trigger timing (event timing). It is small for the cosmic data where the timing is provided by the scintillator, and it is large for data where the timing is determined by ECL signals because there is a large fluctuation in the timing measured by ECL signal.

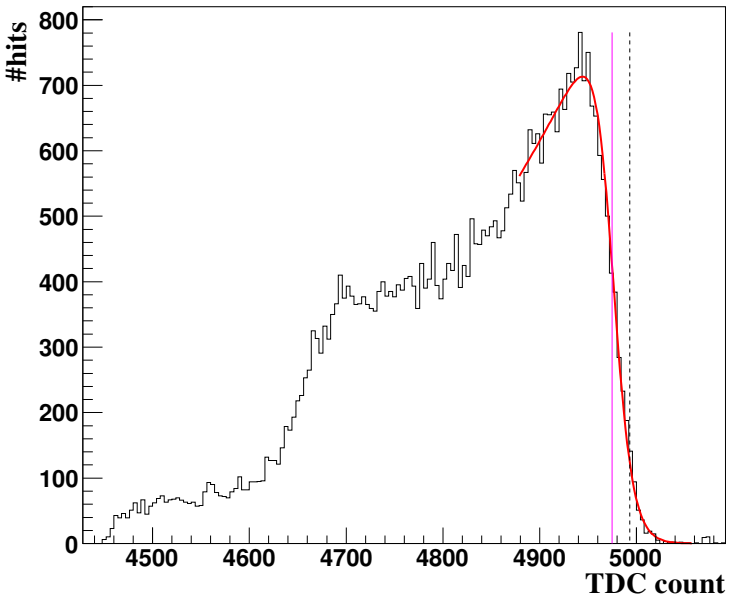

Figure 3.7: TDC count distribution. The rightmost slope is fitted to a Fermi-Dirac like function to obtain the reflection point of the edge, as indicated by the position of the magenta line. The position of the black dotted line is T_0, the detailed explanation is provided in Section 3.3.2.

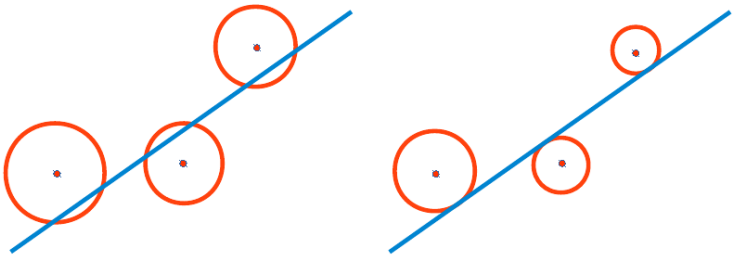

Figure 3.8: Schematic explanation of the relation between T_{evt} and drift time, depicted for the cases when event timing is wrong (left) and correct (right).

T_{evt} can be determined using the event timing extraction module in basf2. It searches for event timing based on minimum χ^2 method using CDC tracks. As mentioned above, T_{evt} affects all the hits in that event as illustrated in Figure 3.8: T_{evt} is negative and not applied to correct drift time in the left Figure, as all the calculated drift lengths used for the tracking become larger than the case a correct T_{evt} is applied (right). The algorithm determines T_{evt} where χ^2 of the track fitting is minimized. The 0.45 ns resolution of the event timing is obtained for the Monte-Carlo cosmic-ray events. The resolution for the real data is unknown. The

1.0 ns resolution is obtained for the cosmic-ray data taken with the scintillator, which includes the timing resolution of scintillator signals.

3.3.2 T_0 Correction

Determination and correction of T_0 for each channel are crucial to obtain a correct drift time of each hit. In order to start the first approximation tracking, a set of initial T_0 for all the channels is needed, and it is obtained from TDC spectra. In case that the particle passes through the region close to the sense wire, the drift time is zero and the TDC value is the maximum and is assigned by the value at the rightmost edge of the TDC spectrum. Since the mean of event timing T_{evt} is zero by definition. The initial T_0 value can be simply estimated as:

$$T_0^{initial} = \mathrm{TDC_{edge}} \cdot c + T_{tof} + T_{prop.} + T_{tw}, \tag{3.2}$$

where $\mathrm{TDC_{edge}}$ is the reflection point of the rightmost edge of the TDC spectrum, $\mathrm{TDC_{edge}}$ is shown as the magenta line in Figure 3.7 and is determined by fitting the TDC spectrum with a Fermi-Dirac like function:

$$f(t) = p_0 + p_1 \frac{e^{p_2 t}}{1 + e^{-(t-p_4)/p_5}}, \tag{3.3}$$

where p_0 represents the amount of background and noise hits; an exponential function with the two parameters p_1 and p_2 is used to describe the main region of spectrum; p_4 is $\mathrm{TDC_{edge}}$; and $\mathrm{p_5}$ is the slope parameter for the edge, which relates to the resolution of the time measurement and is also useful for data quality monitoring. All the parameters p_0 to $\mathrm{p_5}$ are floated in the fit. In cosmic-ray case, time of propagation delay on wire, $T_{prop.}$ and time of flight, T_{tof} are roughly calculated assuming the polar angle of 90 degrees,velocity $v/c = 1$ and $T_{tof} = r/c$, where r is the layer radius of the given channel and c is the light velocity. The

same value for the time walk effect is applied at this step, the time walk effect is calibrated as a function of ADC (mentioned at Section 3.3.6). The position of the black dotted line in Figure 3.7 is T_0, and the difference between $\mathrm{TDC_{edge}}$ and T_0 is the sum of T_{tof}, $T_{prop.}$, T_{tw}, and T_{evt}.

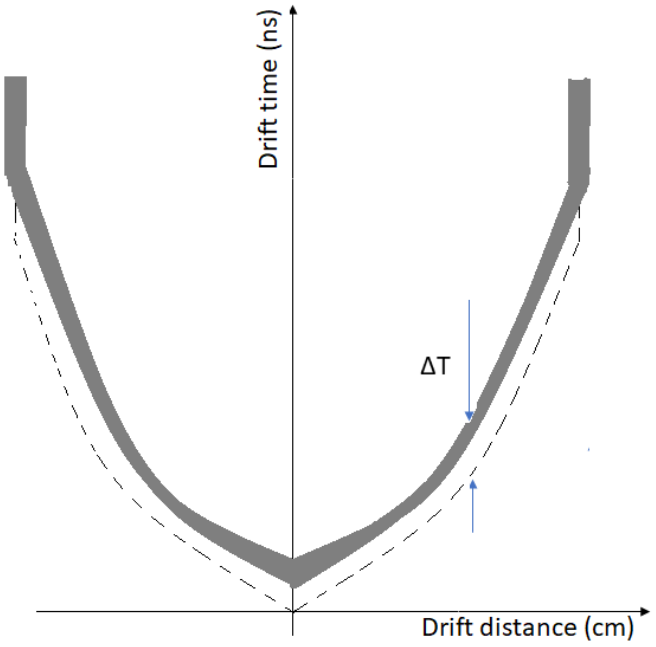

Figure 3.9: Behavior of x(t) relation when T_0 is shifted by a ΔT. The dashed line is the x(t) relation which was used to estimate the drift distance for tracking. The gray region is the data after the tracking, where drift times are calculated from unbiased fitted drift distances.

Figure 3.9 sketches the x(t) relations for a case where T_0 is shifted by ΔT. If $\mathrm{T_0}$ is wrong, the data shift along the drift time axis. This shift is defined as time residual $\Delta T = T_{mea} - T_{fit}$. ΔT for each channel is the mean of the time residual distribution. It is found by fitting the distribution with a Gaussian function. To obtain a good resolution of ΔT, hits in the regions near a sense wire and cell boundary are rejected because the resolution is worse there. T_0 of each channel is corrected by an amount of ΔT in each iteration. This procedure is iterated until ΔT of all the channels are close to zero within 0.5 ns: 4 iterations are needed typically. Figure 3.10 shows ΔT for all channels of a typical layer (layer 6). Each point represents ΔT for each channel. At the first iteration (red triangles) ΔT

fluctuates channel by channel and most of ΔT become close to zero after the 4^{th} iteration (full black circles). ΔT around the channels 0, 80, and 160 still fluctuate and has large errors after the T_0 correction because these channels correspond to the horizontal region where the statistics is low in the cosmic ray data.

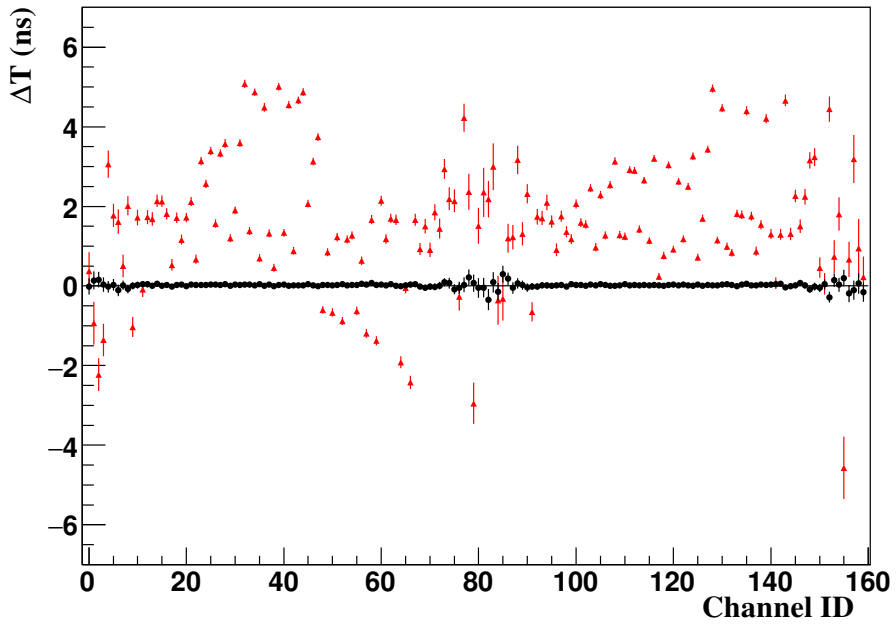

Figure 3.10: ΔT for each channel in layer 6 before (red triangles) and after (black circles) the calibration.

3.3.3 Time to Space Relation, x(t) function

The incident angle of a track in $r-z$ plane (θ) is defined as the angle between the momentum vector and the z axis, and the incident angle in $r-\phi$ plane (α) as the angle between the unit vector of the wire position from IP ($\overrightarrow{w}$) and the momentum vector at the point of the closest approach to wire ($\overrightarrow{\mathrm{p}}$), as shown in Figure 3.11. The angle α and θ are derived as follows:

$$\alpha = \arctan \frac{(\overrightarrow{w} \times \overrightarrow{\mathrm{p}})_{\mathrm{z}}}{\overrightarrow{w} \cdot \overrightarrow{\mathrm{p}}},$$

$$\theta = \arctan \left(\frac{\mathrm{P_T}}{\mathrm{P_z}} \right).$$

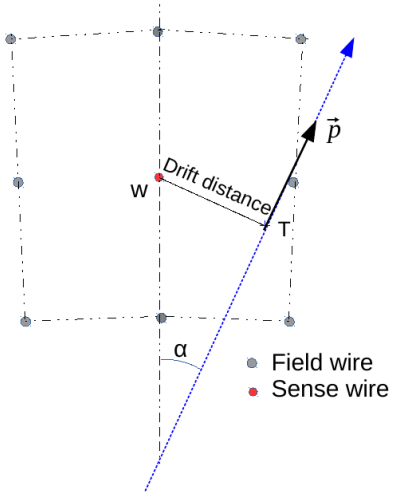

Figure 3.11: Definition of the incident angle α.

The left or the right passing of a track through a cell (L/R) is defined as follows:

$$\mathrm{L/R} = \mathrm{sign}((\overrightarrow{w} - \overrightarrow{\mathrm{T}}) \times \overrightarrow{\mathrm{p}})_{\mathrm{z}}, \tag{3.4}$$

where $\overrightarrow{\mathrm{T}}$ and $\overrightarrow{\mathrm{p}}$ indicate a position vector and a momentum vector at POCA of the track to the sense wire of the given cell. The positive sign corresponds to the right side.

The cell sizes are different layer by layer: smaller at the inner layers and larger at the outer layers. The left-right symmetry of x(t) function is broken under the magnetic field. Figure 3.12 shows the x-y view of electron drift lines as well as isochron lines of the drift time in a normal cell under a 1.5 T magnetic field. It is clear that drift lines of electron have different shapes for different incident angle (α)e. The x(t) relation depends also on the polar angle in the r-z plane (θ), especially, in the transition layers between the two types (axial and stereo), since they are bounded by a different shape (type) of field wire layers. That leads to a change of the cell shape along z (or polar angle). Because of these reasons, x(t) relation should be calibrated for each layer, different incident angles, polar angles and the left-right passage, $\mathrm{x} = \mathrm{f}(\mathrm{Layer}, \mathrm{L/R}, \alpha, \theta, \mathrm{t})$.

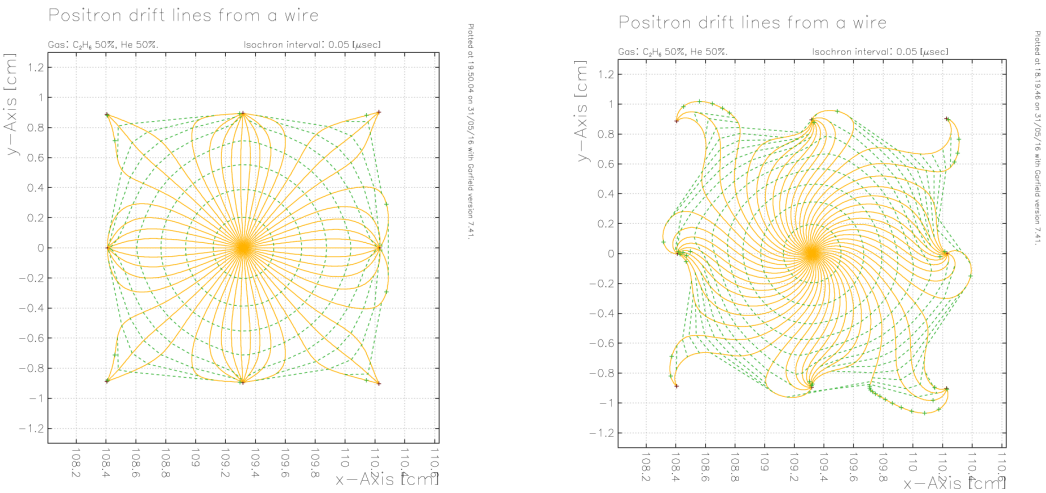

(a) B=0 (b) B = 1.5 T

Figure 3.12: Drift line (yellow line) and arrival time contour (green dash line) of electron in a normal cell computed by Garfield. The gas mixed is C_2H_6 50% − He 50%.

Assuming that the x(t) relation at the same POCA position is independent to the direction of the track, that is, the x(t) relation for the track with momentum $\overrightarrow{P}$ is same as the track $-\overrightarrow{P}$. the x(t) relation is calibrated only for the outgoing tracks. The estimated values for incoming track are converted to the corresponding values for the outgoing track and the calculation of the drift length is performed with the same way. α is defined in the range from -90 to 90 degrees. The x(t) relation is prepared with a step of 10 degrees of α because of the strong dependence of x(t) on α. This treatment is the same as that used at the Belle CDC [26]. The acceptance of CDC is $17 < \theta < 150$ degrees but the x(t) relation is calibrated for the full range $0 < \theta < 180$ degrees. Since the variation of x(t) on θ is not large, it is split to 7 bins. The configuration for α and θ is listed in Table 3.2. The first and last θ bins are not represented by the bin centers because most of the data come from the $\theta > 18$ degrees for the first bin and $\theta < 150$ degrees for the last bin. Adopting this configuration, A total of 14112 x(t) functions need to be calibrated.

The drift distance for the track reconstruction is obtained by interpolation of the values from the four adjacent bins.

Table 3.2: Boundaries and representative value for α and θ bins. Unit is degree.

Bin No.	Lower	Upper	Representative
θ			
1	0	29	18
2	29	50	40
3	50	75	60
4	75	105	90
5	105	125	120
6	125	139.5	130
7	139.5	180	149
α			
1	-90	80	-85
2	-80	70	-75
...	...	...	...
18	80	90	85

The time to space relation is obtained from the relation of the unbiased drift distance and drift time which is calculated by Eq. 3.1. The drift distance vs. drift time plot is then projected to the drift distance axis to calculate mean drift distance for every bin. The bin width is 3 ns and each drift-time bin is represented by the central value of the bin. The relation between the drift distance and drift time is then fitted with x(t) function. A set of x(t) relation which is calculated using the Garfield program [4] is used for the first approximation in tracking. After each iteration, new set of x(t) functions is applied for the next iteration. This procedure is repeated until x(t) relation converges and that needs about 3 iterations. The convergence condition is given by size of the variation in means of the number of degrees of freedom (ndf) and p-value for the χ^2 distribution in the track fit between the two consecutive iterations, which are required to be less than 0.2 and 0.01, respectively.

Figure 3.13 shows the time to space relation of a small cell layer (layer 1) and a large cell layer (layer 54). The data are superimposed with the x(t) function

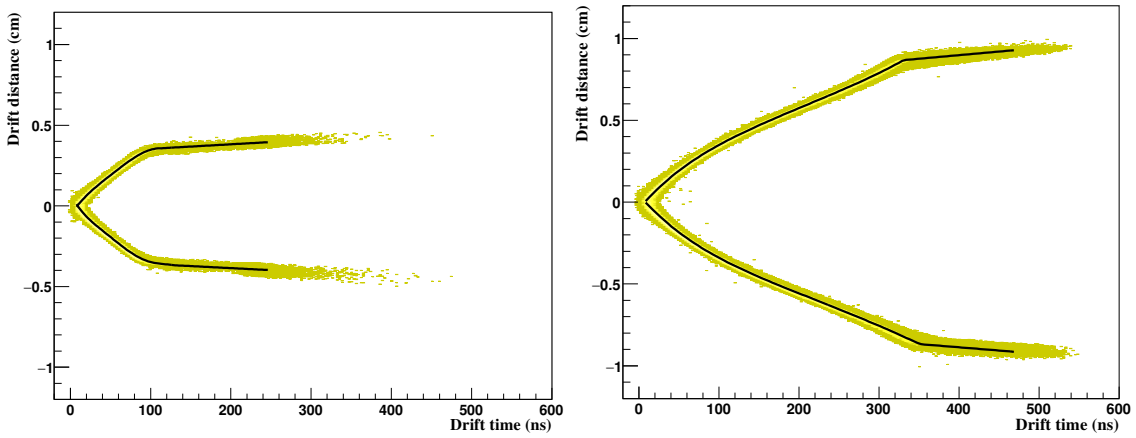

(a) Layer 1, $\alpha = 15$ degrees, $\theta = 90$ degrees.

(b) Layer 54, $\alpha = 15$ degrees, $\theta = 90$ degrees.

Figure 3.13: x(t) relation of a small cell size layer (a) and a large cell size layer (b). Data (yellow) are supperimposed with x(t) function (black lines).

(the black line). Positive (negative) drift distances correspond to the right side (left side). The 5^{th}-order Chebyshev polynomial function is utilized to describe x(t) relation of the main region, which is the range of the drift time from zero to 350 ns (330 ns) for the left (right) sides in Figure 3.13b, . A linear function describes the x(t) relation at the boundary regions with a longer drift distance. These two functions are made to be continuous at the transition point. The x(t) relation at boundary region is more sophisticated than a linear function in reality. But statistics are small at the large drift-time region and the position resolution is worse there (see Section 3.3.4). For simplicity, a linear function is adopted as a functional approximation.

A typical example of the incident angle (α) dependence of the x(t) function is shown in Figure 3.14. x(t) relations at the small drift distance are almost the same for all the angles. They become gradually different at the large drift distance and much different in the boundary region. This difference is equivalent to that of drift lines explained above. The dependence of x(t) relation on the incident angle (θ) is not shown here as they have only tiny different. The effect would is visible on the x(t) plot drawn with a cm scale.

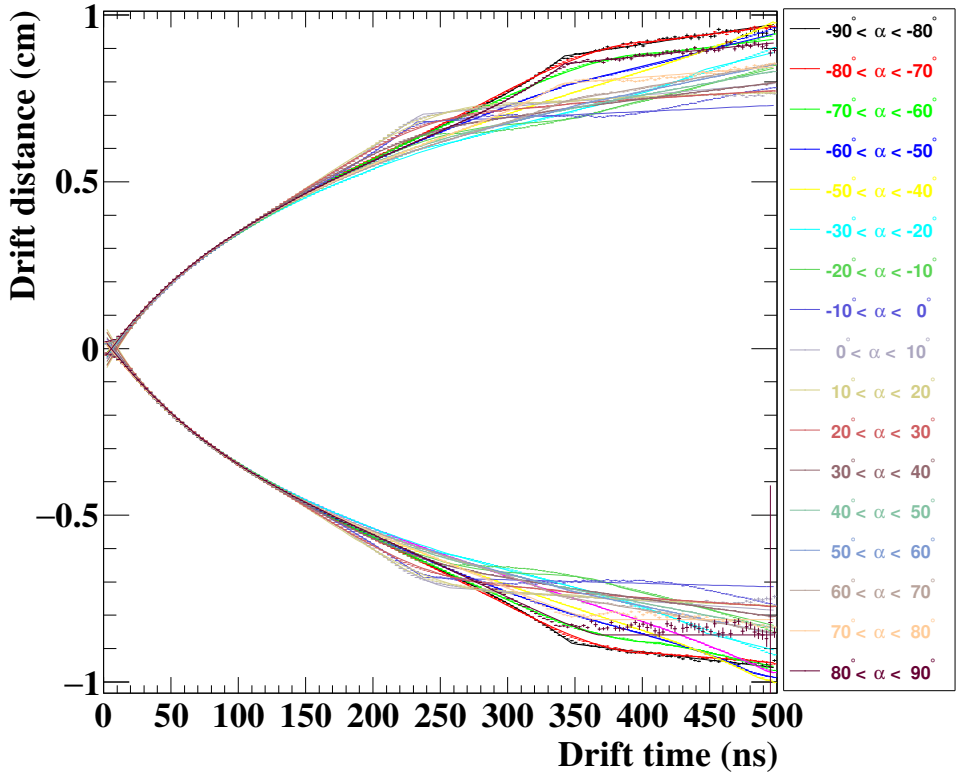

Figure 3.14: α dependence of the x(t) relation. The plot shows results of layer 18, and $\theta = 90$ degrees.

3.3.4 Position Resolution

Position resolution or intrinsic resolution, σ, is defined as a standard deviation of the measured drift distance (measurement error). The Belle II track fitting software (genfit2) can provide both biased and unbiased track fit results for each hit, so the position resolution can be calculated from its relations with the biased and unbiased resolutions in order to exclude the contribution of the track fitting errors. The biased and unbiased resolutions are standard deviations of the biased and unbiased track-fit residuals, respectively. In the biased track fit, the given hit is included in the track fitting, and in the unbiased is not. The relation between the positions, the biased and unbiased resolutions are discussed in Appendix A. Since the position resolution is estimated and iterated together with the x(t) calibration,

position resolution is estimated using following formula:

$$\sigma = \sqrt{\sigma_{\text{unbia}} \cdot \sigma_{\text{bia}}}, \tag{3.5}$$

where the σ_{unbia} and σ_{bia} are the position resolutions estimated for the unbiased and biased track fits. The biased and unbiased residual distributions are plotted for each slice of the unbiased drift distance, x. Each distribution is then fitted with a Gaussian function to obtain σ_{unbia} or σ_{bia}. The bins near a sense wire ($x < 0.1$ cm) are treated differently: they are fitted with a Gaussian function just using the positive side of the residual distribution. This is because hits with negative drift distances are rejected in the track reconstruction (negative tail is cut-off).

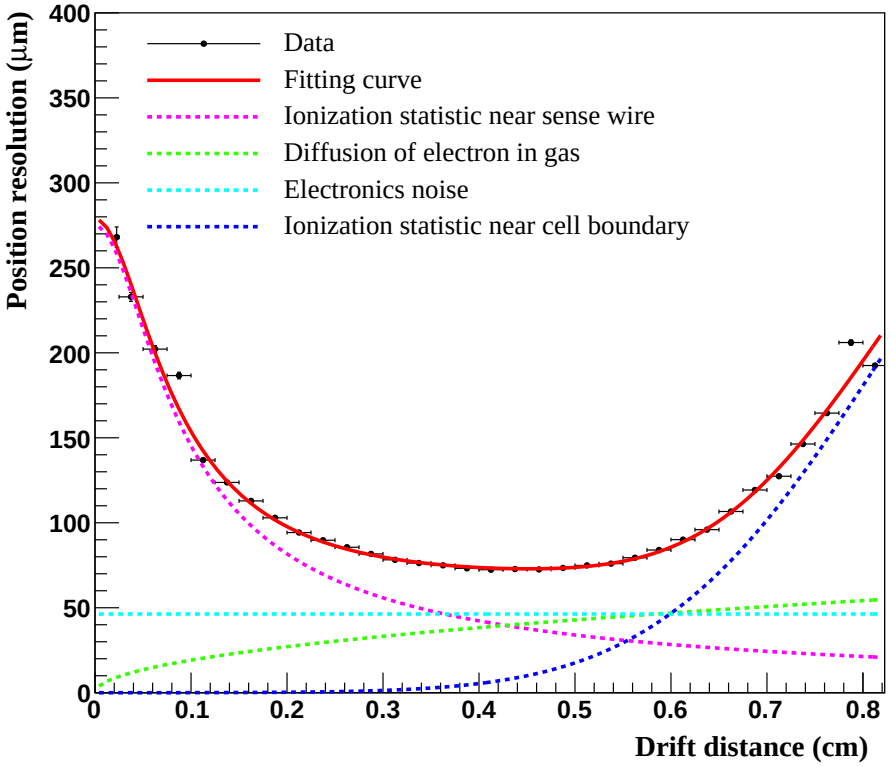

Figure 3.15: Position resolution as a function of the drift distance for the left side, layer 51, $\alpha = 5$ degrees and $\theta = 60$ degrees.

In the same way as for the x(t) relation, position resolution is also obtained for each layer in the different incident angles, polar angles, and the left-right sides,

$\sigma = \sigma(\text{Layer}, \text{L/R}, \alpha, \theta, \text{t})$. A typical example of the position resolution as a function of drift distance is shown in Figure 3.15. At the region close to the sense wire (short drift distance), the position resolution is worse because of the ionization statistics where effect is quickly decreases as a function of the drift distance. The effect of electron diffusion in the gas increases proportionally to the drift distance. At the boundary region where the drift paths are distorted, a small fluctuation caused by ionization statistic leads to a large difference in the measured drift time. This effect is called "the distortion of electric field". It depends strongly on the incident angle α as for the x(t) relations.

The best position resolution is obtained in the intermediate drift-distance region where both the ionization statistics and the distortion of electric field effects are small. The best value for the position resolution 75 μm is obtained in the region of 0.5 cm drift distance. Such the best value of the position resolution depends on layer, incident and polar angles. It varies from 50 μm to 120 μm, they are mostly lower than 100 μm. The average position resolution obtained from Figure 3.15 is 120 μm. In principle, the average resolution over the cell for the Belle II CDC is worse than that of the Belle, because of smaller cell size.

To store the position resolution as a function of drift distance into database, which is needed for analyzing the collision data and Monte-Carlo simulation, a function is developed with an assumption that there are four main contributions: (1) the ionization statistics effect; (2) the diffusion of electron in gas; (3) the electronics noise; and (4) the distortion of the electric field at the cell boundary region. The fit function is quadratic sum of these four components. They are shown by pink, green, cyan, and blue lines, respectively in Figure 3.15. The ionization statistics effect is dominant in the small drift distance region [41]. The diffusion of electron in gas is proportional to $\sqrt{\text{x}}$. The electronics noise is assumed to be independent to the drift distance. The distortion of electric field is empirically described by an exponential function.

The dependence of the position resolution on α is shown in Figure 3.16 for a typical layer. In the short drift distance region, the position resolution is almost same for all the angles. As seen in Figure 3.12, the drift lines in this region are homogeneous for all the directions. The resolution is largely different at the angles in the large drift distances region. The best resolution is achieved at α around 30-50 degrees. Because the shape of drift paths in these angles is much more uniform than that in the other angles, a fluctuation of ionization does not cause large fluctuation on the measured drift time. The best resolution about 50 μm is obtained at the 0.7 cm drift distance for the 35 degrees α angle.

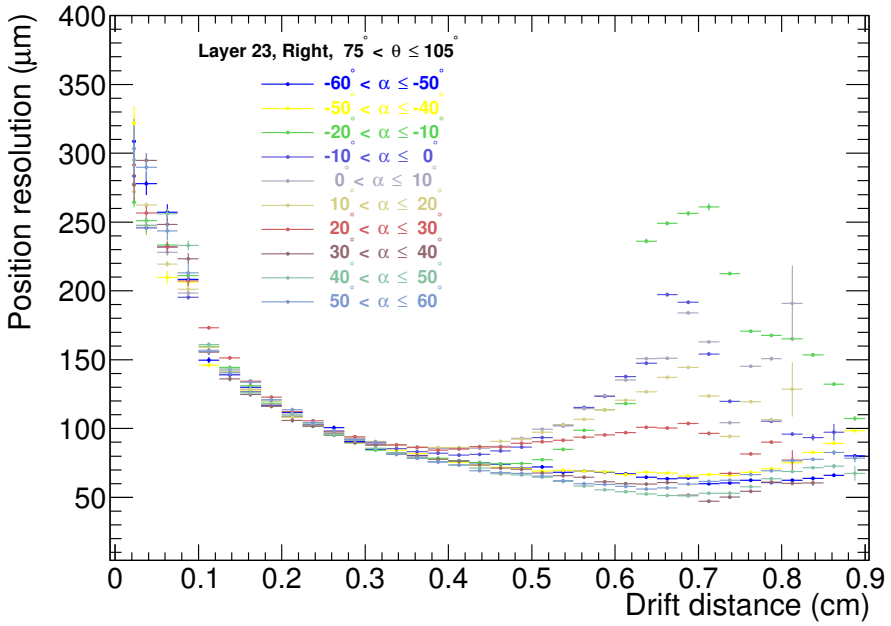

Figure 3.16: α dependence of the position resolution. Results of right side for layer 23 with $\theta = 90$ degrees.

The dependence of the position resolution on θ is shown in Figure 3.17 for a typical layer. As seen in x(t) relation, the shape of drift paths are almost same for all the polar angles, the shape of the position resolutions as a function of drift distance is basically similar among the different polar angles. However, the resolutions are the worst at the polar angle of 90 degrees as shown by blue points in the figure, and they are better at larger or smaller angles because the ionization statistics effect is smaller in these angles. The best resolution is obtained in the

angles $140 < \theta < 180$ degrees, as shown by the cyan points. The difference is large in the short drift distances region and smaller in the larger drift distance region. The difference of the position resolutions between 90 and 149 degrees is 40 μm at the drift distance of 0.4 cm.

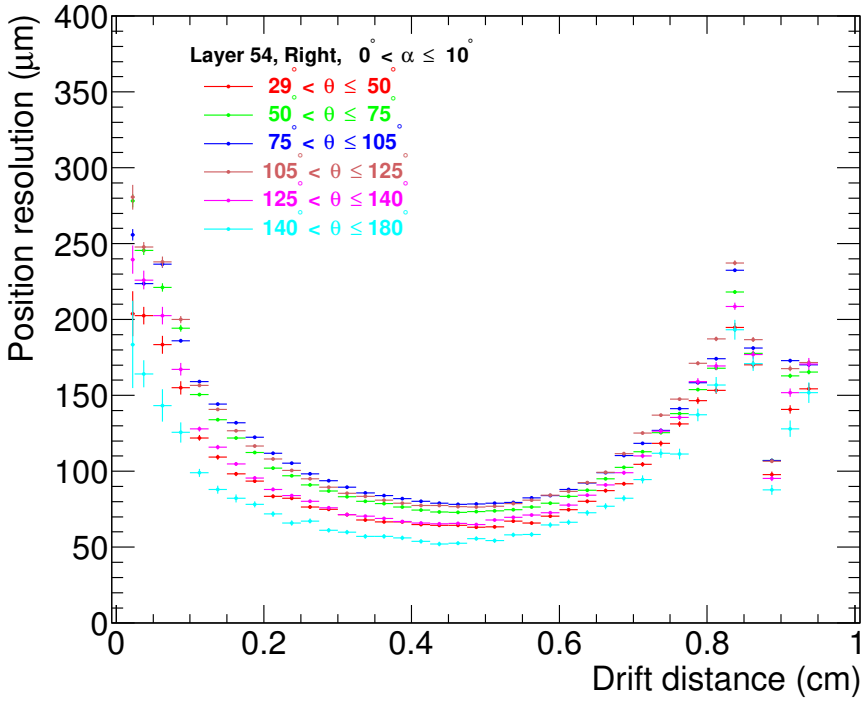

Figure 3.17: θ dependence of position resolution. Results of the right side of layer 54 with $\alpha = 5$ degrees.

3.3.5 Time Walk Effect

A signal from the CDC is split into two paths: one for pulse-height measurement with ADC, and the other for timing measurement with TDC, where a leading-edge type discriminator is employed. The timing measurement is, hence, dependent on the input pulse height (this effect is known as time walk). Calibration of this effect is performed after those of T_0, x(t) and position resolution. The time residual (ΔT) defined in Section 3.3.2 is estimated for every electronics boards. The dependence of ΔT on the ADC count is shown with red points in Figure 3.19 for board ID 20 as an example.

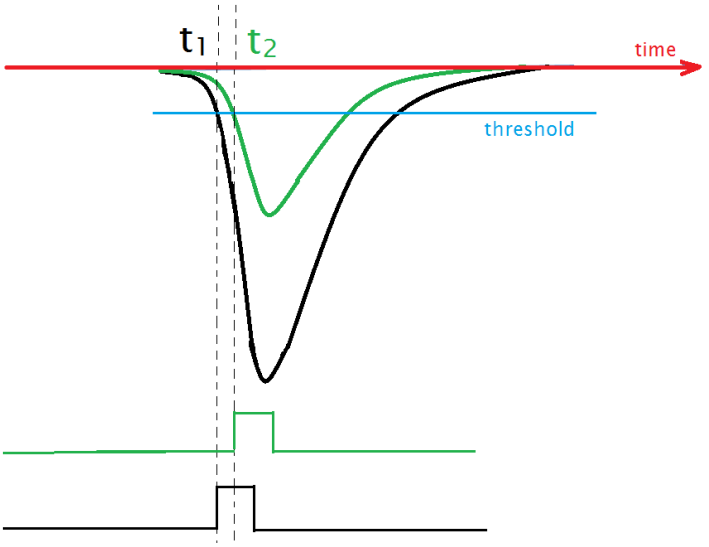

Figure 3.18: Time walk effect.

In the Belle CDC case, a function "$a + b/\sqrt{\mathrm{ADC}}$" was adopted for the time walk correction, however, the time walk effect correction with this function is not good enough for the Belle II CDC. so an exponential function (Eq. 3.6) is utilized for Belle II CDC, It fit well to the data, as shown in Figure 3.19.

$$\Delta T = p_0 + p_1 e^{-p_2 * \mathrm{ADC}}, \tag{3.6}$$

where, p_0, p_1 and p_2 are constants for each electronics board. The constant term p_0 is ADC-independent. It is absorbed into T_0. The fitted function is shown by the red line in Figure 3.19. The black points shows the results after applying the correction. They are zeros within 0.5 ns for the whole ADC range except the first point (ADC < 10), where the hits mostly come from noise. Since the time walk correction affects the drift time determination, a few iterations for the T_0 correction, x(t) and position resolution calibrations are needed after the time walk corrections.

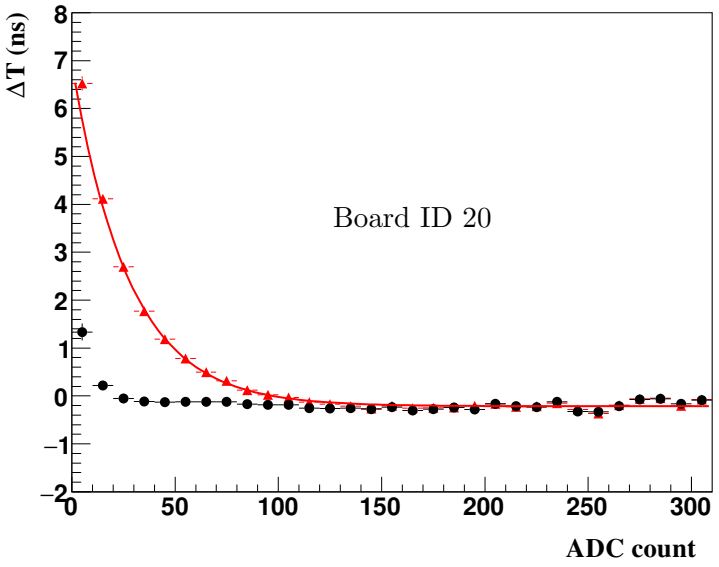

Figure 3.19: Time walk correction. The red triangles (black circles) are the ΔT before (after) the time walk correction. The red line shows fitted function.

3.3.6 Propagation Velocity

Material of the sense wires is gold-plated tungsten as same as that of the Belle CDC, so the same propagation speed of the signals along the sense wire is expected in Belle II CDC ($V_{\text{prop.}} = 27.25$ cm/ns). Its validity is confirmed by checking ΔT as a function of z hit position. Figure 3.20 is the result for a typical layer (layer 31), where ΔT is almost zero for all the region of z hit position.

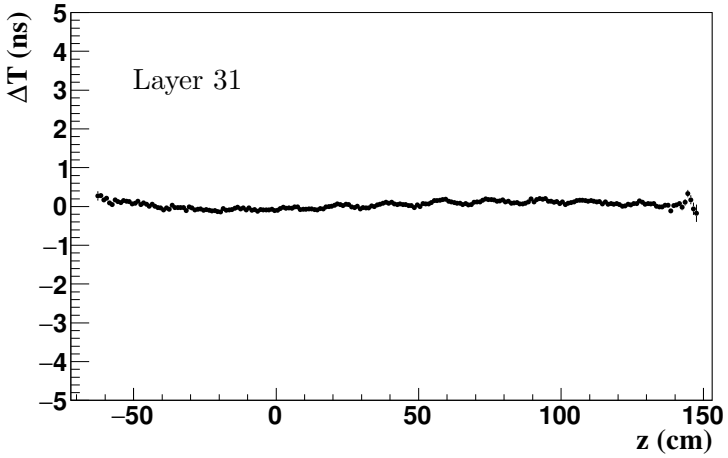

Figure 3.20: z hit position dependence of ΔT.

3.3.7 Calibration Procedure

The calibration procedure is summarized in a block diagram of Figure 3.21. The calibration starts with the correction of T_0 and is iterated until ΔT_0 for all the channels come close to zero. Then x(t) relation calibration is performed. Since x(t), T_0 and position resolution correlate with each other, T_0 is corrected again after each update of the x(t) constants. Because the correlation between position resolution and T_0 are small, they are updated simultaneously at this step. These steps are repeated until they are converged. Typically, 3 iterations are needed. Finally, the time walk calibration is performed, and the procedure is repeated until the correction is small enough, that means the ΔT is close to zero for the whole range of ADC. After the time walk effect is corrected, T_0 correction, x(t) relation and the position resolution calibrations are performed again. However, only few iterations are needed for the second calibration loop.

Steps in each iteration are listed in Figure 3.22. First, Track reconstruction (track finding and track fitting) is performed from the raw data (containing of CDC hit information). Fit information is then collected by a collector module and stored in output files. When all the reconstruction and collection jobs are finished, algorithms which deal with the T_0 correction, x(t) function, position resolution or time walk calibration are executed to create new constants. The database is then updated by the new constants for the next iteration.

3.3.8 Comparison with the Belle CDC Calibration

In case of the Belle CDC, T_0 was calibrated for each channel, However the calibration was done on the drift distance domain. The mean of residual distribution for each channel was estimated from the track fitting. Then the ΔT was calculated

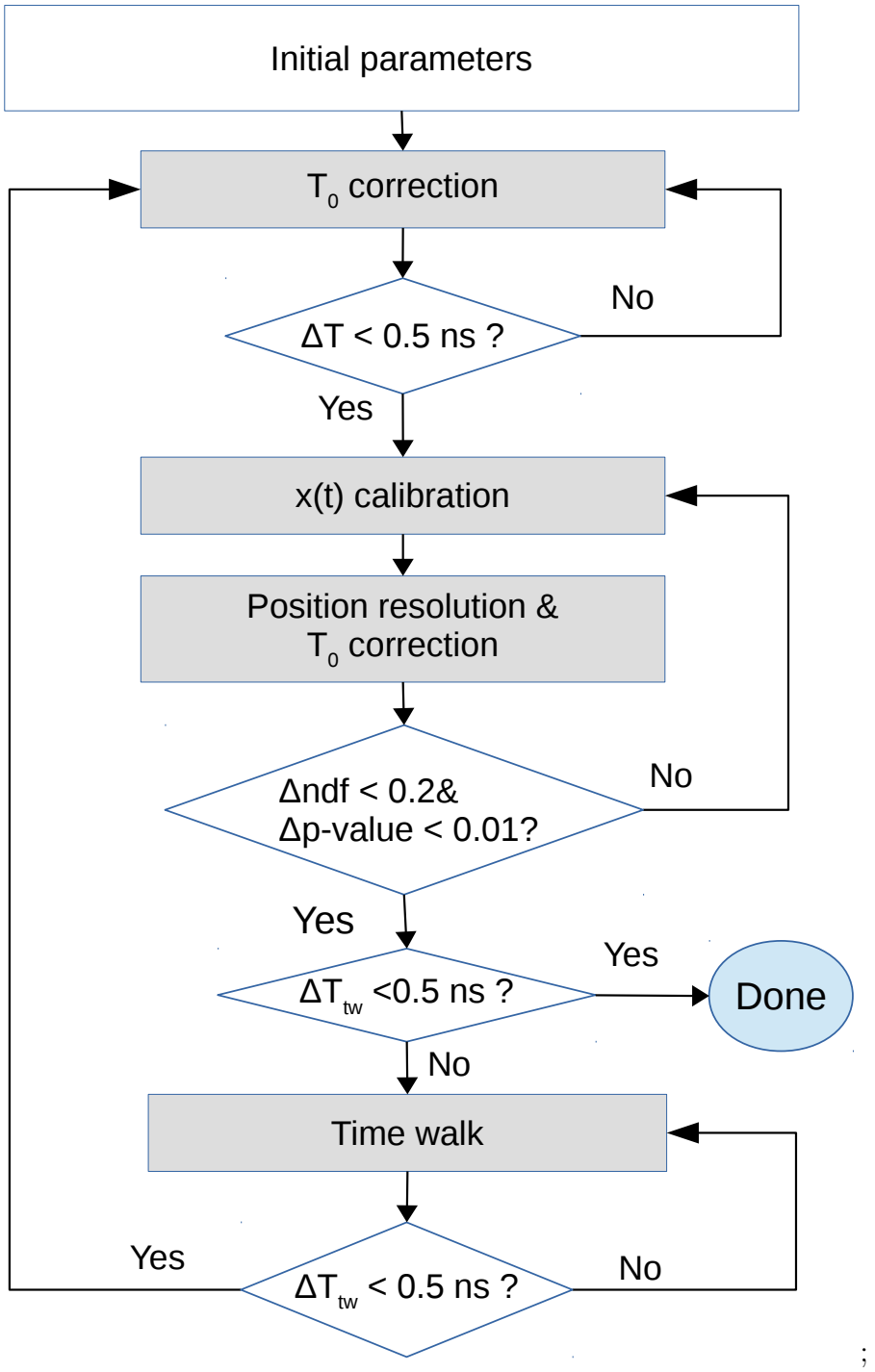

Figure 3.21: Calibration procedure for CDC. The Δndf and Δp-value are the differences in the number of degree freedom and p-value of χ^2 of track fit between two consecutive iterations, respectively.

as follows:

$$\Delta T = \frac{\Delta X}{\overline{V}}, \tag{3.7}$$

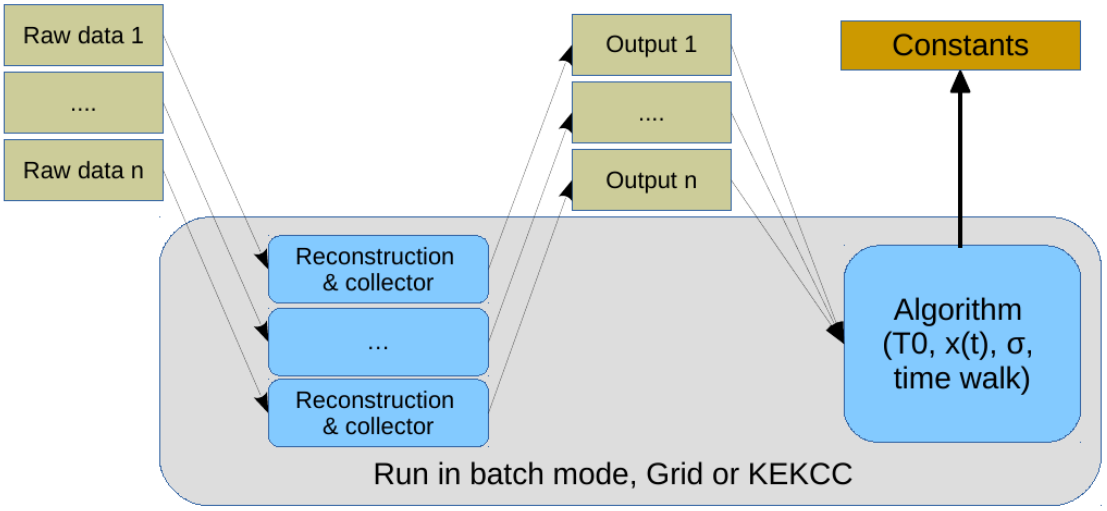

;

Figure 3.22: Data flows and steps in each iteration. Raw data which contains CDC hit information is used for tracking reconstruction. The collector harvests the necessary information for calibration after track fitting and stores it in the output files. The reconstruction is performed in parallel at KEKCC (KEK computing center). The algorithm is then executed over all the output files of the collector to create new constants.

where $\Delta X = |X_{measurement}| - |X_{fit}|$ is the (absolute) residual of track fitting, and $\overline{V}$ is the average drift distance velocity, Because the velocity is not a constant (as can be seen in the x(t) calibration), our T_0 calibration method which is done on the time domain is more precise and robust than that done in Belle.

For Belle II CDC, the x(t) relations have been calibrated for each layer with different incident angles, α, θ and left-right side. For the Belle CDC case, the θ dependence was not considered for the x(t) relation. The α dependence was not fully calibrated for all the bins: only the x(t) relations at α=0 degrees were calibrated, and Garfield simulation results were used for other x(t) relation bins. It is impossible to obtain the ideal gas conditions in the experiment and to simulate all the effects by Garfield, the x(t) relations for the Belle II CDC should be more realistic than that using in the Belle CDC. The 5^{th} Chebyshev polynomial function is adopted for the main region of x(t) relation in our calibration, while the 5^{th} polynomial one was used in Belle CDC.

The position resolution for the Belle II CDC was calibrated for each layer, left-right side, incident angle, and polar angle. However, only the layer dependence was considered in the Belle CDC calibration. This makes the Belle II CDC position resolution more realistic than the resolution obtained for the Belle CDC.

For Belle II CDC the time walk calibration has been done on the time domain and has used an exponential for correction. while it was done in the drift distance domain for Belle CDC case. As explained above, the correction for timing on the time domain would give better results. The time walk effect was corrected with a function $\sim 1/\sqrt{\mathrm{ADC}}$ for the Belle CDC.

3.4 Alignment

Each end-plate of the CDC is divided into three parts: the small cell (super-layer 0), conical (super-layer 1 and 2) and main parts (super-layer 3-8). The main and conical parts are joined together before wire stringing. The small cell part is constructed as an independent chamber [27] and installed into the main chamber which consists of the main and conical parts to complete the CDC. These parts of end-plates might be misaligned with each other. They might be shifted in all the three directions x, y, z and rotate around the z axis. The forward end-plate might also be rotated with respect to the backward end-plate (twist).

The positions of each layer and each wire are also possibly misaligned due to reasons such as the deformation of the end-plates caused by the tension of 56576 wires; the forward position of layers 35-39 (from super-layer 5 and 6) is shifted due to an earthquake happened when drilling the end-plate, as indicated by a measurement; the mechanical imperfection; and the effect of the feed-through. Before starting this alignment, the end-plate deformation is corrected by measured values with the precision of ± 50 μm, and the gravitational wire sag is corrected

using tension data. The gravitation sag is modeled as parabola. The maximum is around 200 μm at the middle of the longest wire.

The misalignment of sense wire positions is divided into three categories:

- Misalignment due to twist: the rotation of the forward end-plate with respect to the backward side.
- Layer-by-layer misalignment: the misalignment between layers.
- Wire-by-wire misalignment: the misalignment between sense wires within a layer.

We start CDC alignment with the layer-by-layer alignment, and then perform the twist alignment. The twist and layer-by-layer alignments are iterated until corrections are small enough. Finally, the position of each wire in the ϕ direction is corrected (wire-by-wire alignment).

3.4.1 Reference for Alignment

Choice of a good reference is the most important key which must be considered before starting any measurement or alignment works. Since the CDC is the main tracking device in Belle II, all the outer detectors will be aligned to the CDC. There is no any external reference for the CDC alignment. The CDC has to be aligned internally. Track-based alignment method which is used for Belle II CDC requires the reference to satisfy the following two conditions:

- The number of layers (hits) is large enough to obtain good quality of track fitting. At least four super-layers which contain two stereo super-layers and two axial super-layers are required: both types of stereo-layer hits are required in track fitting to obtain a reasonable z resolution. The two additional axial super-layers are requested in order to improve the track fit quality.

- The reference is well aligned, or its misalignment is small as much as possible.

The innermost layers (the small chamber and conical part) are supposed to have a large misalignment because of the limitation of mechanical precision as mentioned above. The deformation of the end-plates is getting smaller at the outer layers as they are close to the outer support cylinder. The outermost position of the end-plates serves as the reference for surveying the end-plates deformation. It indicates that the end-plates near the outermost layer are more precisely aligned than that at the inner layers. The effect of a misalignment at the outer layers is smaller than that at the inner layers because of the longer wires. The super-layer 5-8 should not use as the reference because of the earthquake as mentioned above.

Considering the two conditions required and the expectation mentioned above, both the upper and lower sides of the two outermost super-layers are selected for the reference for the first iteration: cosmic-ray track which has hits at the upper and lower sectors is fitted as single track. Thus, a track is fitted with the two outermost super-layers, but the number of hits is the same as using of four super-layers. The upper and lower sides of a stereo super-layer play a role as two different types of stereo super-layers.

3.4.2 x(t) Relation for Alignment

Figure 3.23 sketches the misalignment effect on x(t) relation. The black curve shows a true x(t) relation, that is used to estimate the drift distance for tracking. The gray region shows the data, where the drift distance is estimated by extrapolating the fitted tracks from the reference layers to the given cell. It shifts along the drift distance axis if the cell is misaligned. This shift is defined as residual $\Delta X = X_{\text{measurement}} - X_{\text{fit}}$.

Since x(t) function is obtained from the data, it fits to the data as the red curve in Figure 3.23. That means effects from the systematic misalignment such as rotation, twist are absorbed in the x(t) calibration. To cancel this bias and obtain the x(t) relation as the black curves, data at the left and right are merged for x(t) calibration: assuming that the x(t) relations are identical for the two sides. Because of the requirement of the left-right symmetry, only the cosmic ray data taken without the magnetic field can be used for this alignment. The x(t) calibration should be done separately for the data taken with magnetic field.

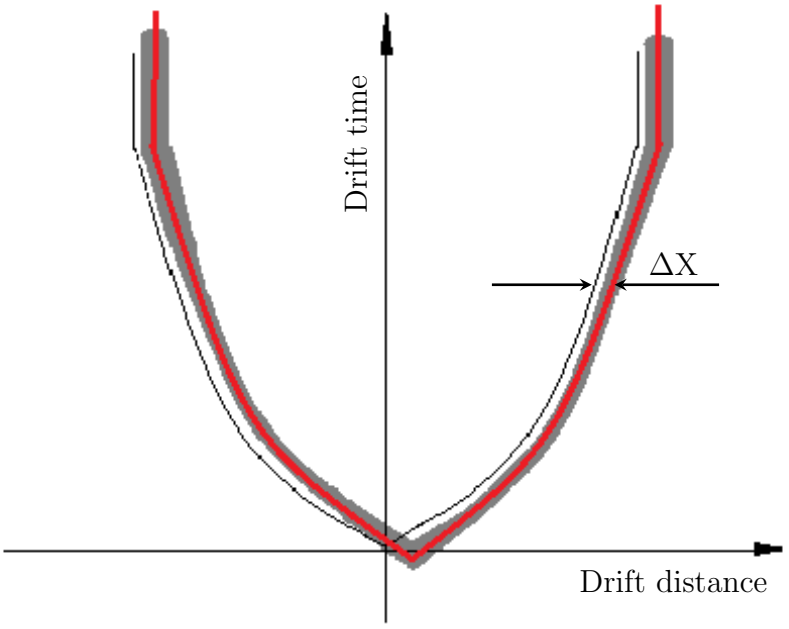

Figure 3.23: The effect of misalignment in x(t) relation. The black curve is the expected x(t) function. The gray region is the data when misalignment happen. The red line are assumed to be x(t) after calibration if x(t) relations of the left and right sides are calibrated separately in the standard way.

3.4.3 The Effect of Misalignment

The layer-by-layer misalignment is described by the following parameters: δx, δy and δz for the shifts in the x, y and z directions, respectively, and $\delta\phi$ for the

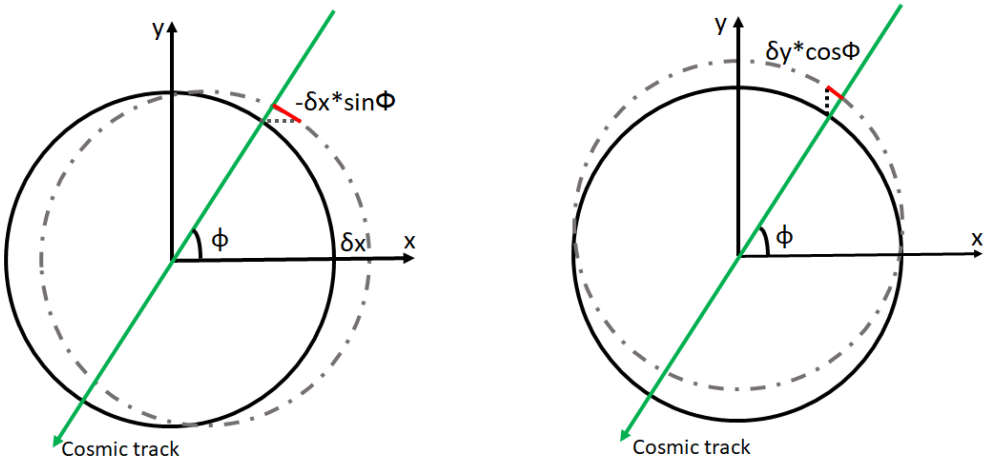

(a) δx shift (b) δy shift

Figure 3.24: The effect caused by δx and δy shifts. The black circles are the designed wire positions in a layer, and the dash-dot circles are the real one. A cosmic-ray track passes through the CDC at the azimuthal angle ϕ. The red line shows the observed residual.

rotation around the z-axis. The wire-by-wire misalignment is described only by x and y shifts.

The misalignment of a wire position causes different effects on the residual ΔX. For a track with small incident angle ($|\alpha| < 5°$), the track azimuthal angle, ϕ, is also the angle of the wire position where the track pass through. The effect of misalignment is described as following:

$$\Delta X_{observed} = -R \sin \delta\phi + \delta x \sin \phi - \delta y \cos \phi, \tag{3.8}$$

where R is the layer radius of the given layer; the first term is for the effect of a rotation $\delta\phi$; and the second and third terms are for the effects of δx and δy shifts, respectively, and depicted in Fig. 3.24.

A shift along the z direction, δz, has no influence for the axial wires, but it causes an effect for stereo wires. The relation between δz shift and the residual of

a stereo wire is shown in Figure 3.25 and approximated as follows:

$$\Delta X_{\mathrm{zshift}} \simeq \delta z \sin \epsilon, \tag{3.9}$$

where ϵ is the stereo angle of the given layer. Since the stereo angles are small (∼70 mrad), the effect caused by δz shift is small and behaves in the same way as that caused by a rotation with a small angle, and it is impossible to distinguish the two effects. Therefore, z-positions of wires are fixed during the calibration.

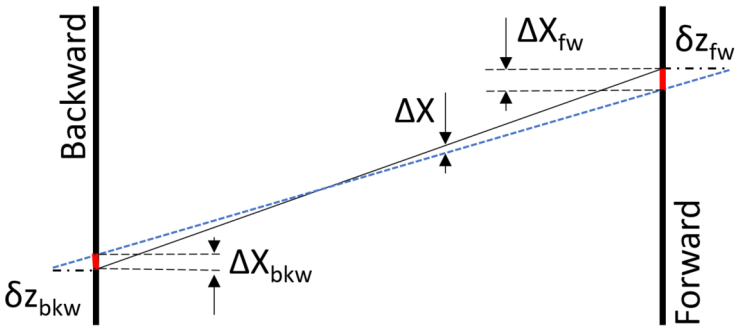

Figure 3.25: Effect of the δz shift. From a misalignment at the forward (backward) side δz_{fw} (δz_{bkw}). A residual ΔX_{fw} (ΔX_{bkw}) will be observed at the forward (backward).

3.4.4 Layer-by-layer Alignment

Vertical cosmic-ray tracks ($70^\circ < \theta < 110^\circ$) are used for this alignment to avoid the effect of the twist misalignment (explain in Section 3.4.5). A cosmic-ray track is fitted with the reference layers. The track is extrapolated to layers which need to be aligned to compute the residual ΔX. Since the extrapolation uncertainty becomes large for a layer far from the reference layers, the alignment results of these layers are bad. Therefore, all layers are aligned step-by-step. One super-layer is considered in one step. Aligned layers are added to the reference and used for track fitting to align the next super-layers. After inner layers are aligned to

outer layers, cosmic-ray tracks are fitted with inner layers to aligned outer layers. These steps are repeated until the corrections are small enough.

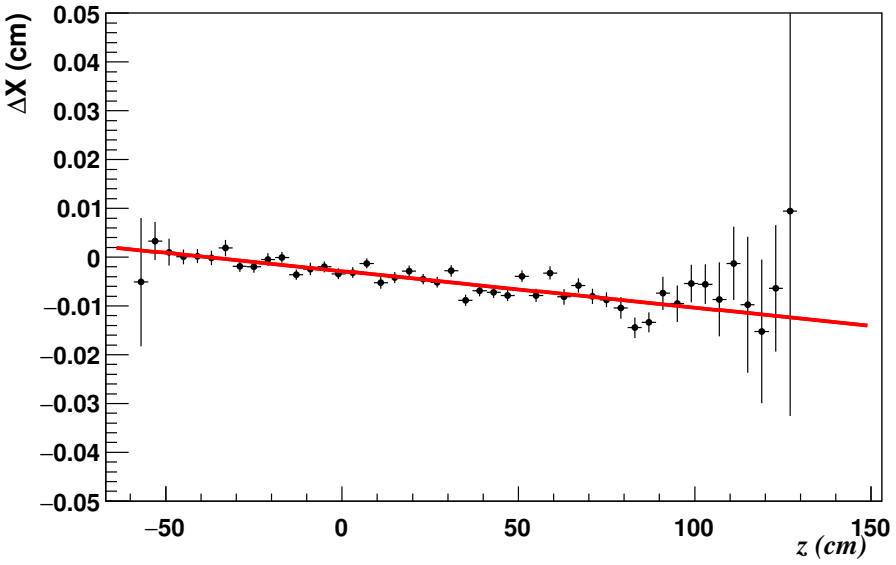

Figure 3.26: Example for the z dependence of residuals (a group of channels 223-337 of layer 38). A linear function (red line) is fitted to the data (black points) to compute the residual at the end-plate positions.

The residual ΔX varies along the z position because the misalignment at the backward and forward end-plates are different. Its values at the end-plate positions relate directly to misalignment. They are determined for each channel or group of few channels by fitting its dependence on the z position with a linear function, as shown in Figure 3.26 for a typical group of channels.

The residuals ΔX at the end-plates positions as a function of the azimuthal angle ϕ of the wire position is shown in Fig. 3.27 for the forward side of the layer 38. It is fitted with the function in Eq. 3.8 to extract the misalignment parameters. The results of all layers are summarized in Fig. 3.28 for the first iteration. The small cell and conical parts are misaligned largely with respect to the reference. Layers 20-25 of the main part are also misaligned slightly because of the mechanical imperfection, but the magnitudes are smaller than those of the inner layers, except slightly large δx shifts at layers 35-39 due to the earthquake as mentioned above.

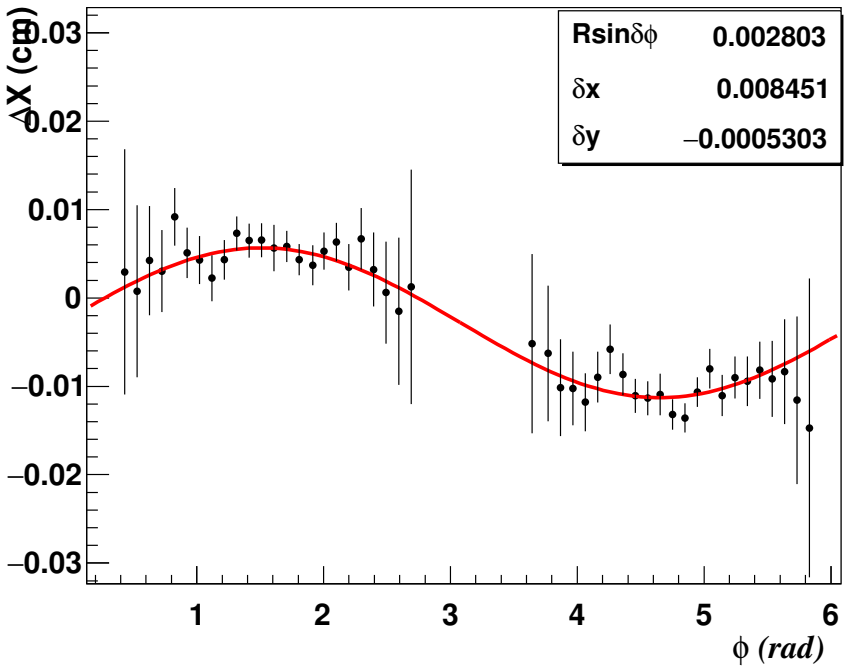

Figure 3.27: Residual ΔX as a function of ϕ for the forward side of layer 38. The black points are the data, and the red line is the fit.

3.4.5 Twist Alignment

Rotation of the forward end-plate with respect to the backward end-plate (twist) has no effect for tracks with $\theta = 90$ degrees but provides an impact proportional to polar angle of a track or $\tan\lambda$ (dip angle). The twist alignment is performed after all the layers of the CDC are aligned for the other effects mentioned in the previous sections. Then, the twist and layer-by-layer alignments are iterated.

To simplify the parameterization, only the axial hits are used for this alignment. When the end-plates are twisted with an angle $\delta\phi$, a given layer with radius R is displaced by $\delta X = R \sin \delta\phi$ at the forward end-plate. Considering a cosmic-ray track which passes through the CDC with at a dip angle λ. This track is fitted with the reference layers and the best fit is obtained at the layer with radius R_0. That means the residual of a hit in this layer is the closest to zero. The layer with the radius R_0 is not required to be a specific layer. This track passes through the reference layer R_0 at the coordinate $z = z_0$ as shown in Figure 3.29. The

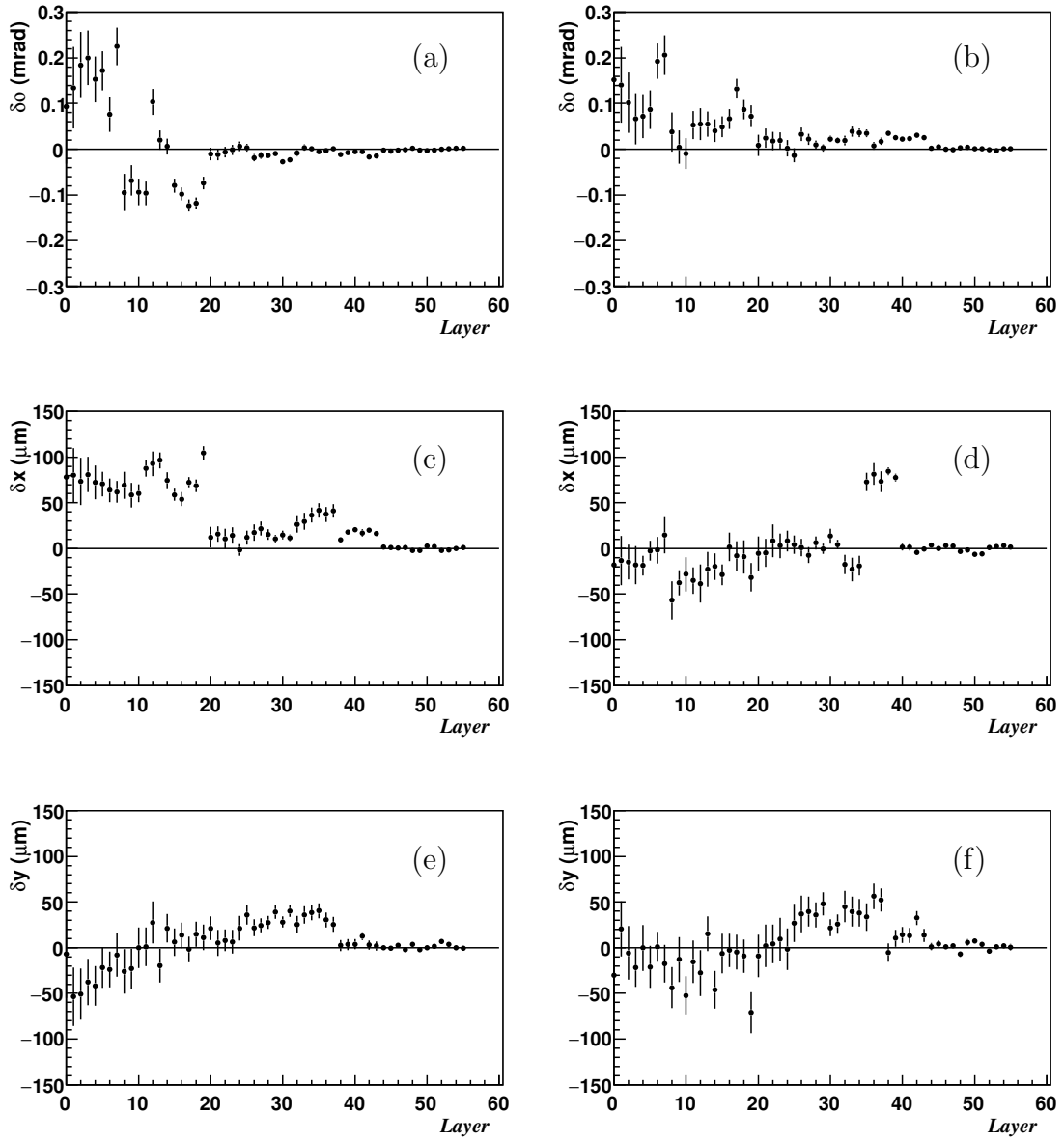

Figure 3.28: Alignment results for the layers with respect to the reference layers. (a) (c) (e): the results of the backward end-plate, and (b) (d) (f): the results of the forward end-plate. (a) and (b) are for the rotation effect $\delta\phi$, (c) and (d) for the δx shift, and (e) and (f) for the δy shift.

misalignment at this location is expressed as:

$$\delta X_{R_0} = \frac{R_0 \sin\delta\phi}{L_0}(z_0 - z_{b0}), \tag{3.10}$$

where L_0 and z_{b0} are the wire length and z-position at the backward end-plate position of this reference layer, respectively. This comic-ray track shall pass a

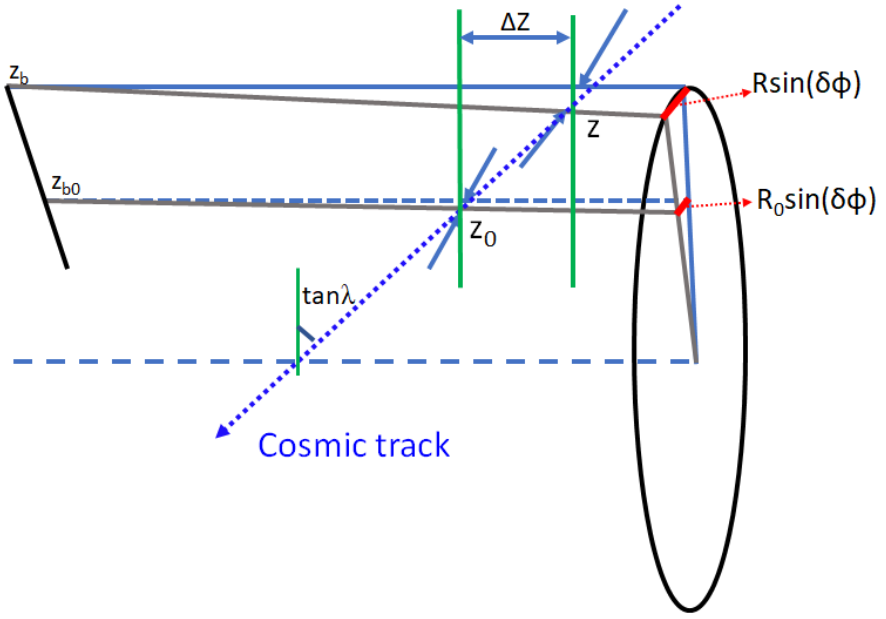

Figure 3.29: Twist effect: the end-plates are twisted an angle $\delta\phi$. A cosmic-ray track passes through the CDC with an dip angle $\tan\lambda$. It passes through the layers which have radii R and R_0 at the z-positions z and z_0, respectively. The backward positions of these two layers are z_b and z_{b0}.

specific layer which has the length L, the radius R and the backward position z_b at the z coordinate at $z = z_0 + (R - R_0)\tan\lambda$. The displacement at this location is:

$$\delta X_R = \frac{R\sin\delta\phi}{L}(z - z_b) = \frac{R\sin\delta\phi}{L}\left[z_0 + (R - R_0)\tan\lambda - z_b\right], \tag{3.11}$$

and the observed residual at this specific layer can be approximated using the difference of δx between the reference and the given layers, as follows:

$$\begin{aligned}\Delta X_R^{observed} &\simeq \delta X_R - \delta X_{R_0} \\ &\simeq \frac{R\sin\delta\phi}{L}(R - R_0)\tan\lambda + \frac{R\sin\delta\phi}{L}(z_0 - z_b) - \frac{R_0\sin\delta\phi}{L_0}(z_0 - z_{b0}).\end{aligned} \tag{3.12}$$

For a given layer, the first term depends on the track direction ($\tan\lambda$) with a coefficient labeled P_1. The other two terms depend on z-position of the hit and

label as P_0. Then, Eq. 3.12 can be re-written as follows:

$$\Delta X_R^{observed} = P_1 \tan\lambda + P_0. \tag{3.13}$$

P_0 is complicated and difficult to use for alignment, because z_b and L are different layer-by-layer. The term $P_1 \tan\lambda$ is be used to extract the twist effect.

Cosmic-ray tracks are fitted with the four innermost super-layers and then extrapolated to the outer layers. Residual ΔX is plotted in a c orrelation with $\tan\lambda$ for each layer. It is then fitted with a linear function. Figure 3.30 shows the dependence of the residual on $\tan\lambda$ for the upper sector of layer 55. The slope coefficient (P_1) depends on the layer radius and wire length as indicated in Eq. 3.12. Quantiy $P_1 L$ depends on the layer radius is fitted with the following function:

$$P_1 L = R^2 \sin\delta\phi - RR_0 \sin\delta\phi \tag{3.14}$$

to extract the twist angle. Where $\sin\delta\phi$ and $R_0 \sin\delta\phi$ are parameters of the fitting. The dependence of the $P_1 L$ term on the layer radius of the upper sector of the CDC after the first iteration is shown in Figure 3.31, the twist angle is obtained to be $+0.218 \pm 0.001$ mrad. The final results from the alignment conclude that the forward end-plate is rotated with an angle $+0.295 \pm 0.001$ mrad.

3.4.6 Wire-by-wire Alignment

Mechanical imperfection such as the precision of the drilling process, the feed-through effect possibly causes different for each wire. Correction for this effect is applied for ϕ position of sense wires using cosmic-ray track with a small incident angle α. Misalignment of the wire position in r is unable to correct because there is not much data with α around 90 degrees (perpendicular to r direction) and the impact of the misalignment in r direction to CDC performance is small, since most

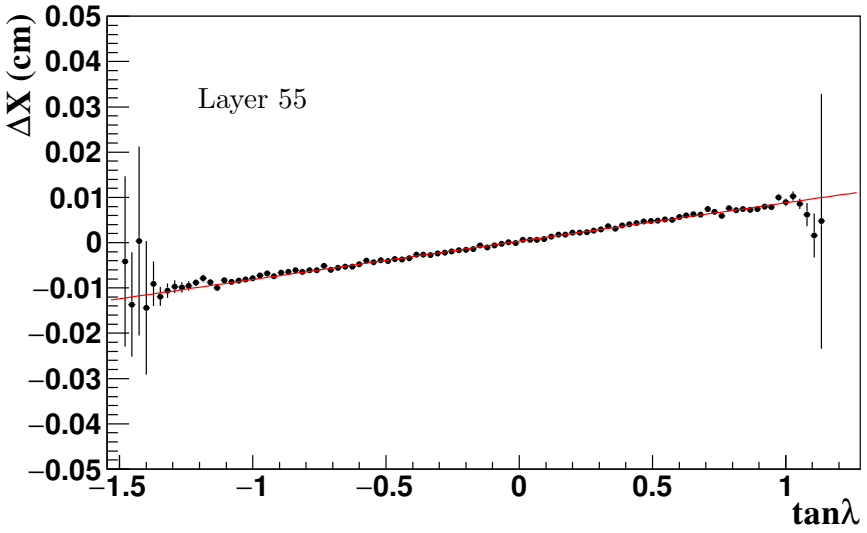

Figure 3.30: The dependence of ΔX on $\tan\lambda$ for the upper sector of layer 55. The black points are the data and the red line is the linear fit.

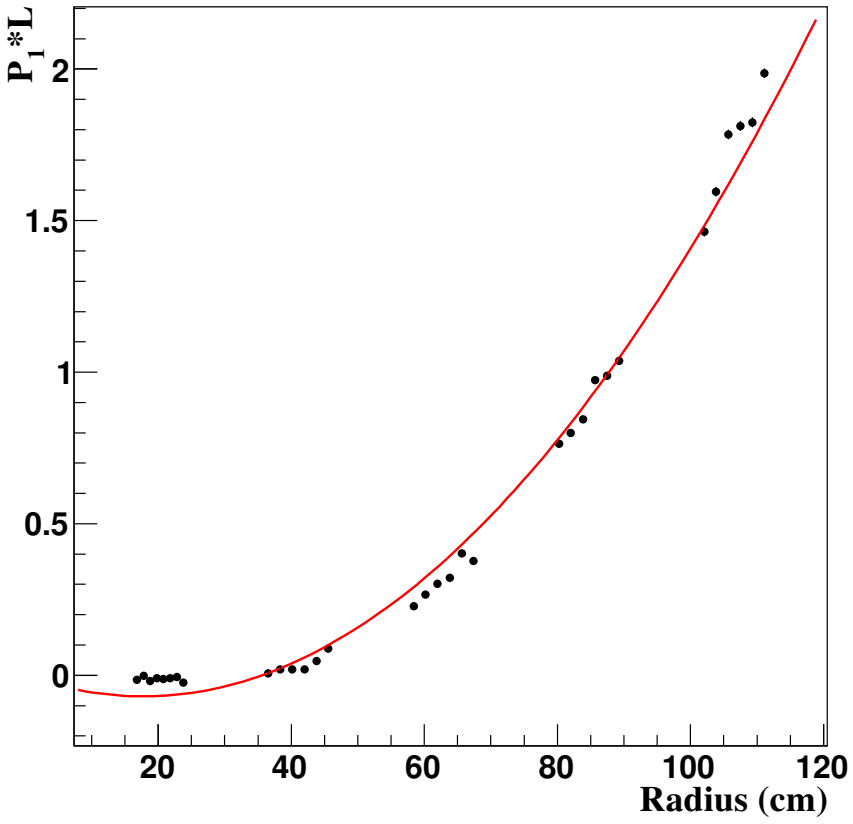

Figure 3.31: The dependence of the $P_1 L$ term on layer radius for the axial layers in the upper sector of the CDC. The data (black points) are fitted with the function of Eq. 3.14.

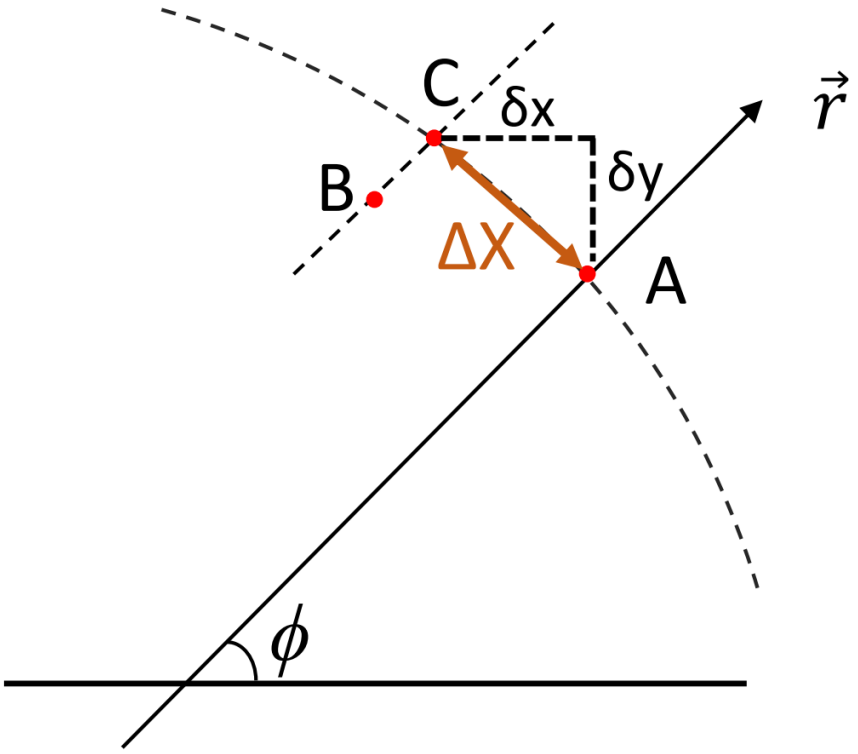

Figure 3.32: Conceptual drawing for wire-by-wire alignment. A is the designed wire position which is used for reconstruction, B is the real position, and C is a new wire position for reconstruction after the correction (δx, δy) applied.

of tracks come radially from the IP in the collision experiment (α ~0 degrees). The method is shown in Figure 3.32. The residual of each wire at the end-plate positions is estimated with the method mentioned in Section 3.4.4. Corrections (δx, δy) are extracted using following formula:

$$\begin{cases} \delta x = -\Delta X \sin\phi \\ \delta y = \Delta X \cos\phi, \end{cases} \tag{3.15}$$

The result of wire-by-wire alignment is shown in Figure 3.33. The means of the residual distributions before the alignment fluctuate, and they are close to zero after the wire-by-wire alignment. The effect of wire-by-wire alignment on the position resolution is shown in Figure 3.34 as a dependence on the drift distance. The resolution is much improved at the middle of the drift distances region, around

0.35 cm in above plot.

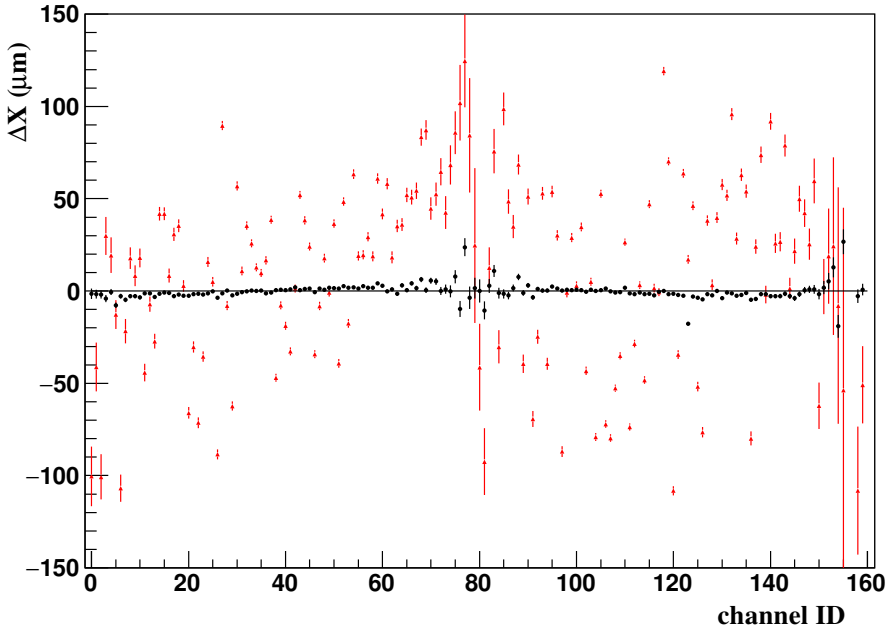

Figure 3.33: Mean-of-residual distribution for the wires of layer 12, where a wire is identified by channel ID. The red triangles show the results before the alignment and the black circles the final results.

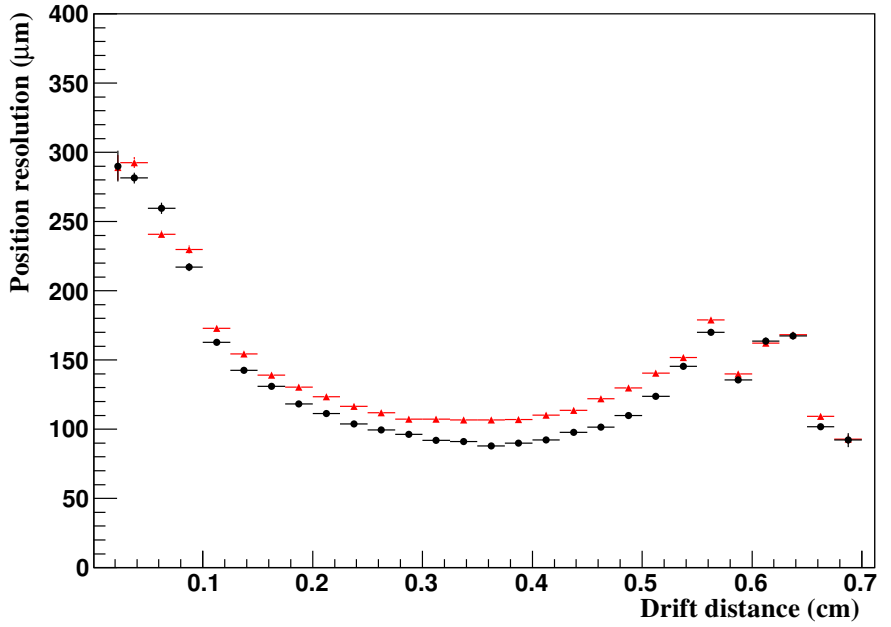

Figure 3.34: Position resolution for wires in layer 12 at $\alpha = 0$ degrees and $\theta = 135$ degrees, obtained with the cosmic-ray data taken without magnetic field. The red triangles (black circles) show the results before (after) the wire-by-wire alignment.

3.4.7 Comparison with the Belle CDC Alignment

The Belle CDC alignment was performed using the x(t) relations from the Garfield simulation, while the x(t) relations for Belle II CDC alignment are obtained from the data. It is unbias the misalignment (explained above). The x(t) relations from the data should more realistic, so it delivers better results than the simulated x(t) relation. The Belle II CDC is aligned internally, that means that only the CDC was used in this alignment. While in the Belle CDC case, the z-position from the SVD detector was used for track fitting. That made the Belle CDC alignment dependent of the SVD alignment.

The CDC has been successfully aligned layer-by-layer by merging upper and lower cosmic tracks and fitting a cosmic-ray track as a single track using the two outermost super-layers as the reference for the first iteration. While only the cathode and inner parts of the Belle CDC were aligned to the main part. The misalignment of the layer-by-layer of the cathode, inner and main parts were not considered in the Belle CDC alignment.

With the success of the layer-by-layer alignment and having a good x(t) relation, the twist and the wire-by-wire alignment for the Belle II CDC have successfully performed, while they were not done for the Belle CDC.

3.5 Performance of CDC

Performance of the CDC is examined by the cosmic-ray data taken under a 1.5 T magnetic field generated by the Belle II solenoid. A cosmic-ray muon which passes through the CDC is fitted to two separate tracks at the upper and at the lower sectors as shown in Figure 3.35. The performance of the CDC is obtained by comparing measured parameters of these two tracks assuming that the track-parameter resolutions of these two tracks are identical. Cosmic-ray events which

pass near the IP region, $|d_0| < 3$ cm and -5 cm $< z_0 < 15$ cm, are selected for this study, and both two tracks are required to have more than 30 associated hits.

The performance is also verified with Monte-Carlo simulation. The cosmic-ray data were taken in parallel with the magnetic field surveillance in the IP region. A B-field mapper, a device for measuring the magnetic field was located inside the CDC, and its material quantity significantly affected the observed CDC performance. Two configurations of simulation are performed. One is simulated with a the presence of the B-Field mapper material, corresponding to the real condition and the other is without the B-Field mapper which provides the intrinsic performance of the CDC. The detail description for the B-field mapper geometry and, its location are shown in Appendix B.

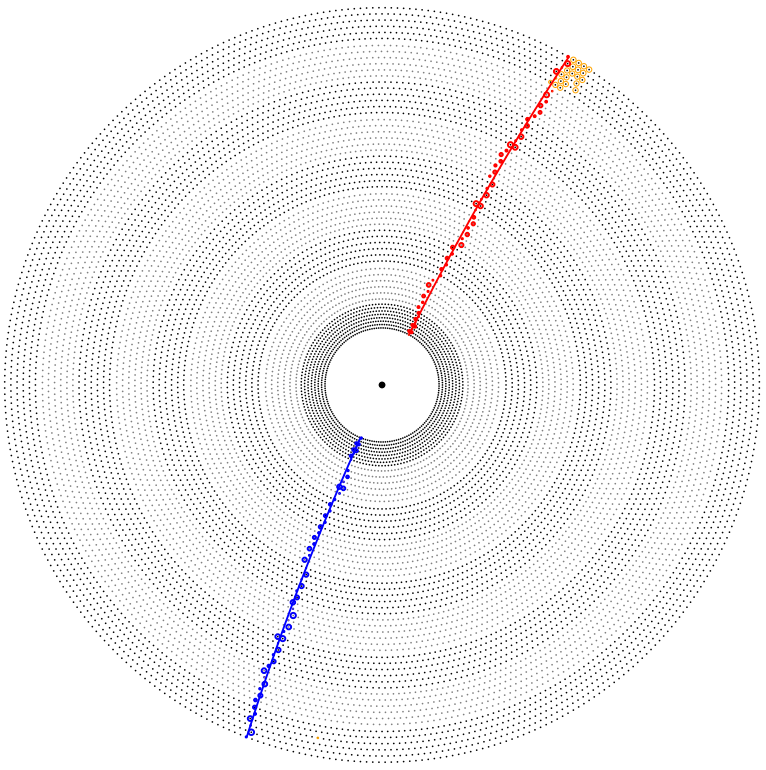

Figure 3.35: A comic-ray event displayed. A single cosmic-ray track is fitted as two separate tracks.

3.5.1 Alignment Results

Figure 3.36 shows the dependence of Δd_0 on tanλ, where Δd_0 is the mean of the difference between d_0 values of the upper and lower tracks. Before the alignment, Δd_0 is shifted to the negative side with a significant dependence on $\tan\lambda$. In contrast, it becomes close to zero for the whole range of $\tan\lambda$ after the alignment. The negative shift and the slope of the dependence are mainly caused by the rotation and a shift of the inner layers with respect to the outer layers, respectively.

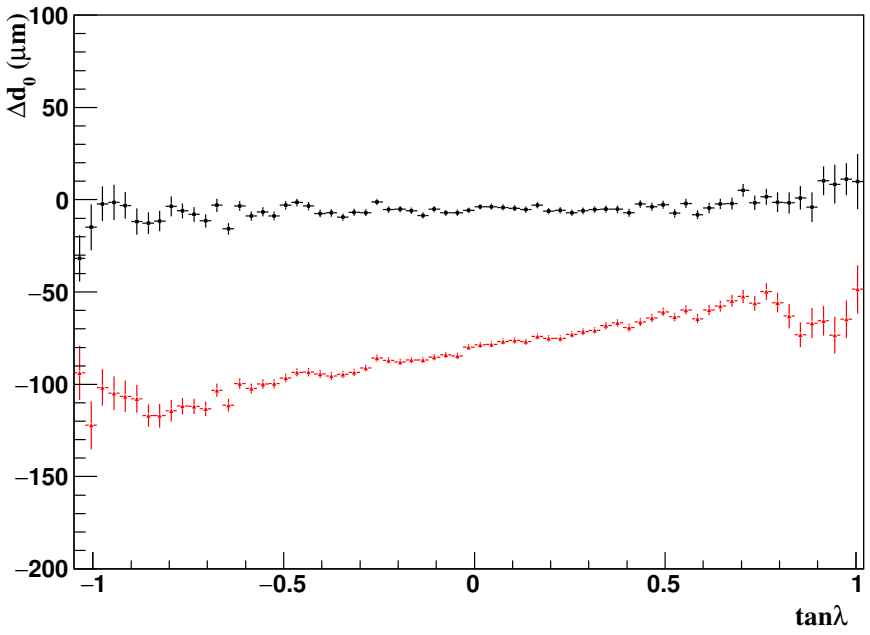

Figure 3.36: The dependence of Δd_0 on tanλ. The red (black) points show the data before (after) the alignment.

The φ_0 dependence of Δz_0 is shown in Figure 3.37, where Δz_0 is the mean of the difference of z_0 between the upper and lower tracks. Before the alignment, it typically fluctuates with a magnitude of 0.3 mm. This fluctuation is caused by the wire by wire misalignment as explained for Figure 3.33. The wire-by-wire position do not only fluctuate but also have a structure. For instance, the group of wires around channel ID 70 in the plot is systematically shifted to the positive side. After the alignment, Δz_0 is almost zero over the whole acceptance. Since statistics

are low for the horizontal region, the corresponding wires near $\varphi_0 = -180$ and $\varphi_0 = 0$ degrees have large errors and large fluctuations even after the alignment.

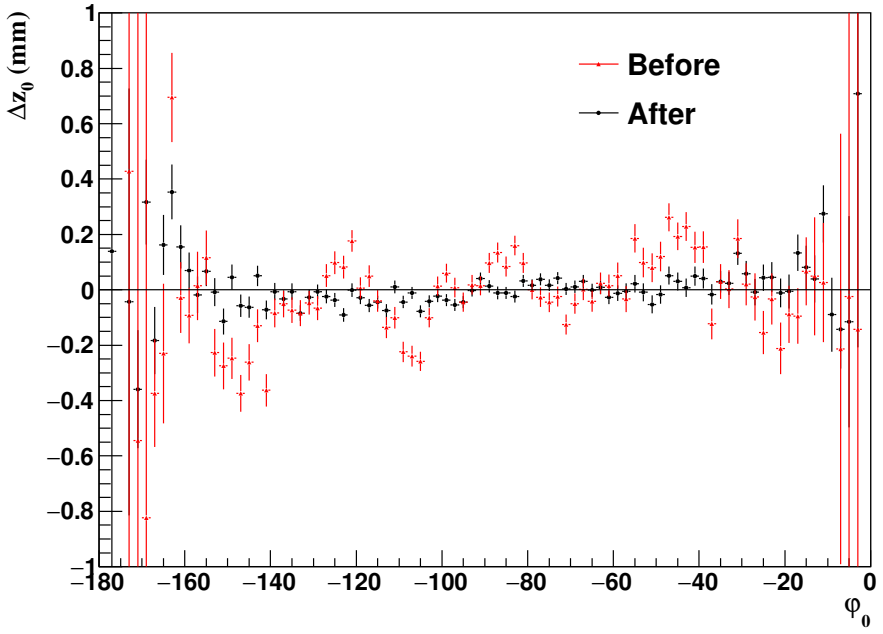

Figure 3.37: The dependence of Δz_0 on φ_0. The red (black) points show the data before (after) the alignment.

3.5.2 Transverse Momentum Resolution

The transverse-momentum of charged particles measured by the CDC is mainly affected by measurement error and multiple scattering. The resolution is formulated as the following:

$$\frac{\sigma_{P_T}}{P_T} = \left(\frac{\sigma_{P_T}}{P_T}\right)_{\text{Meas}} \oplus \left(\frac{\sigma_{P_T}}{P_T}\right)_{\text{MS}}, \tag{3.16}$$

where P_T is transverse momentum in GeV/c, and $\oplus$ denotes adding in quadrature. The measurement error (Meas) relating directly with the position resolution is written as:

$$\left(\frac{\sigma_{P_T}}{P_T}\right)_{\text{Meas}} = \frac{P_T \sigma_{r\phi}}{0.3 L^2 B}\sqrt{\frac{720}{N+4}}, \tag{3.17}$$

where $\sigma_{r\phi}$ is position resolution in meter, B is magnetic field in Tesla, B = 1.5 T for Belle and Belle II, L is lever arm in meter, and N is the number of measurement

points. The multiple scattering effect (MS) is expressed for the Belle II CDC case as following:

$$\left(\frac{\sigma_{P_T}}{P_T}\right)_{MS} = \frac{0.054}{B\sqrt{LX_0}\beta}\left(1 + 0.038\ln\left(\frac{L}{X_0}\right)\right) \tag{3.18}$$

where X_0 is radiation length of material inside the CDC and measured in meter (m). The momentum resolution is parameterized as following:

$$\frac{\sigma_{P_T}}{P_T} = aP_t \oplus b. \tag{3.19}$$

The basic structure and material of the Belle II CDC are similar with those of the Belle CDC. Hence the expected P_T resolution of the Belle II CDC can be estimated by propagating values from the Belle CDC results. The extension of the lever arm and the increase of the number of the measurement points (number of layers) are taken into consideration, the other differences are ignored. The estimation is done as follows:

$$\begin{aligned} a_{b2} &= a_b\left(\frac{L_b}{L_{b2}}\right)^2\sqrt{\frac{N_b+4}{N_{b2}+4}} \\ b_{b2} &\simeq b_b\sqrt{\frac{L_b}{L_{b2}}} \end{aligned} \tag{3.20}$$

where a_b (a_{b2}), b_b (b_{b2}), L_b (L_{b2}) and N_b (N_{b2}) are the measurement error, multiple scattering effect terms, the lever arm, and the number of measurement points of the Belle CDC (Belle II CDC). They are listed in Table 3.3.

Table 3.3: Estimation of the expected momentum resolution as well as the related geometrical parameters of the Belle and Belle II CDC.

Parameters	Belle	Belle II
Radius of innermost sense wire (cm)	8.8	16.8
Radius of outermost sense wire (cm)	86.3	111.14
Lever arm (cm)	77.5	94.34
Number of measurements (Layers)	50	56
Momentum resolution (%)	$0.28P_T \oplus 0.35$	$0.18P_T \oplus 0.32$ (Eq. 3.20) $0.2P_T \oplus 0.3$ (TDR [3])

Using the parameters from Table 3.3 and Eq 3.20, the transverse momentum resolution is estimated as following:

$$\frac{\sigma_{P_T}}{P_T} = \left[0.28\left(\frac{77.5}{94.34}\right)^2\sqrt{\frac{50+4}{56+4}}\right] P_T \oplus \left[0.35\sqrt{\frac{77.5}{94.34}}\right] = 0.18 P_T \oplus 0.32\ (\%). \tag{3.21}$$

The expected performance of σ_{P_T}/P_T is also estimated by assuming the 100 μm for the average position resolution in the Technical Designed Report (TDR) [3]. The results are summarized in Table 3.3

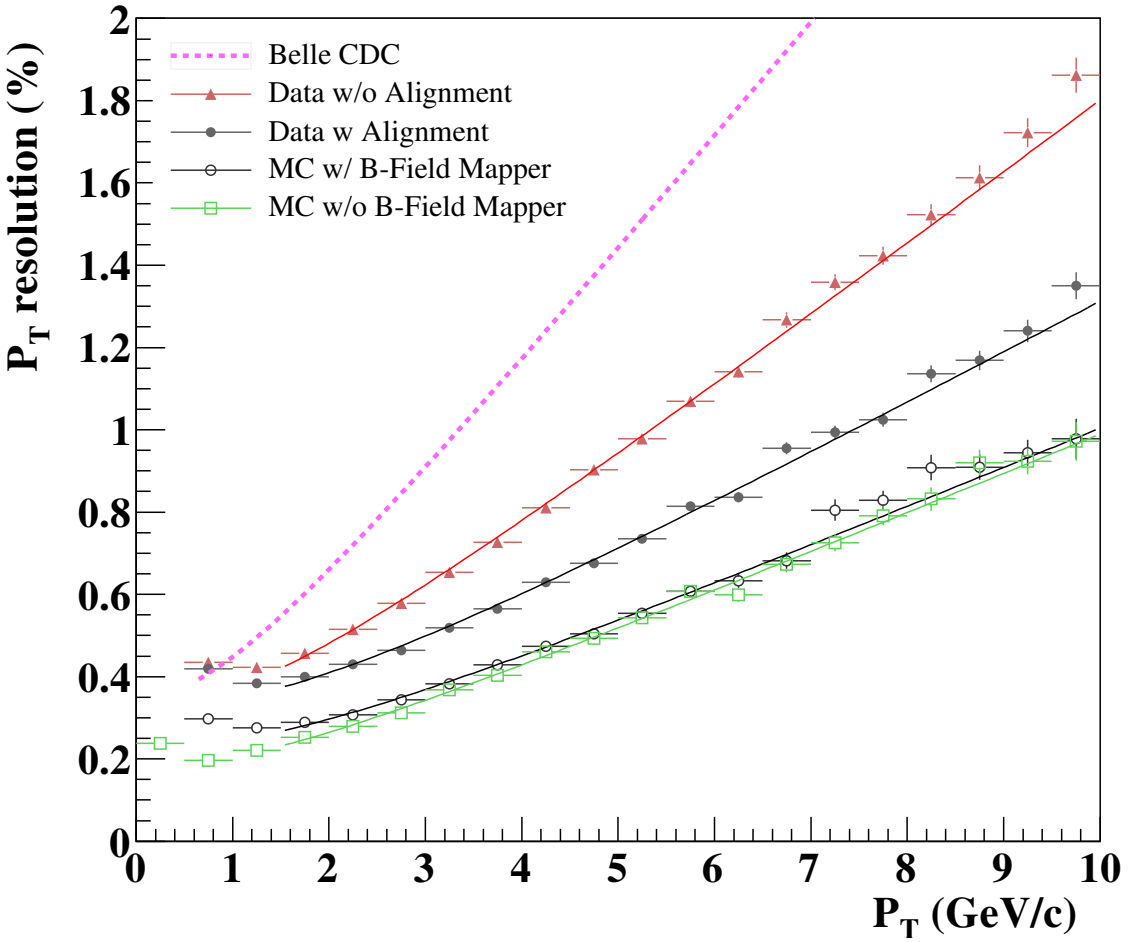

Figure 3.38: P_T dependence of P_T resolution.

For cosmic-ray data case, σ_{P_T} and P_T are estimated from measurement values of the lower (P_T^{lower}) and upper (P_T^{upper}) tracks using the relation $\sigma_{P_T} = \sigma[(P_T^{upper} - P_T^{lower})]/\sqrt{2}$ and the average value, $P_T = (P_T^{upper} + P_T^{lower})/2$, where

$\sigma[\left(\mathrm{P_T^{upper}} - \mathrm{P_T^{lower}}\right)]$ is a standard deviation of the $\mathrm{P_T}$ difference distribution. Thus, the momentum resolution is estimated as following:

$$\frac{\sigma_{\mathrm{P_T}}}{\mathrm{P_T}} = \sigma\left[\frac{\sqrt{2}\left(\mathrm{P_T^{upper}} - \mathrm{P_T^{lower}}\right)}{\mathrm{P_T^{upper}} + \mathrm{P_T^{lower}}}\right]. \tag{3.22}$$

The $\mathrm{P_T}$ dependence of $\Delta\mathrm{P_T}/\sqrt{2}\mathrm{P_T}$ for samples in every 0.5 GeV/c $\mathrm{P_T}$ bin width is fitted by a Gaussian function to obtain the resolution. Results of the data and Monte-Carlo (MC) expectations are shown in Figure 3.38. The MC results indicate that the material of the B-field mapper causes large degradation of the $\mathrm{P_T}$ resolution. For example, $\mathrm{P_T}$ resolution is degraded from 0.2% to 0.3% at $P_T = 0.75$ GeV/c. The effect is large in the low $\mathrm{P_T}$ region and gets smaller in high P_T region.

The dependence of $\mathrm{P_T}$ resolution on $\mathrm{P_T}$ of real data before the alignment is parameterized as $(0.177 \pm 0.001)\,\mathrm{P_T} \oplus (0.325 \pm 0.005)\,(\%)$ ($\mathrm{P_T}$ in GeV/c). It is greatly improved after the alignment and becomes $(0.127 \pm 0.001)\,\mathrm{P_T} \oplus (0.321 \pm 0.003)\,(\%)$. The constant term originating from the multiple scattering effect is almost the same as that before the alignment. But the slope term which is due to the measurement error is improved enormously from 0.177 to 0.127.

In comparison with the result of the Belle CDC, the measurement error term is much better. It is also much better than the expected performance which the extrapolated from the Belle CDC result mentioned above. This improvement is the benefits from the increase of the outer radius of the CDC and the improvements of the new calibration and alignment procedures. The constant term is slightly worse than the expectation because of the multiple scattering on the B-field mapper.

In comparison with the MC expectation, the slope term for the data after the alignment are worse than the MC results about 20%. However, the constant term shows large discrepancy with the MC results. There are some reasons that

would lead to this difference such as the imperfection of the magnetic field map and the geometry of the B field mapper which were used in the reconstruction. In addition, some remaining sources of small misalignment such as the imperfect gravitation sag correction, misalignment in r direction might exist and tail effect of the residual at the short drift distance region is still ignored in the simulation.

3.5.3 Resolution of other Track Parameters

Resolutions of the other helix parameters, d_0, z_0, $\tan\lambda$ and φ_0 are obtained from the standard deviation of the difference of the measurement values between the upper and lower tracks. For example, $\mathrm{d_0}$ resolution is the standard deviation of $\Delta\mathrm{d_0}$ distribution, $\sigma_{\mathrm{d_0}} = \sigma\left[\Delta\mathrm{d_0}\right]/\sqrt{2}$, where $\Delta\mathrm{d_0}$ distribution is fitted with a Gaussian function to obtain $\sigma\left[\Delta d_0\right]$. The dependence of track parameter resolutions on the transverse momentum ($\mathrm{P_T}$) for both the data and MC expectations are shown, respectively, for $\mathrm{d_0}$ (Figure 3.39), $\mathrm{z_0}$ (Figure 3.40), $\tan\lambda$ (Figure 3.41) and φ_0 (Figure 3.42).

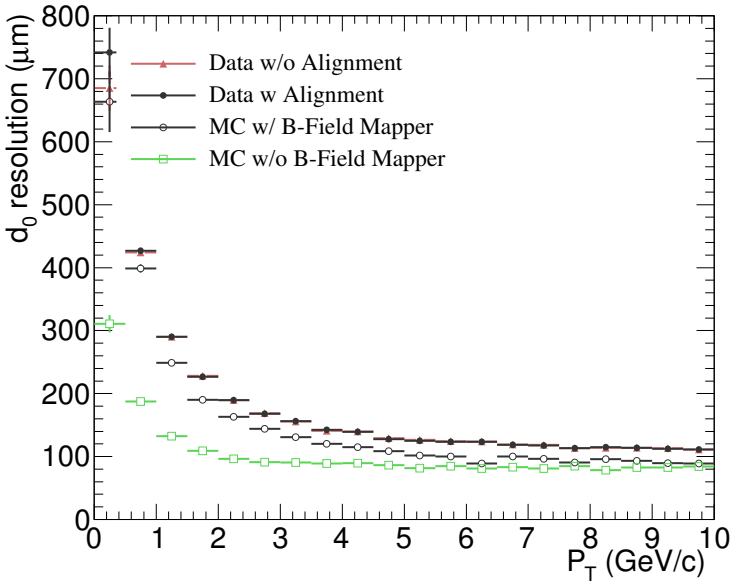

Figure 3.39: $\mathrm{d_0}$ resolution as a function of transverse momentum.

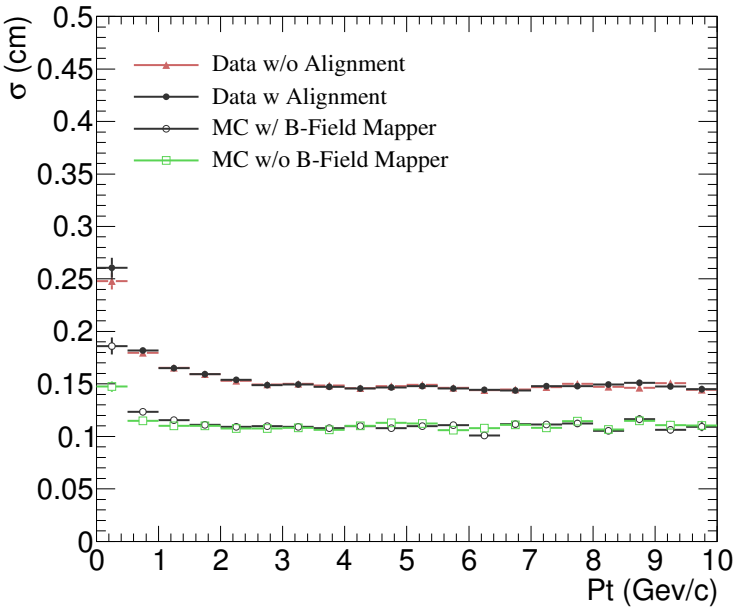

Figure 3.40: z_0 resolution as a function of transverse momentum.

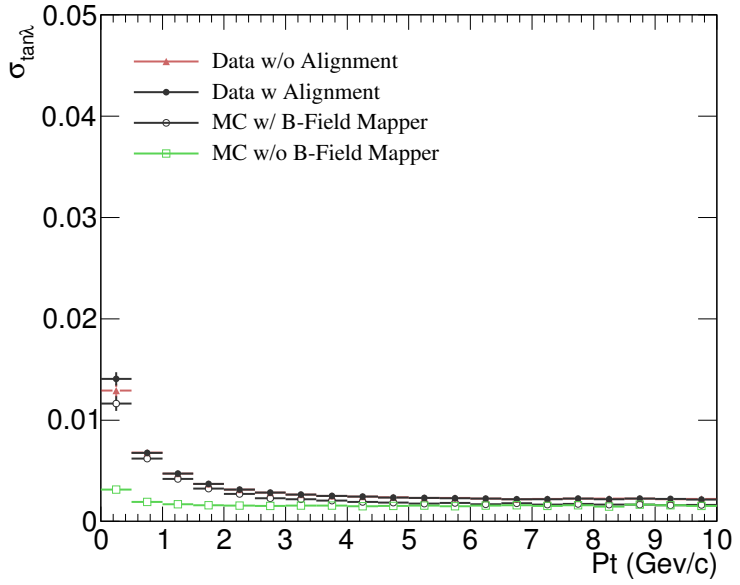

Figure 3.41: tanλ resolution as a function of transverse momentum.

Because of the multiple scattering effect, the resolutions are degraded in the low P_T region and saturate in the high P_T region. For example, σ_{d_0} ~120 μm is obtained for $P_T > 5$ GeV/c. A large effect of the multiple scattering can be seen in the φ_0 resolution. The track parameter resolutions are in agreement with the MC expectations within about 20% except the z_0 resolution. The tendency of the z_0 resolution is the same as that observed in the P_T resolution. Unlike those of the

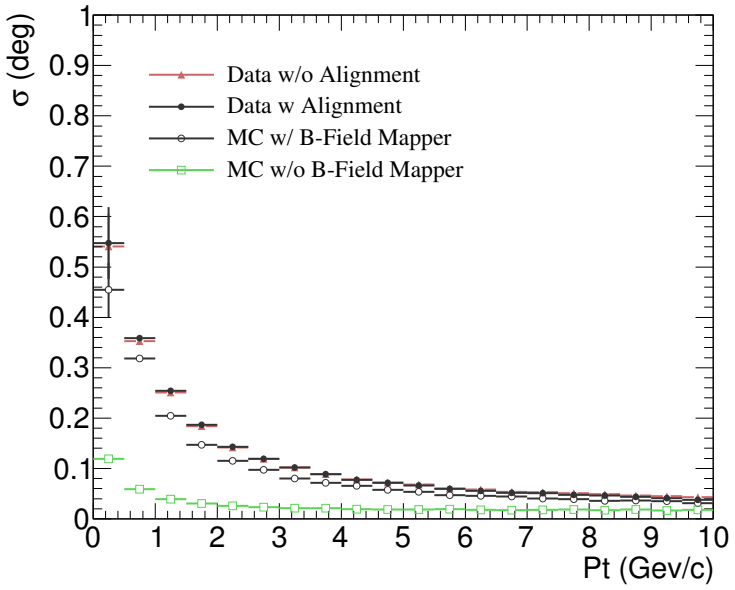

Figure 3.42: φ_0 resolution as a function of transverse momentum.

other parameters, influence of position resolution is dominant in the z_0 resolution, as the z_0 resolution is not so much degraded in the low P_T region where the effect of multiple scattering is large.

Chapter 4

LFV Analysis

When electrons collide with positrons at the SuperKEKB accelerator, many different physics processes will occur, including a wide range of event types such as B^+B^-, $\bar{B}^0B^0$, $q\bar{q}(q = u, d, s, c)$, $\tau^+\tau^-$ pair, $\mu^-\mu^+$ pair, two-photon processes and so on. Among these physics processes, we hope to find the signal of the decay $\tau \to \mu\mu\mu$. In this chapter, the decay $\tau \to \mu\mu\mu$ is referred as the signal process and the other processes as background. All the decay processes which are mentioned in this chapter include the corresponding charge-conjugate final states, unless otherwise stated.

4.1 Monte-Carlo Production

Monte-Carlo (MC) sample is used to investigate selection criteria for the signal candidates and to estimate the efficiency of the analysis procedure. Basf2 is under active development, for instance, new features are added to make the simulation more realistic and also improve the performance (e.g. tracking efficiency, resolutions) of the reconstruction algorithm. In this study release-00-08-00 of basf2 software [42] is used to generate data and analysis. The signal and background

events are generated by physics generators as listed in Table 4.1. The detector response is simulated by Geant4 [35], and the simulated signal hits in each sub-detector are then digitized in basf2. The output of simulation has the same record format as that used for the real data. The reconstruction of charged tracks, clusters and particle ID etc. is then performed, and then the output is stored. To reduce the file size, only information which are necessary for physics analysis is stored in a set of data files, which is called mdst data (mini data storage). Beam-associated background hits are embedded in the signal hits before digitization to take into account pile-up effect of background and signal hits.

4.1.1 Beam Background

Beam backgrounds are one of the big concerns of the SuperKEKB, which is designed to operate at 40 times higher luminosity than that in KEKB. The beam backgrounds are predicted increasing drastically at SuperKEKB as compare with KEKB. The background simulation study is ongoing during this time, typically new features are added to make the simulation more realistic. In this study, background data of the 12^{th} simulated background campaign is used [42]. This campaign is close to the lasted one and expected to be the most realistic at the present. The simulated background data will be replaced by the real background data, which will be taken using the random trigger during the SuperKEKB operations.

There are five main effects at the SuperKEK which are predicted to produce a huge background in the Belle II experiment:

• **Beam-gas scattering**: This is the scattering of beam particles on residual molecules in the beam pipe. It can occur via two types of processes: coulomb scattering which changes the direction of the beam particles; and Bremsstrahlung

which reduces the beam energy. The beam particles then hit the wall of the beam pipe and makes showers. The rate is proportional to product of the beam current and vacuum pressure.

• **Touschek effect**: This is the intra-beam scattering which is the scattering of two particles in the same bunch. The transverse momenta are transferred into the longitudinal component. As a result, the energy of the two particles deviates from the nominal energy. They do not obey the designed optics and hit the beam pipe wall. The rate is proportional to the number of bunches and square of the beam current and is inversely proportional to the beam size and the cubic of the beam energy. With the doubled beam current and the smaller beam size, the Touschek rate at SuperKEKB is predicted about 20 times higher than that at KEKB.

• **Radiative Bhabha**: The third beam background source is radiative Bhabha scattering. Its rate increases proportionally to the luminosity. Photons from the radiative Bhabha process propagate along the beam directions and hit beam pipes. Electrons and positrons lose their energy after the scattering. They also hit the beam pipe and make showers.

• **Two photon process**: The fourth beam background is the two-photon process where a low momentum electron-positron pair is produced. They spiral inside the tracking detectors and leave a lot of hits. The primary electrons and positrons lose some amount of the energy or scatter with some angles and behave in the same way as in the radiative Bhabha case.

• **Synchrotron radiation**: The power of synchrotron radiation is proportional to the fourth power of the beam energy and the square of the magnetic field strength, so this source is significant from the electron beam at SuperKEKB. Since photon energy is very low ($\sim$20 keV), this background mainly affects the vertex detector.

The beam pipes (at the IP) and collimators are designed to block synchrotron radiation from the beams.

4.1.2 Monte-Carlo Generation for Signal and Physics Backgrounds

Signal MC samples are generated by KKMC/TAUOLA [43]. The $\tau^+\tau^-$ pairs are generated via the process $e^+e^- \to \tau^+\tau^-(\gamma)$. One of the τ's is then forced to decay to three muons $\tau \to \mu\mu\mu$ (signal side), and the other τ decays into various final-states according to the known branching fractions [44] (tag side), which is called generic decay. In total 100 000 signal events are generated.

The Belle II experiment is planned to run for 10 years and to accumulate an integrated luminosity of 50 ab^{-1}. It is impossible to simulate an analysis with the full expected data at this stage due to the lack of computing resource, and that is unnecessary. The analysis is performed using a certain amount of data. The results can be extrapolated to the expected luminosity. In this study, 1 ab^{-1} MC data is used, it is equivalent to the 10-year accumulated data of the Belle experiment.

For the main physics processes which have large cross section such as $B\overline{B}$, $\tau^+\tau^-$ and $q\overline{q}$ ($q = u, d, s, c$), the 8$^{\text{th}}$ campaign MC data (MC8) generated by the central data production of Belle II [42] are used in this analysis. The data correspond to 0.8 ab^{-1}. Results is scaled to 1 ab^{-1} at the final stage. Other types of processes which have large possibility to be fake signals such as $\mu^+\mu^-(\gamma)$ and two-photon processes are generated with a large number of events, however, due to their large cross sections, its scale factor is large. The cross section, the number of generated events, the scale factor and generator name for all the processes are summarized in Table 4.1.

Table 4.1: The cross section, the number of generated events and other parameters as well as the MC generator for the signal and background MC generations.

Process type	cross-section (nb)	Generated (10^6)	Scale for 1 ab^{-1}	Generator
Signal †	–	0.1	–	KKMC
$\Upsilon(4S)$	1.05 ± 0.10			
$\to B^+B^-$	$Br(0.514 \pm 0.006)$[44]	427.68	1.25	EvtGen
$\to B^0\bar{B}^0$	$Br(0.486 \pm 0.006)$[44]	452.32	1.25	EvtGen
$u\bar{u}(\gamma)$	1.61	1284	1.25	KKMC
$d\bar{d}(\gamma)$	0.40	320.8	1.25	KKMC
$s\bar{s}(\gamma)$	0.38	306.4	1.25	KKMC
$c\bar{c}(\gamma)$	1.30	1063.2	1.25	KKMC
$\tau^+\tau^-(\gamma)$	0.919 ± 0.003[45]	735.2	1.25	KKMC
$\mu^+\mu^-(\gamma)$	1.147 ± 0.005 [45]	400	28.68	KKMC
Bhabha	123.5	200	6175	BABAYAGA.NL0
$e^+e^-e^+e^-$	40.9	200	204.5	AAFH
$e^+e^-\mu^+\mu^-$	18.9	400	47.25	AAFH

† $\tau^\pm \to \mu^\pm\mu^+\mu^-$; $\tau^\pm \to generic$

4.2 Event Selection and τ Reconstruction

4.2.1 Track Selection

Under the high beam background environment a single charged particle trajectory is possibly reconstructed as two or more separate tracks. The best one should be used, and the others should be rejected as the case of background tracks. In order to do that, each reconstructed track is required to come from the vicinity of the IP, that is, the helix parameters are in the region $|d_0| < 0.08$ cm and $|z_0| < 0.15$ cm. These requirements also reject tracks from photon conversion. The d_0 and z_0 distributions for the signal MC events are shown in Figure 4.1.

The number of tracks in each signal event before and after applying the selection on the helix parameters is shown in Figure 4.2 for both cases without and with the presence of the beam backgrounds. For the case when the beam backgrounds are absent, the numbers of four-track events (our interest) before and after applying the track selection are almost similar, while the difference is

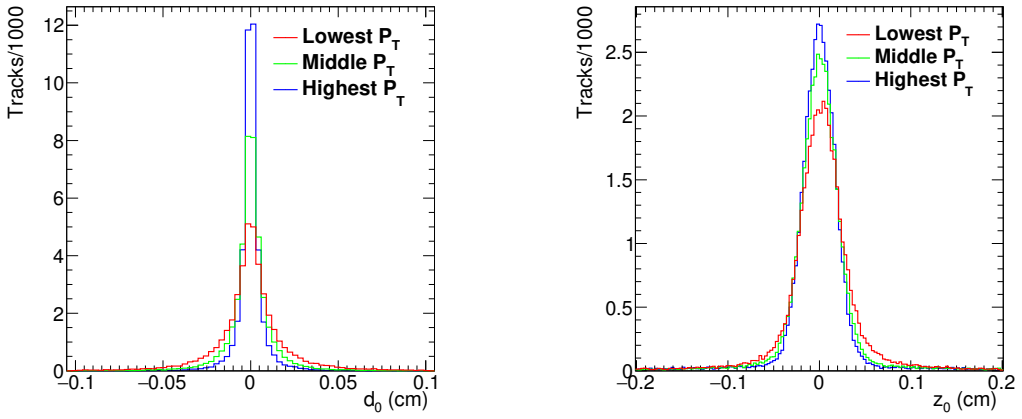

(a) (b)

Figure 4.1: Helix parameter distributions for the tracks originated from the daughters in the $\tau^\pm \to \mu^\pm\mu^-\mu^+$ decays: (a) d_0 - distance of the closest approach in the x-y plane, and (b) z_0 - that in the z direction.

large when the beam backgrounds are embedded in the simulation. The number of four-track events increases significantly after applying the track selection, because clone and background tracks are rejected. However, it is still lower than that of the case where beam backgrounds are absent. The number of four-track events before the filtering for the case without (with) beam background is 54000 (32000), and it is 58000 (44000) after the filtering. It implies that the beam backgrounds largely degrade the efficiency of the analysis. Distribution of the number of tracks in an event for physics backgrounds from $B\bar{B}$, μ-pair, Bhabha, two-photon processes, the continuum ($udsc$ quark-pair) and τ-pair are shown in Figures 4.3 and 4.4. The number of tracks in an event is large in the $B\bar{B}$ and continuum processes events, while it is small in the two-photon, Bhabha and μ-pair processes, where the number of tracks is less than four for most of the events.

4.2.2 Reconstruction of τ

The decay $\tau \to \mu\mu\mu$ is selected and reconstructed using four-track events in which the tag side τ is one prong decay. It means that the tag side decays to only one charge track and neutral products such as photon or neutrino ($\tau \to$

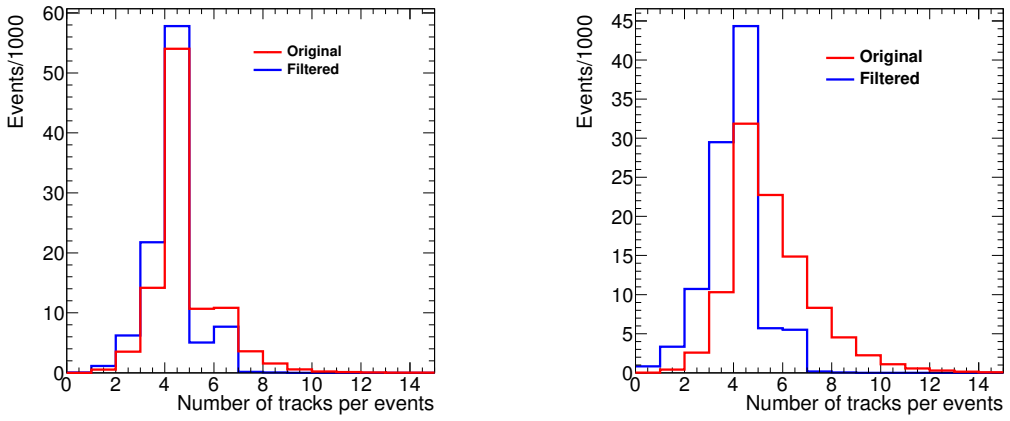

(a) Without beam background (b) With beam background

Figure 4.2: Distributions of the number of tracks in an event before and after applying the track selection for the signal MC sample (a) without and (b) with the present of the beam background cases.

$\mu\bar{\nu}_\mu\nu_\tau$, $e\bar{\nu}_e\nu_\tau$, $\pi\nu_\tau$, $\rho\nu_\tau$, $\pi^-\pi^0\pi^0\nu_\tau$). An event display of an MC event is shown in Figure 4.5. The total branching fraction of the one prong decays of τ in the SM is approximately 85 % [44].

After applying the track selection on d_0 and z_0, events which have four good tracks are selected for reconstructing τ signal. The total charge of these four tracks is required to be zero because they are assumed coming from the decay of $\tau^+\tau^-$. Thrust axis of the event is then calculated using all the reconstructed charged tracks and photons which have energy larger than 0.1 GeV, $E_\gamma > 0.1$ GeV. The thrust axis (vector) $\overrightarrow{T}$ of an N-particles system is defined as a unit vector along which the total projection of the momentum of all the particles has a maximum value. The thrust scalar or thrust is defined as

$$T = \frac{\sum_{i=1}^{N} |\overrightarrow{T} \cdot \overrightarrow{p_i}|}{\sum_{i=1}^{N} |\overrightarrow{p_i}|}, \tag{4.1}$$

where $\overrightarrow{p_i}$ is momentum of the i^{th} particle. The momenta are measured in the center of mass system of the e^+e^- beams. Thrust value distribution for the signal MC event is shown in Figure 4.6.

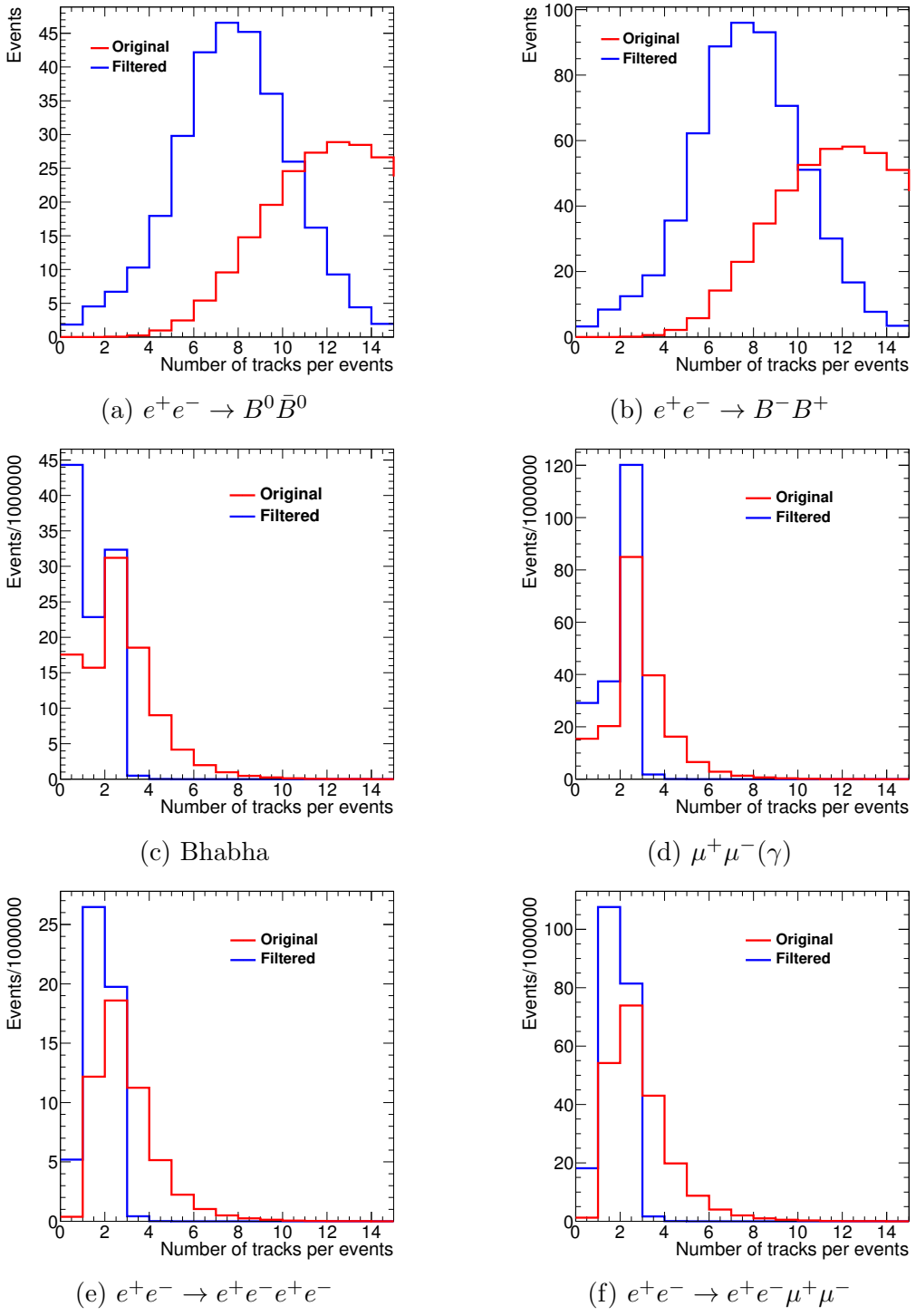

(a) $e^+e^- \to B^0\bar{B}^0$ (b) $e^+e^- \to B^-B^+$

(c) Bhabha (d) $\mu^+\mu^-(\gamma)$

(e) $e^+e^- \to e^+e^-e^+e^-$ (f) $e^+e^- \to e^+e^-\mu^+\mu^-$

Figure 4.3: Distributions of the number of tracks in an event before and after applying the track selection for $B\bar{B}$ and other processes.

The charged tracks and photons in a four-track event are then separated into two hemispheres, which are referred as the signal and tag sides using the plane perpendicular to the thrust axis. The side which contains one charged track

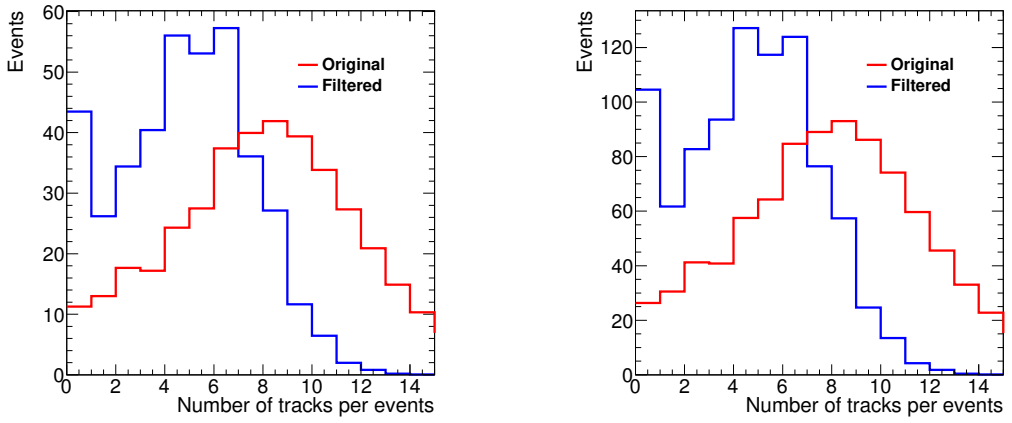

(a) $e^+e^- \to u\bar{u}(\gamma)$

(b) $e^+e^- \to d\bar{d}(\gamma)$

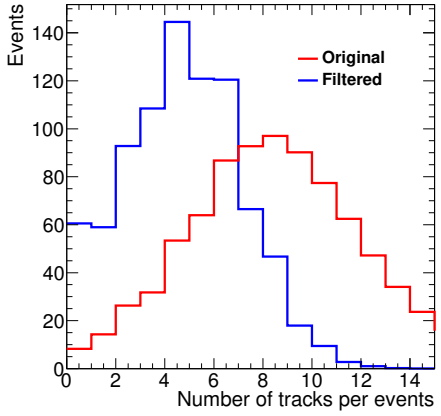

(c) $e^+e^- \to c\bar{c}(\gamma)$

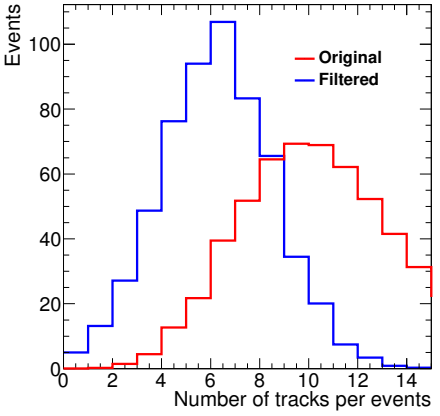

(d) $e^+e^- \to s\bar{s}(\gamma)$

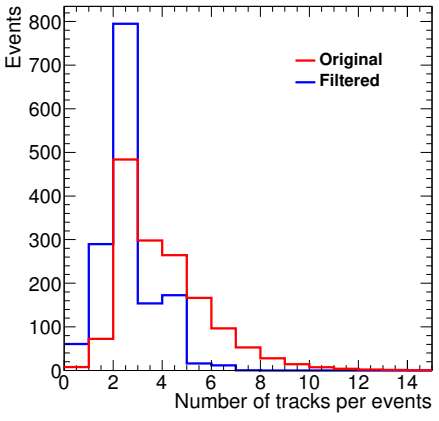

(e) $e^+e^- \to \tau^+\tau^-(\gamma)$

Figure 4.4: Distributions of the number of tracks in an events before and after applying the track selection for the continuum processes ($udsc$ quark-pair) and τ-pair.

is assigned to the tag side and the other which has three charged tracks is the signal side. The idea is described as in Figure 4.7. Events which have a topology of 2-2 tracks are abandoned in this analysis, since the fraction of this event type

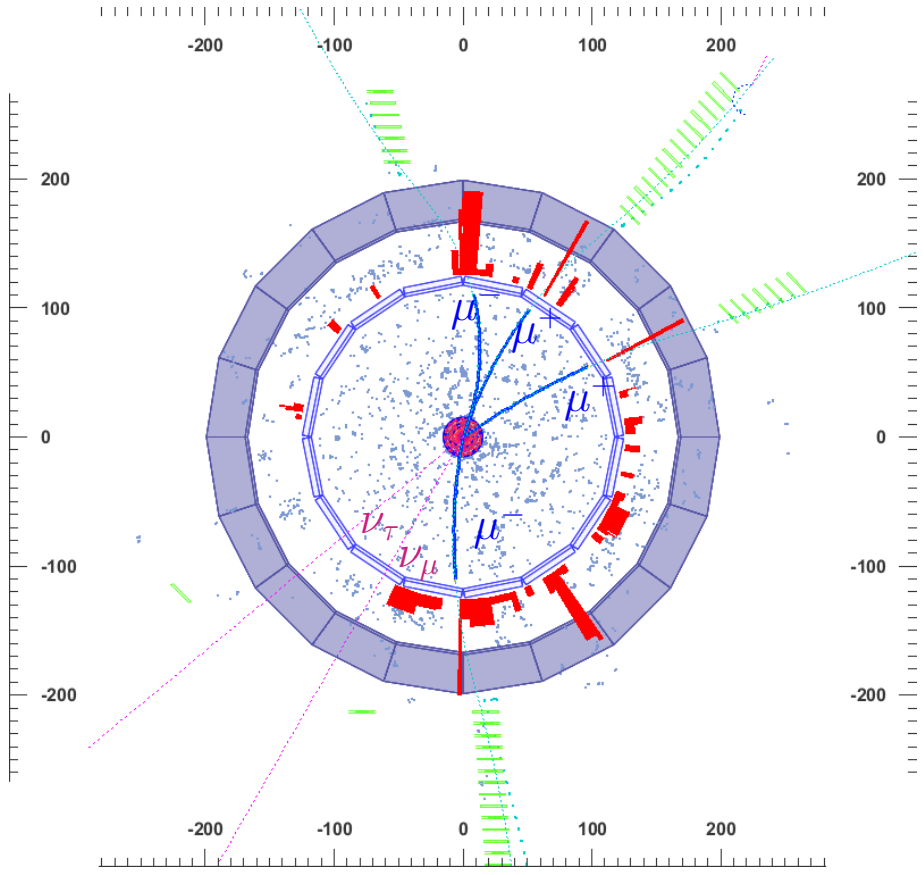

Figure 4.5: Event display for a lepton flavor violation event in r-ϕ view: the signal side $\tau^+ \to \mu^-\mu^+\mu^+$ and the tag side $\tau^- \to \mu^-\bar{\nu}_\mu\nu_\tau$. The green bars show KLM clusters, the red bars show ECL clusters of signal and background particles, and the blue-gray dots show beam background hits.

is very small.

The reconstructed invariant mass for the signal side τ candidate, $M_{\mu\mu\mu}$, and its energy difference, ΔE, are defined as follows:

$$M_{\mu\mu\mu} = \sqrt{E_{3\mu}^2 - p_{3\mu}^2} \tag{4.2}$$

and

$$\Delta E = E_{3\mu} - \frac{E_{beam}^{cms}}{2}, \tag{4.3}$$

where $E_{3\mu}$ and $p_{3\mu}$ are the energy and momentum in the CMS, respectively, of the signal τ candidate, which is reconstructed from the three charged tracks at the signal side using a muon hypothesis, and E_{beam}^{cms} is the total beam energy. Events

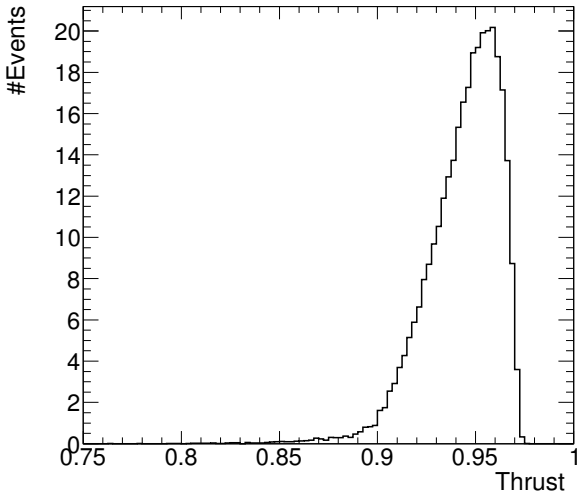

Figure 4.6: Thrust distribution for the signal events.

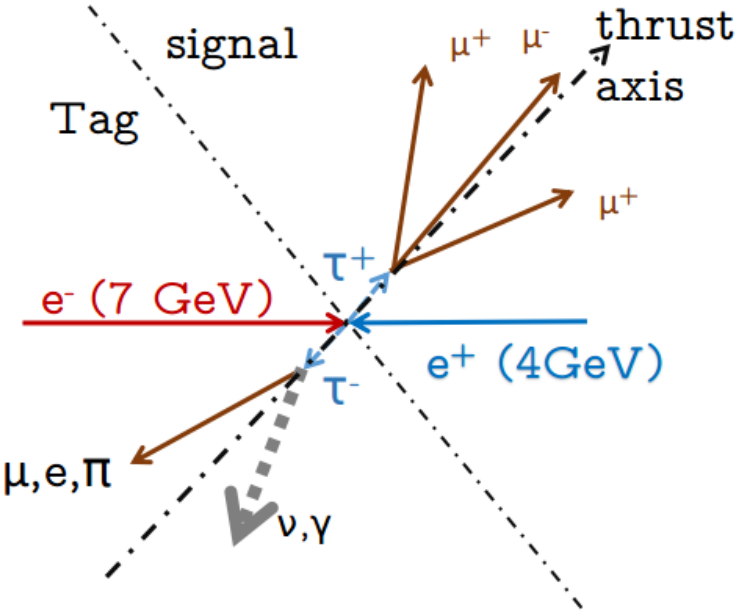

Figure 4.7: Analysis strategy to separate the four charged tracks into the signal and tag sides.

which satisfy $1.65 < M_{\mu\mu\mu} < 1.9\ GeV/c^2$ and $-0.5 < \Delta E < 0.2$ GeV are selected for further studies of event selections and background suppression. Hereafter, the sum of all the physics background is referred backgrounds.

In order to suppress backgrounds in the selected events, at least one charged

track at the signal side is required to be identified as muon with the likelihood ratio $\mathcal{L}(\mu/\pi) > 0.9$. This track satisfies the condition $25 < \theta_{lab} < 145$ degrees. This polar-angle range corresponds to a good region of the KLM (slightly narrower than real KLM acceptance). A priority is set based on momentum of the tracks, from high to low. If the highest momentum track is in the range $25 < \theta < 145$ degrees, muon-ID requirement is applied for this track only, otherwise, muon-ID requirement is applied for both two charged tracks which have the highest and middle momenta. Figure 4.8a shows the $\mathcal{L}(\mu/\pi)$ distribution of the selected track for the signal and the background samples selected with the conditions so far mentioned. The efficiency of this requirement is 90 %. Most of the continuum processes ($udsc$-pair) and $B\bar{B}$ backgrounds are rejected, but there is still a small fraction of those events due to mis-identification of a pion or a proton as a muon, and the decay in flight of pion ($\pi \to \mu\nu_\mu$) and kaon ($K \to \mu\nu_\mu$). Events which a kaon is mis-identified as a muon is rejected by requiring the selected tracks is not identified as kaon with the selection criterion $\mathcal{L}(K/\pi) < 0.9$. Figure 4.8b shows the $\mathcal{L}(K/\pi)$ distribution for the candidate tracks. The number of the signal and background events after each selection step is summarized in Table 4.2.

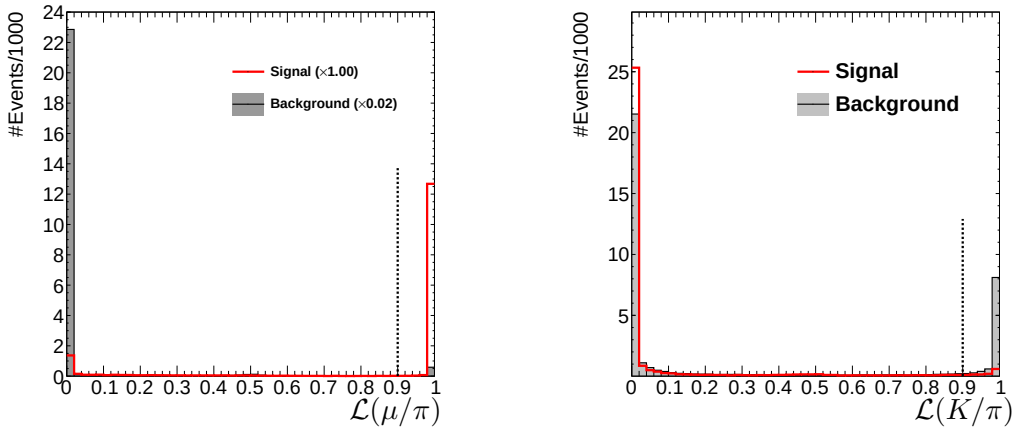

(a) (b)

Figure 4.8: PID likelihood ratio of the selected tracks for the muon-identification. (a) muon likelihood, events with $\mathcal{L}(\mu/\pi) > 0.9$ are selected (the right side of vertical dot-line). (b) kaon likelihood, event with $\mathcal{L}(K/\pi) < 0.9$ are kept (the left side of vertical dot-line).

Table 4.2: The number of remaining events after each selection step for the signal and background samples.

Processes	Generated ($\times 10^6$)	4 tracks &Σcharge = 0 & $1.65 < M_{\mu\mu\mu} < 1.9$ GeV/c^2 & $-0.5 < \Delta E < 0.2$ GeV	Require 1 μ ID
Signal	0.1	32820	29507
$\tau^+\tau^-$	735.2	284310	8069
$B^0\bar{B}^0$	427.68	111	12
B^+B^-	452.32	176	8
$u\bar{u}$	1284	597875	18317
$d\bar{d}$	320.8	122546	3974
$s\bar{s}$	306.4	149687	5066
$c\bar{c}$	1063.2	119248	4329
$\mu^+\mu^-(\gamma)$	400	3538	3522
Bhabha	200	0	0
$e^+e^-e^+e^-$	200	0	0
$e^+e^-\mu^+\mu^-$	400	954	950

4.3 General Selections

After imposing the requirement that at least one charged track in the signal side identified as muon, most of the background events from the $B\bar{B}$, Bhabha and two-photon $e^+e^-e^+e^-$ process are rejected. However, there are still a large number of events from the continuum processes and the $\tau^-\tau^+$ pair where one of pions, kaons or protons is mis-identified as muon. The $\mu^-\mu^+$ pair and two-photon ($e^+e^-\mu^+\mu^-$) processes, where one or two muons and an electron are at the signal side also contaminate as background with some amounts.

The number of photons in the tag and signal sides for the candidate events are counted for background suppression purposes. The photon energy spectra from the τ generic decay at the tag side and from the beam backgrounds are shown in Figure 4.9. There is a huge number of photons from the beam background. Fortunately, their energy is mostly lower than 0.1 GeV. In order to preclude the

huge number of photons from beam background only photons whose energy exceeds the 0.1 GeV threshold are taken into account. Hereafter, the number of photons refers to the photon exceeded the 0.1 GeV.

At most one photon in the signal side is allowed in general selections. This photon may come from the initial state radiation from one of the incoming beam particles or the beam background.

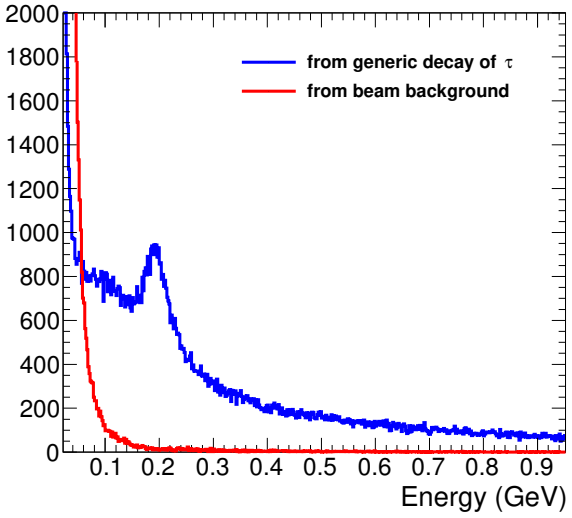

Figure 4.9: Photon-energy spectrum where the red line shows the photon energy distribution from the beam background and the blue line from the decays of τ.

There are always one or two neutrinos which escape from detection in the tag side. From the reconstructed momentum 4-vector of the τ candidates, $\mathrm{P}_{\mu\mu\mu}$ and $\mathrm{P}_{\mathrm{tag}}$, missing momentum 4-vector is defined as:

$$\mathrm{P}_{\mathrm{miss}} \equiv (\mathrm{E}_{\mathrm{miss}}/\mathrm{c}, \overrightarrow{P}_{\mathrm{miss}}) = -\mathrm{P}_{\mu\mu\mu} - \mathrm{P}_{\mathrm{tag}},$$

where $\mathrm{P}_{\mathrm{tag}}$ is the four momentum of the charged particle in case the tag consists of only a leptons or a charged pion, and the sum of the charged track and π^0 or photons ($\mathrm{E}_\gamma > 0.1$ GeV) for case $\rho\nu$ or $\pi\pi^0\pi^0$, respectively, is identified, there. In the signal event $\mathrm{P}_{\mathrm{miss}}$ represents the momentum 4-vector of the missing neutrino

system, with the missing-mass squared:

$$\mathrm{M}^2_{\mathrm{miss}} \equiv \mathrm{P}^2_{\mathrm{miss}}/\mathrm{c}^2.$$

To confirm that the missing system is composed by only neutrinos, the missing momentum 3-vector $\overrightarrow{P_{miss}}$ is required to point into the fiducial volume of the detector, $13 < \theta < 155$ degrees (ECL acceptance).

All the three charged tracks at the signal side are muons, so their energy deposit in ECL crystals should correspond to the minimum ionization penetrating through the 30 cm length of a CsI(Tl) crystal. In some case, a charged track does not have the associated ECL cluster, because it does not reach the ECL or the matching between the track and its cluster is failed. For convenience, the average of the energy deposits in the ECL crystals which are associated to the charged tracks at the signal side is used, $\overline{E_{ecl}^{signal}}$. Its distribution is shown in Figure 4.10. The distribution of the background is wider than that of the signal because the three charged particles are not muons. The condition $0.1 < \overline{E_{ecl}^{signal}} < 0.27$ GeV is imposed to reject background events.

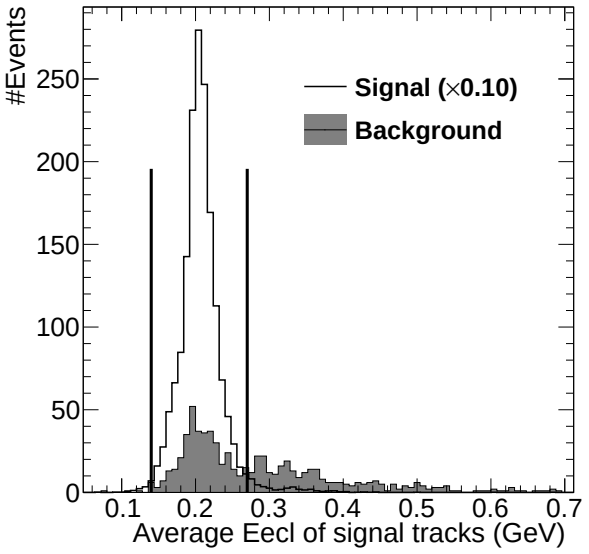

Figure 4.10: Average energy deposit in ECL for the charged particles at the signal side. The two vertical lines indicate the selection region.

4.4 Reconstruction of π^0

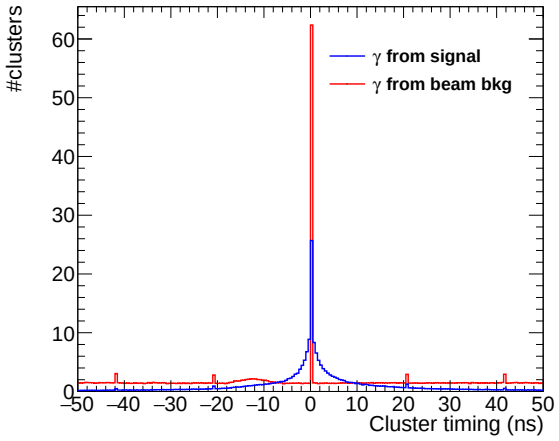

Figure 4.11: Timing distribution of ECL clusters for signal and background photons.

π^0 in the tag side is reconstructed from two neutral ECL clusters in order to divide the hadron tag modes for background suppression. Selection criteria are chosen to maximize the number of reconstructed π^0s. Clusters are required to have $E_\gamma > 75$ MeV or a good shower shape: the ratio of energy deposits in the central crystal (E1) and the sum of the total 9 crystal around (E9), E1/E9, is larger than 0.4 ($E_\gamma > 75$ GeV or E1/E9 > 0.4). Timing of all the clusters is required to be smaller than 20 ns, $|T_{cluster}| < 20$ ns, in order to reject photons from beam backgrounds where $T_{cluster}$ is the timing of the cluster with respect to the trigger timing. $T_{cluster}$ is determined from the waveform fitting [3, 46] and subtracting the time of flight from the IP. The cluster timing distributions are shown in Figure 4.11 for the signal and backgrounds.

The distribution of estimated error for the $\gamma\gamma$ invariant mass, $Err(M_{\pi^0})$, which is calculated from the momentum error of the two clusters is shown in Figure 4.12. It is required to be smaller than 0.01 GeV. The reconstructed invariant mass of π^0 should be in the range $0.09 < M_{\pi^0} < 0.165$ GeV. The π^0 invariant mass distribution is shown in Figure 4.13a for each selection step.

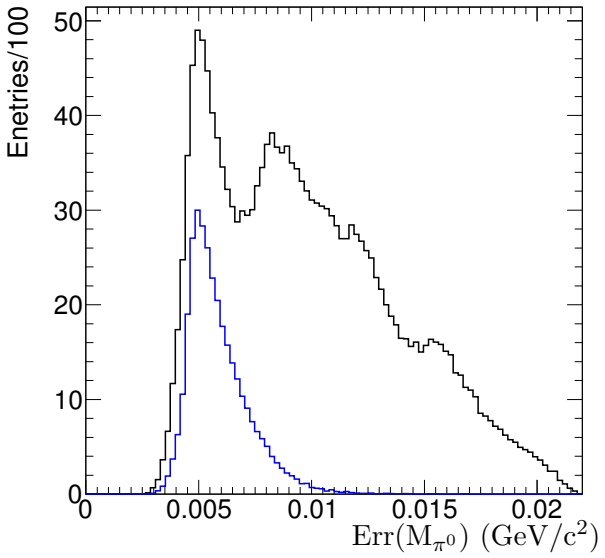

Figure 4.12: The distributions of the estimated error for the reconstructed π^0 mass. The black line is for all the reconstructed π^0 candidates. The blue line is for the true π^0's which match MC information.

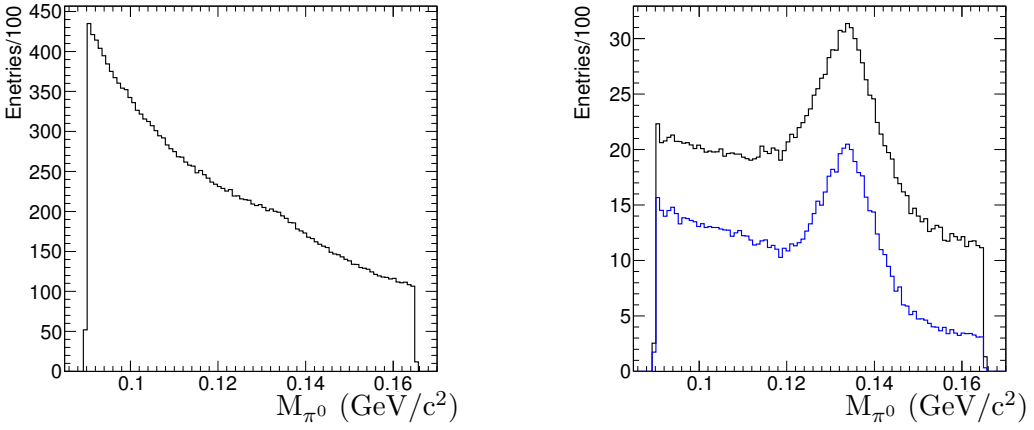

(a) (b)

Figure 4.13: The reconstructed π^0 mass distributions. (a) the distribution before applying the selections, (b) the results after the cluster timing cut $|T_{\text{cluster}}| < 20$ (black histogram) and the additional cut on the mass error Err(M$_{\pi^0}$) < 0.01 GeV applied (blue histogram)

4.5 Background Suppression for Each Tag Mode

After the general selections, the remaining signal candidates are classified into different tag side decay modes to suppress background. Selection criteria are chosen to make sure an event is just only assigned for one tag-side mode. They are summarized in Table 4.3

Table 4.3: Selection criteria to separate tag modes

Tag modes	Branching fraction (%)	Selections
$\tau \to e\bar{\nu}_e\nu_\tau$	17.36	$\mathcal{L}(e/\pi) > 0.1$ and $N_\gamma^{tag} \leq 1$
$\tau \to \mu\bar{\nu}_\mu\nu_\tau$	17.85	$\mathcal{L}(e/\pi) < 0.1$ and $\mathcal{L}(\mu/\pi) > 0.8$ and $N_\gamma^{tag} \leq 1$
$\tau \to \pi\nu_\tau$	10.91	$\mathcal{L}(e/\pi) < 0.1$ and $\mathcal{L}(\mu/\pi) < 0.8$ and $N_{\pi^0} = 0$ and $N_\gamma^{tag} \leq 1$
$\tau \to \rho\nu_\tau$	25.51	$\mathcal{L}(e/\pi) < 0.1$ and $\mathcal{L}(\mu/\pi) < 0.8$ and $\rho^\pm \to \pi^\pm\pi^0$ is reconstructed and $N_\gamma^{tag} \leq 2$
Remaining		Events unsatisfied above selections.

4.5.1 Tag Side: $\tau^- \to \rho^-\nu$

The tag side is assigned to be $\tau \to \rho\nu$, if the charged track is a hadron, and $\rho^\pm \to \pi^\pm\pi^0$ is reconstructed, where a ρ is reconstructed by combining the charged track and a reconstructed π^0. Since there is a huge number of photons from beam background, some additional fake π^0s are also reconstructed. Each π^0 candidates is tried to combine with the charged track to select the best one where the reconstructed ρ mass is the closest to the nominal ρ mass (0.7754 GeV) [44]. The ρ mass distributions for the signal and background events are shown in Figure 4.14. The mass of the reconstructed ρ is required to be in the range $0.35 < M_\rho < 1.13$ GeV/c^2.

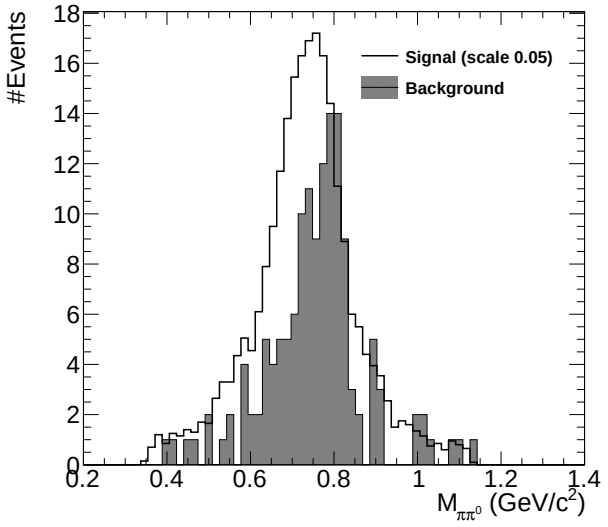

Figure 4.14: Mass distribution of reconstructed ρ for the signal and background events.

The decay mode $\tau^- \to \pi^-\pi^0\pi^0$ may also have ρ as the intermediate state. To separate these two decay modes, the number of photons ($E > 0.1$ GeV) in the tag side is required to be smaller than 3. The number-of-photon distribution is shown in Figure 4.15 for events where a ρ is successfully reconstructed.

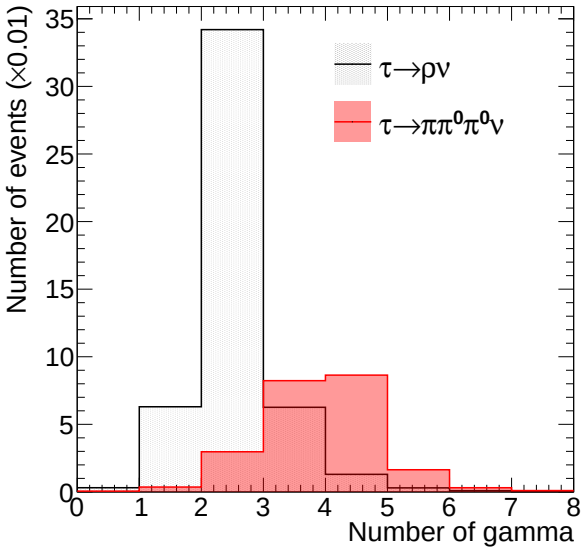

Figure 4.15: Number of photons with $E > 0.1$ GeV in the tag side for the $\rho\nu$ and $\pi\pi^0\pi^0$ tag modes in case a ρ is identified.

The efficiency of these requirements for the $\rho\nu$ tag mode is 50% for the $\rho\nu$ decay events selected by the general selections, and a 16 % fraction of the events selected in this tag mode comes from the other τ decay modes (e.g. including $\pi\pi^0\pi^0\nu$ 6.8% and $\pi\nu$ 3.2%). The efficiency of this tag is low because of the low efficiency of π^0 reconstruction as well as miss-detection of the photons escaping the detector acceptance.

To suppress background, a loose selection for particle ID of the second charged track in the signal side is imposed: with muon likelihood $\mathcal{L}(\mu/\pi) > 0.5$, and not identified as kaon $\mathcal{L}(K/\pi) < 0.5$. Since there is only one neutrino at the tag side in these decays, the missing mass should peak at zero. This nature is useful to reject the background. The scatter plot for the missing momentum and missing

mass squared is shown in Figure 4.16. Events in the region $-0.2 < M^2_{miss} < 0.5$ (GeV$^2/c^4$) and $P_{miss} > 0.25$ GeV/c are selected.

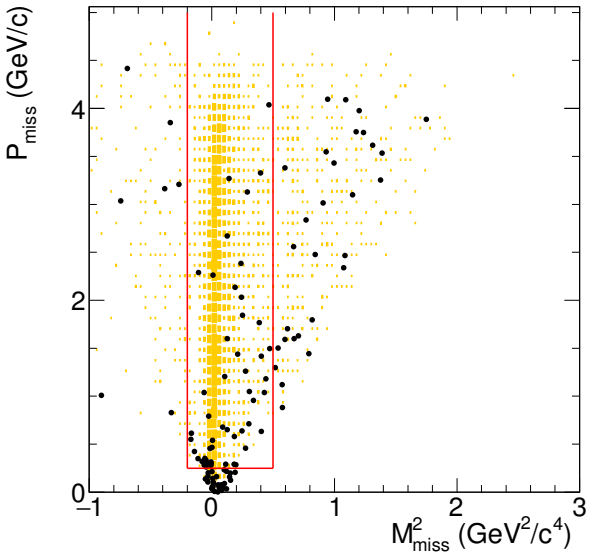

Figure 4.16: 2D plot of the missing momentum and the missing mass squared for the $\rho\nu$ tag mode. The black dots are background events and the yellow boxes are the signal. The red rectangle shows the selection region.

A strong correlation between the missing momentum and the energy of the reconstructed ρ is expected for this tag mode because the missing particle is one neutrino only. Their correlations for the signal and background processes are shown in Figure 4.17. The condition $5.17 < P_{miss} + E_{tag} < 5.35$ GeV is imposed to reject random events; it is the region between two blue lines in the plot.

Figure 4.18 shows the angle between the missing momentum and the momentum of the reconstructed ρ. The angle is required to be larger than 15 degrees and smaller than 80 degrees.

Figure 4.19 is a scatter plot of ΔE vs. $M_{\mu\mu\mu}$. of the $\rho\nu$ tag mode after the selection criteria applied. There are 1868 signal events, and no any background events are remained in the 5σ region. There are 9 background events, but they are located far from the signal region.

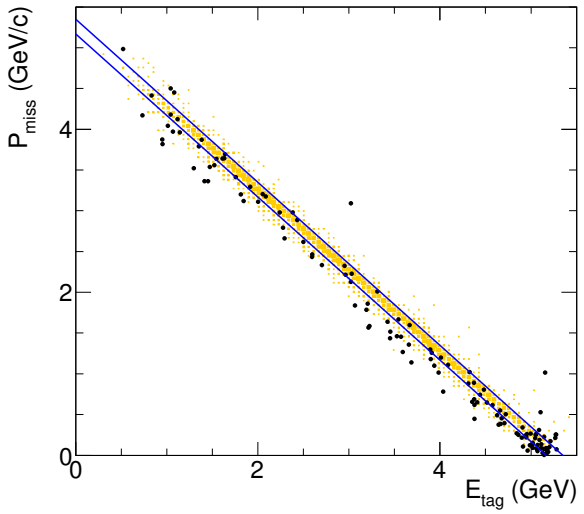

Figure 4.17: Scatter plot for correlation between the missing momentum and the energy of ρ for the $\rho\nu$ tag mode. The events outside the two blue lines are rejected.

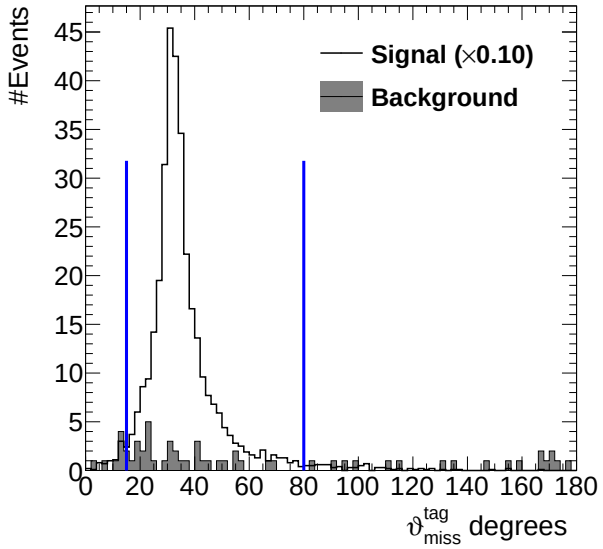

Figure 4.18: Distribution for the angle between the missing momentum and the momentum of the reconstructed ρ. The events in the regions outside the two vertical lines are rejected.

4.5.2 Tag Side: $\tau^- \to \pi^-\nu$

Events are considered as $\pi\nu$ tag mode if the charged track is identified as pion, and there is no reconstructed π^0. The number of photons (E>0.1 GeV) in the tag side is required to be at most one. The energy of this photon is also required to be smaller than 4.5 GeV. The efficiency of this requirement for the $\pi\nu$ mode is 64

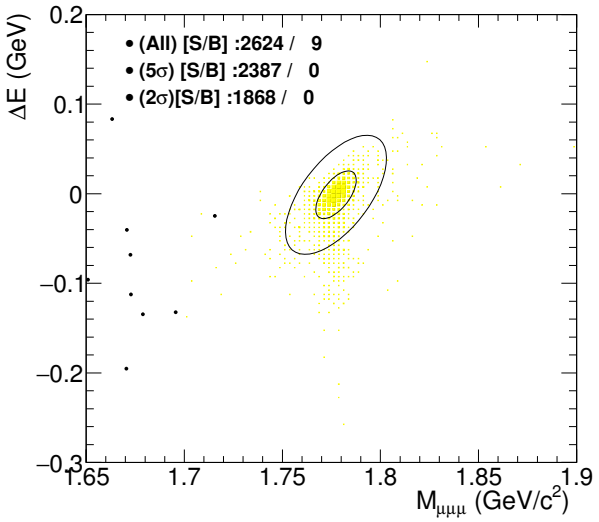

Figure 4.19: Scatter plot of ΔE vs. τ mass $M_{\mu\mu\mu}$ after the selections applied for the $\rho\nu_\tau$ tag mode. The yellow boxes are the signals, and the black dots are background events. The two ellipses correspond to the 2σ and 5σ regions to be of interest, which are used to estimate the efficiency and background.

% for $\pi\nu$ decay events selected by the general selections. It also has efficiency of 24% (16%) for the electron ($e\bar{\nu}_e\nu_\tau$) (muon ($\mu\bar{\nu}_\mu\nu_\tau$)) decay events selected in the same way.

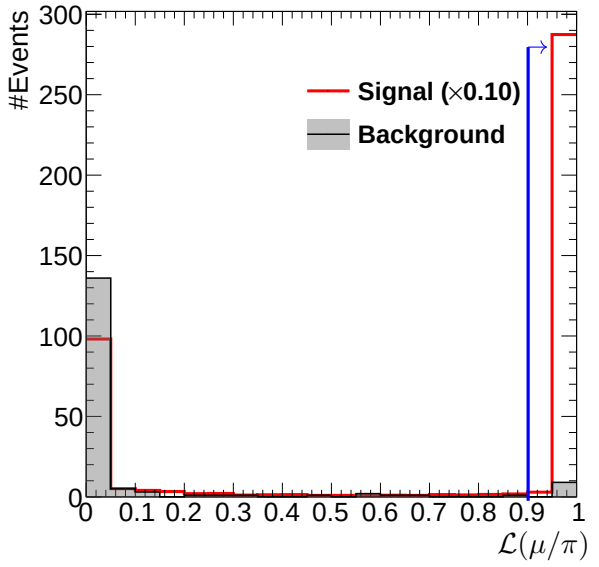

Figure 4.20: $\mathcal{L}(\mu/\pi)$ distribution for the second charged track at the signal side for the $\pi\nu$ tag mode. Events in the left side of the blue line are rejected.

In this hadron tag mode, there is large contamination of continuum processes background. To reject those backgrounds, the second charged track at the

signal side is required to satisfy the muon likelihood, $\mathcal{L}(\mu/\pi) > 0.9$, and it is not identified the kaon or proton, $\mathcal{L}(K/\pi) < 0.9$ and $\mathcal{L}(p/\pi) < 0.9$. The PID likelihood distribution for muon of the second charged track is shown in Figure 4.20.

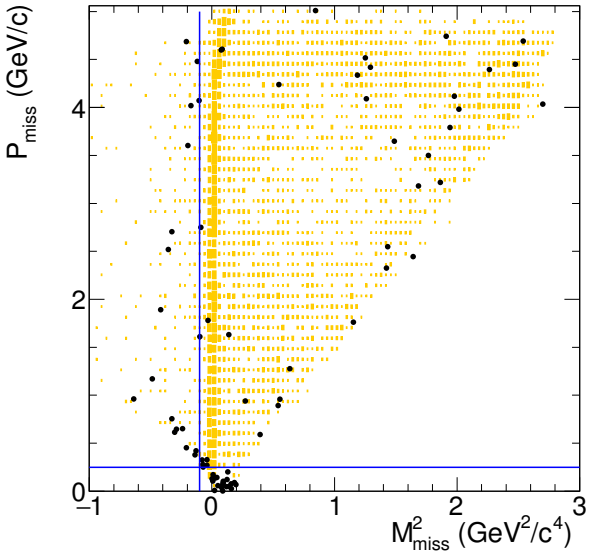

Figure 4.21: Scatter plot of P_{miss} vs. M^2_{miss} for the $\pi\nu$ tag mode. The black dots are background events, and the yellow boxes are the signal. Events inside the upper-right region of the blue lines are kept.

Figure 4.21 shows the scatter plot of P_{miss} vs. M^2_{miss} for the $\pi\nu$ tag mode. Because a large fraction of the electron and muon decay tag mode are mixed in this tag mode, the M^2_{miss} distribution has a long tail to the positive side. In order to keep these events, the selection $M^2_{miss} > -0.1$ GeV$^2/c^4$ and $P_{miss} > 0.25$ GeV/c are imposed only: the positive side of the M^2_{miss} are kept.

The relation between the missing momentum and the tag track's energy is shown in Figure 4.37. It is required to satisfy the condition, $4.95 < P_{miss} + E_{tag} < 5.3$ GeV. The requirement cannot be tight as applied for the ρ tag mode, because the inclusion of events from the lepton tag modes makes the distribution wider.

The result of this tag mode after the above selections applied is shown in Figure 4.23. There are 4663 remaining signal events in total, and 3129 signal events are in the 2σ region. There are still 23 background events, but their mass is lower or higher than the τ mass, and not close to the signal region.

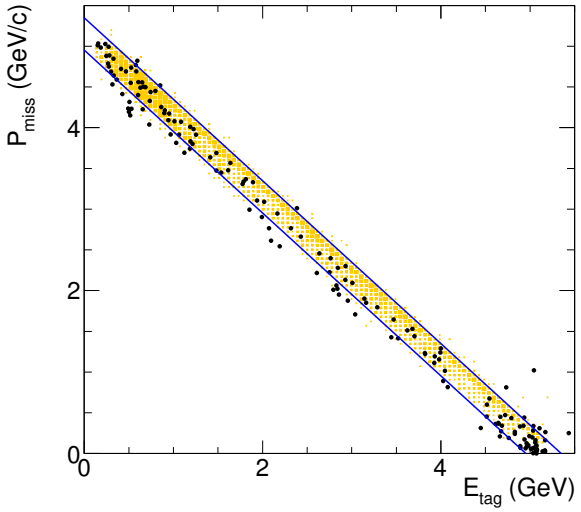

Figure 4.22: Scatter plot of the correlation between the missing momentum and the energy of the tag track for the $\pi\nu$ tag mode. The events outside the two blue lines are rejected.

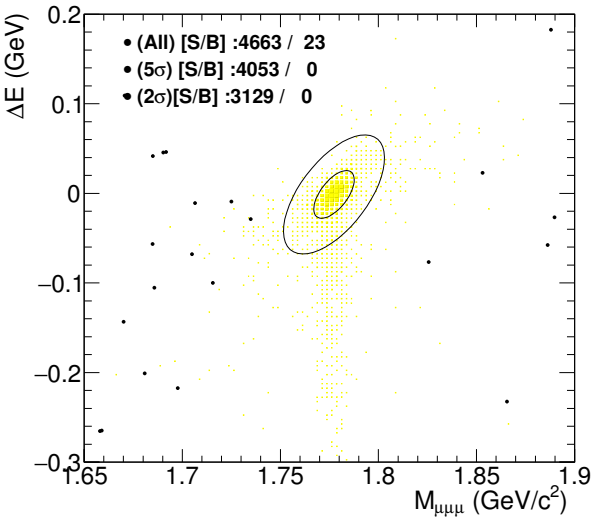

Figure 4.23: Scatter plot of ΔE vs. τ mass $M_{\mu\mu\mu}$ after applied the selections for the $\pi\nu_\tau$ tag mode. The yellow boxes are the signal events, and the black dots are background events. The two ellipses correspond to the 2σ and 5σ regions to be of interest, which are used to estimate the analysis efficiency and background.

4.5.3 Tag Side: $\tau^- \to e^-\bar{\nu}_e\nu_\tau$

The branching fraction of the $\tau^- \to e^-\bar{\nu}_e\nu_\tau$ decay is 17.83 % [44]. Events are identified for this tag mode if the tag track satisfies the electron ID $\mathcal{L}\,(e/\pi) > 0.1$. Maximum one photon is allowed in the tag side. This photon might come from beam background, initial-state radiation of the incoming beam particles or the

final-state radiation of the electron. The distribution for the number of photons in the tag side of the events satisfying $\mathcal{L}(e/\pi) > 0.1$ is shown in Figure 4.24. The efficiency of this tag mode is 78% for the $e\bar{\nu}_e\nu_\tau$ events selected by the general selection. In the selected events for $e\bar{\nu}_e\nu_\tau$ tag mode, there is 5% fraction of $\pi\nu$ decay, where the pion is mis-identified as electron.

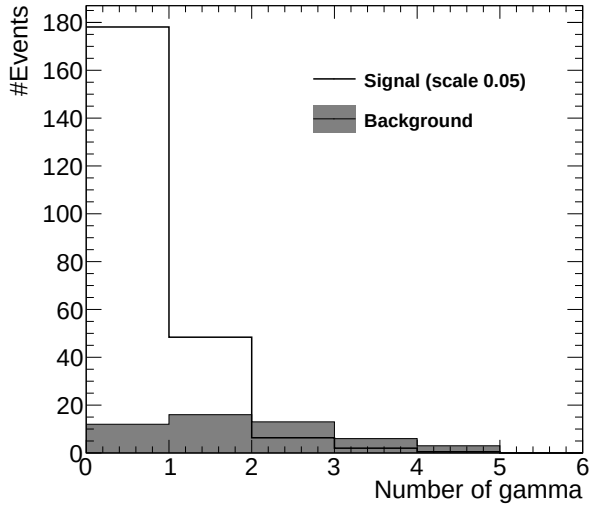

Figure 4.24: Distribution of the number of photons ($E > 0.1$ GeV) in the $e\bar{\nu}_e\nu_\tau$ tag mode selected with the requirement $\mathcal{L}(e/\pi) > 0.1$.

The electron ID is estimated by combining likelihood from information of all the sub-detectors, but mostly based on the ratio of energy deposit in the ECL and the momentum. There are still some mis-identification of pions as seen in Figure 4.25. The signal events are mostly located near the diagonal line, $P_e = E_{ecl}$, so the electron ID condition is tightened with an additional requirement $0.826(E_{ecl}^{tag})^2 - P_{tag} > -0.5$ GeV and $0.75E_{ecl}^{tag} - P_{tag} > 0.1$ GeV. The selected region is limited by a curve and a straight line, respectively, in the figure.

For a further background suppression, the missing momentum and missing mass squared are required to satisfy $P_{miss} > 0.5\,\mathrm{GeV}/c$ and $M^2_{miss} > -0.1\,\mathrm{GeV}^2/c^4$. The scatter plot for P_{miss} vs. M^2_{miss} is shown in Figure 4.26. Because of two neutrinos in the decay, events are widely distributed, and there is no room to tighten the selection.

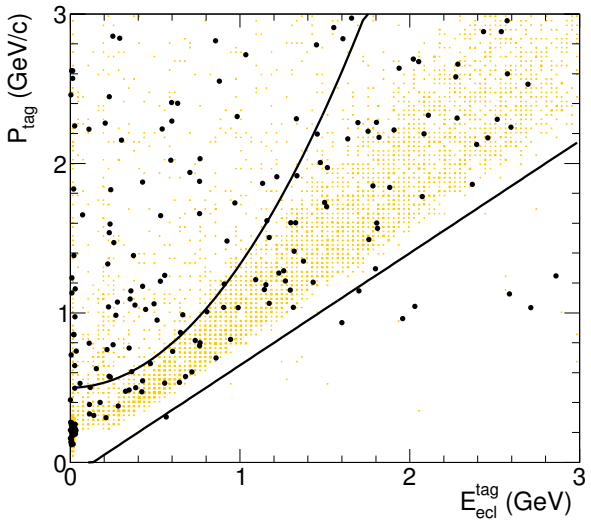

Figure 4.25: Scatter plot of P_{tag} versus E^{ecl}_{tag} for the electron tag mode. The orange-colored boxes show the signal events, and the black dots are the background. The events in the region outside the two black lines are rejected.

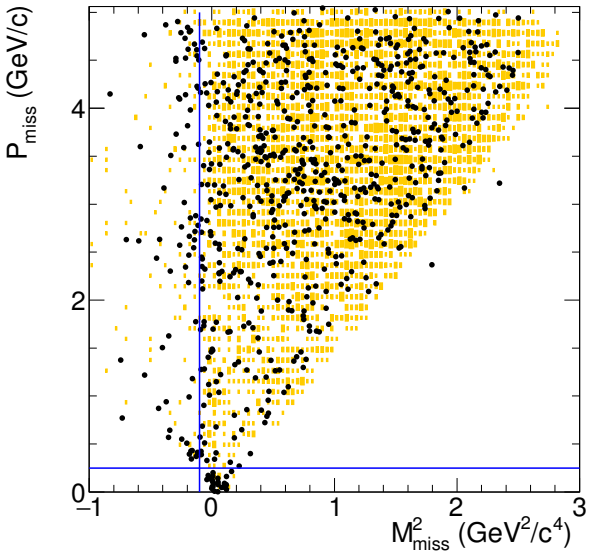

Figure 4.26: Scatter plot of P_{miss} versus M^2_{miss} in the electron tag mode. The orange-colored boxes indicate the signals, and the black dots are the background events. The blue lines indicate the selection region; events at the right-upper side of the lines are selected.

The correlation between the missing momentum and the energy of the tag-side track is shown in Figure 4.27. It is required to satisfy the condition $4.95 < P_{miss} + E_{tag} < 5.3$ GeV, which is indicated by the two blue lines in the figure.

After applied the above selections, there are still background events in the signal region, they need to be rejected. One more charged track in the signal

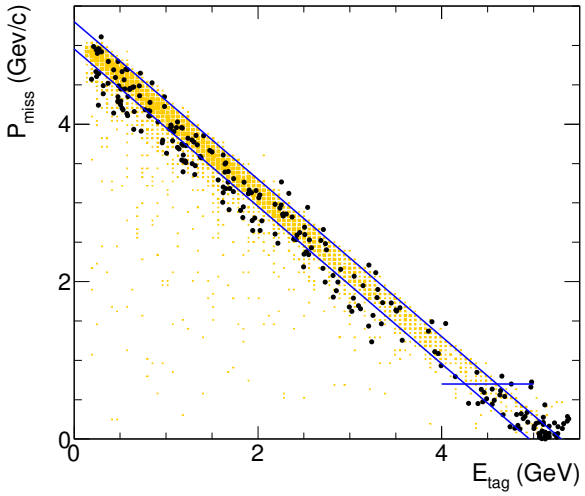

Figure 4.27: Scatter plot for the correlation between the missing momentum and the energy of electron for the $e\bar{\nu}_e\nu_\tau$ tag mode. The events outside the two blue lines are rejected.

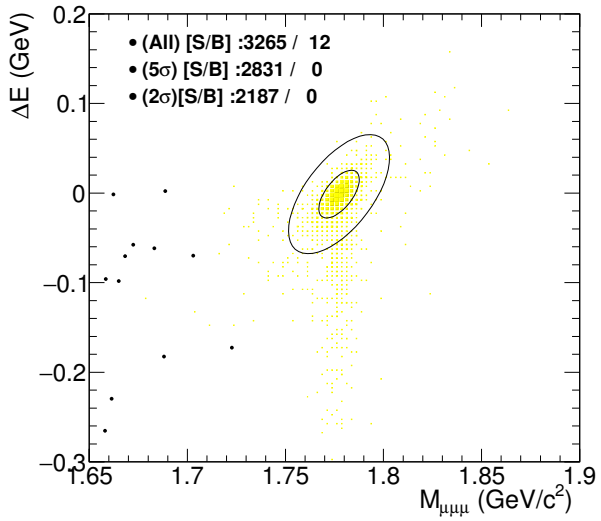

Figure 4.28: Scatter plot of ΔE vs. τ mass $M_{\mu\mu\mu}$ after the selections applied for the $e\bar{\nu}_e\nu_\tau$ tag mode. The yellow boxes are the signals, and the black dots are the background events. The two ellipses correspond to the 2σ and 5σ regions to be of interest, which are used to estimate the efficiency and background.

side is required to be identified as a muon with the condition $\mathcal{L}(\mu/\pi) > 0.9$ and not identified as kaon, $\mathcal{L}(K/\pi) < 0.9$ and proton, $\mathcal{L}(p/\pi) < 0.9$. The remaining events after the above selection criteria applied are shown in Figure 4.28. There are 12 background events, but their mass is smaller than the τ mass, and they are located far from the signal region.

4.5.4 Tag Side: $\tau^- \to \mu^-\bar{\nu}_\mu\nu_\tau$

The branching fraction of the $\tau^- \to \mu^-\bar{\nu}_\mu\nu_\tau$ decay is 17.41% [44]. The tag-side charged particle is identified as muon if $\mathcal{L}(\mu/\pi) > 0.8$ and $\mathcal{L}(e/\pi) < 0.1$. One photon is allowed in the tag side. Efficiency of this tag mode is 72 % for the $\mu\bar{\nu}_\mu\nu_\tau$ decay events selected by the general selections. A fraction of 6% of the events in this tag come from hadron tag modes due the misidentification of pion as muon.

When a photon exists in the tag side, the probability of mis-identification of a pion as muon in both signal and tag sides is large. The second charged track in the signal side is required to be identified as muon with the conditions $\mathcal{L}(\mu/\pi) > 0.9$ and $\mathcal{L}(K/\pi) < 0.9$.

The relation of the missing momentum and the energy of the charge track at the tag side is required to satisfy the condition $4.95 < P_{miss} + E_{tag} < 5.3$ GeV (the same as in the electron tag mode); it is the region between the two blue lines in Figure 4.29.

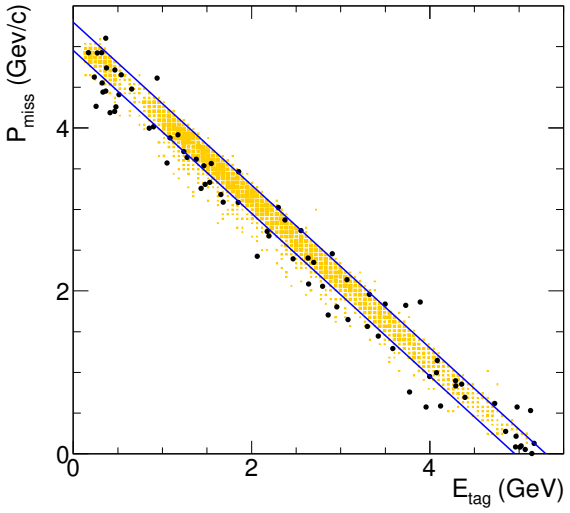

Figure 4.29: Scatter plot for the correlation between the missing momentum and the energy of muon for $\mu\bar{\nu}_e\nu_\tau$ tag mode. The events outside the two blue lines are rejected.

Figure 4.30 shows the scatter plot for P_{miss} vs. M^2_{miss}. The conditions $M^2_{miss} > -0.1$ GeV^2/c^4 and $P_{miss} > 0.5$ GeV/c are imposed as applied for the electron tag mode.

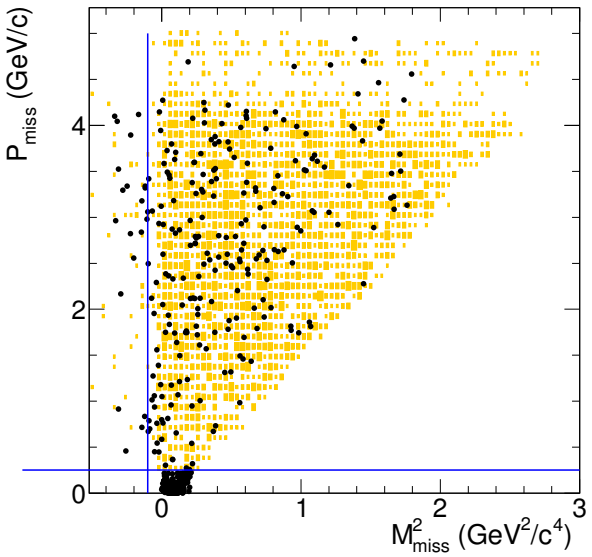

Figure 4.30: Scatter plot of P_{miss} vs. M^2_{miss} for the muon tag mode. The orange-colored boxes show the signals, and the black dots are the background events. Event at the right-upper side of the two blue lines are selected.

The distribution of energy deposit of the tag side track in ECL is shown in Figure 4.31. Since the track is a muon, the energy deposit is expected to be small. $E^{tag}_{ecl} < 0.5$ GeV is imposed.

In the case, an event tagged as the $\mu^-\bar{\nu}_\mu\nu_\tau$ mode, after the above selection criteria applied, there is still backgrounds from: (1) the $\mu\mu\gamma$ process associated with a photon conversion $\gamma \to e^+e^-$ and (2) the two-photon process ($e^+e^- \to e^+e^-\mu^+\mu^-$). In this case, the two charged tracks at the signal side, which do not require muon ID, are an electron and a positron. Assuming the electron mass hypothesis for these two charged particles, the invariant mass of gamma is calculated and shown in Figure 4.32. By imposing a selection $M_{ee} > 0.2$ GeV/c^2, most of these background events are rejected.

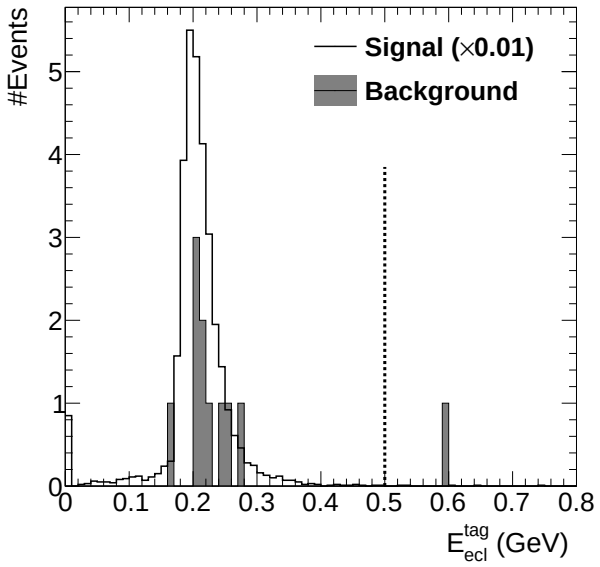

Figure 4.31: Energy deposit in ECL for the tag side charged particle in the muon tag mode.

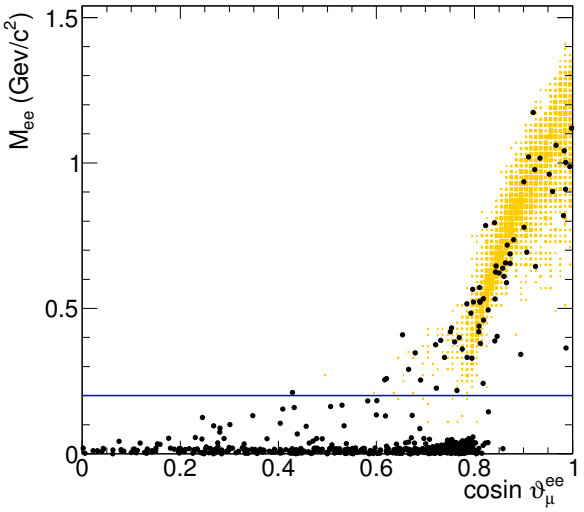

Figure 4.32: Scatter plot for the reconstructed invariant mass by the two particles on which muon ID is not required with electron mass hypothesis, and the angle between the reconstructed momentum of these two particles system, and the momentum of the particle that is identified as muon in the signal side.

The total magnitude of momenta of the four charged tracks in the central of mass system is required to be smaller than 10 GeV/c. Its distribution is shown in Figure 4.33. Since the full energy should be recorded in the two-photon and μ-pair processes, the sum of the momenta should peak at the total beam energy. The energy of each charged track is also required to be smaller than 5 GeV.

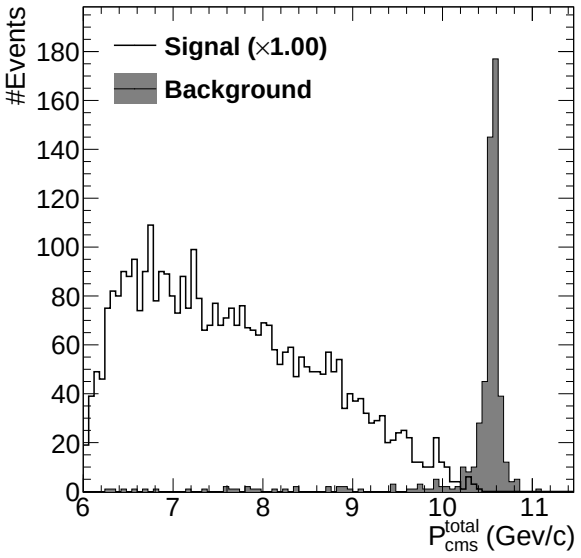

Figure 4.33: The distribution for the sum of absolute momenta over the four charged tracks in the CMS.

After applied these selections, most of backgrounds around the signal region are rejected. The distributions for the signal and background process selected for the $\mu\bar{\nu}_\mu\nu_\tau$ tag mode are shown in Figure 4.34. There is a large fraction of background which comes from the decay $\tau^- \to \pi^-\pi^+\pi^-\nu_\tau$, where π is misidentified as μ. Fortunately, their mass is lower than the τ mass due to a missing neutrino. There is no background event in the region of our interest.

4.5.5 Remaining Tag Mode

The remaining tag-side decay mode includes of $\tau^- \to \pi^-\pi^0\pi^0\nu_\tau$ and $\tau \to \pi\nu_\tau$ and $\tau \to \rho\nu$ in which the ρ reconstruction is failed or there are three or more photons in the tag side. For this tag modes, number of photons in the tag side is not limited. Since the charged track is a pion in this case, and number photons are not limited. There would be a huge continuum process background in which a pion at the signal side is misidentified as muon.

To suppress background events, firstly, the total energy of photons in the tag side is required to be smaller than 4.5 GeV. One more charged track at the

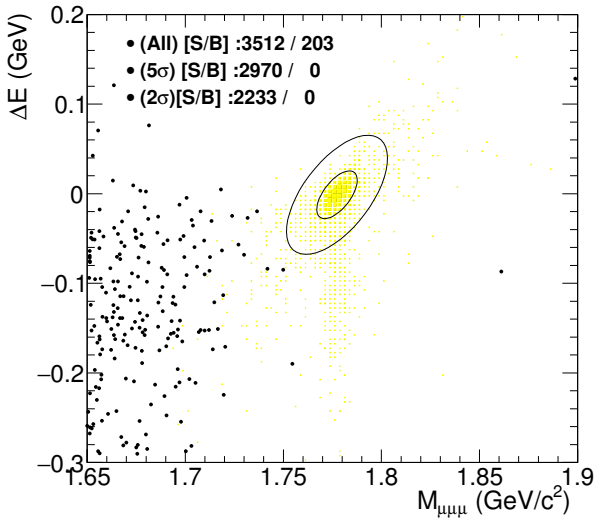

Figure 4.34: Scatter plot of ΔE vs. τ mass $M_{\mu\mu\mu}$ after the selections applied for the $\mu\bar{\nu}_e\nu_\tau$ tag mode. The yellow boxes are the signal, and the black dots are background events. The two ellipses correspond to the 2σ and 5σ regions to be of interest, which are used to estimate the efficiency and background.

signal side is required to be identified as muon with the conditions $\mathcal{L}(\mu/\pi) > 0.9$, $\mathcal{L}(K/\pi) < 0.9$, same as in the electron tag mode. The $\mathcal{L}(\mu/\pi)$ distribution for the second charged track is shown in Figure 4.35.

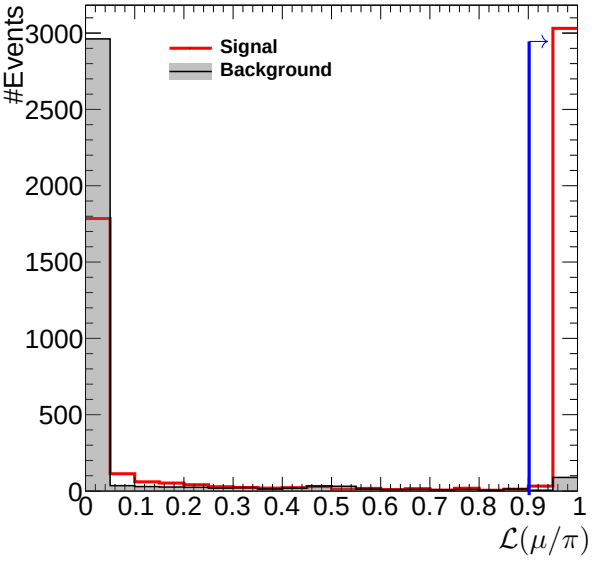

Figure 4.35: Distribution of $\mathcal{L}(\mu/\pi)$ of the second charged track at the signal side for the remaining hadron tag modes.

Figure 4.36 shows the scatter plot of P_{miss} vs. M^2_{miss} after muon ID requirement applied for the second charged track in the signal side. As the remaining

backgrounds have a low missing momentum, those backgrounds are effectively reduced by requiring $P_{miss} > 0.25$ GeV/c and $M^2_{miss} > -0.1$ GeV$^2/c^4$,

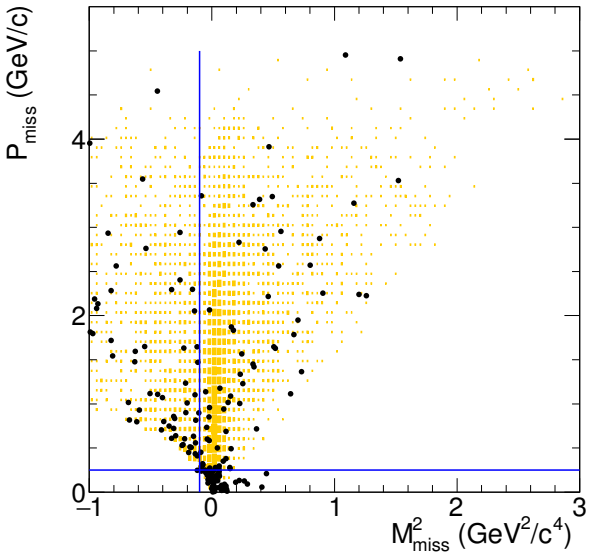

Figure 4.36: Scatter plot of P_{miss} versus M^2_{miss} for the remaining hadron tag mode. The orange-colored boxes show the signals, and the black dots are the background events. The blue lines indicate the selection region; events at the right-upper side of the lines are selected.

Finally, the relation between the visible energy in the tag side and the missing momentum is required to be $5.15 < P_{miss} + E_{tag} < 5.5$ GeV.

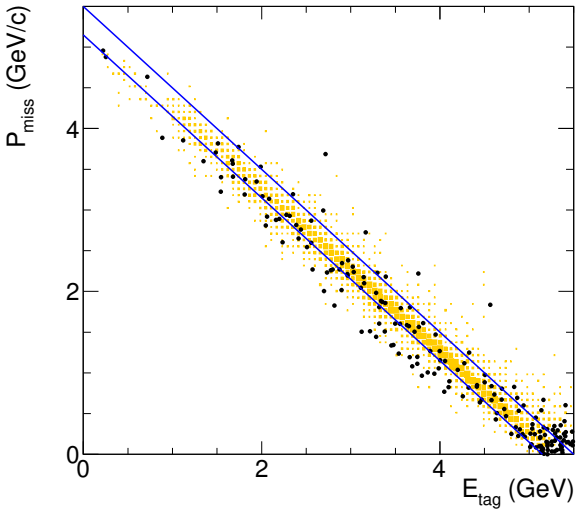

Figure 4.37: Scatter plot for the correlation between the missing momentum and the visible energy for the remaining hadron tag mode. The events outside the two blue lines are rejected.

The result of the ΔE vs. $M_{\mu\mu\mu}$ plot for the remaining hadron tag mode after applied the above selections is shown in Figure 4.38. There are still some background events. They are mostly come from the continuum process and randomly distributed in the signal region. One background event is located inside the 5σ ellipse region.

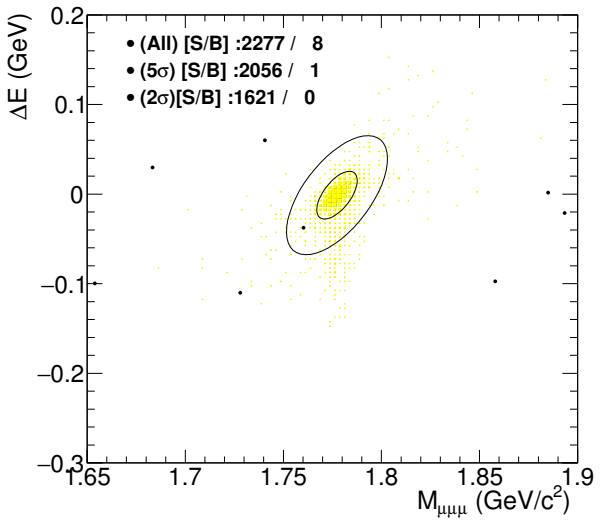

Figure 4.38: Scatter plot of ΔE vs. τ mass $M_{\mu\mu\mu}$ after the selections applied for the remaining hadron tag mode. The yellow boxes are the signals, and the black dots are background events. The two ellipses correspond to the 2σ and 5σ regions to be of interest, which are used to estimate the efficiency and background.

Chapter 5

Signal Analysis

5.1 Invariant Mass $M_{\mu\mu\mu}$ and ΔE

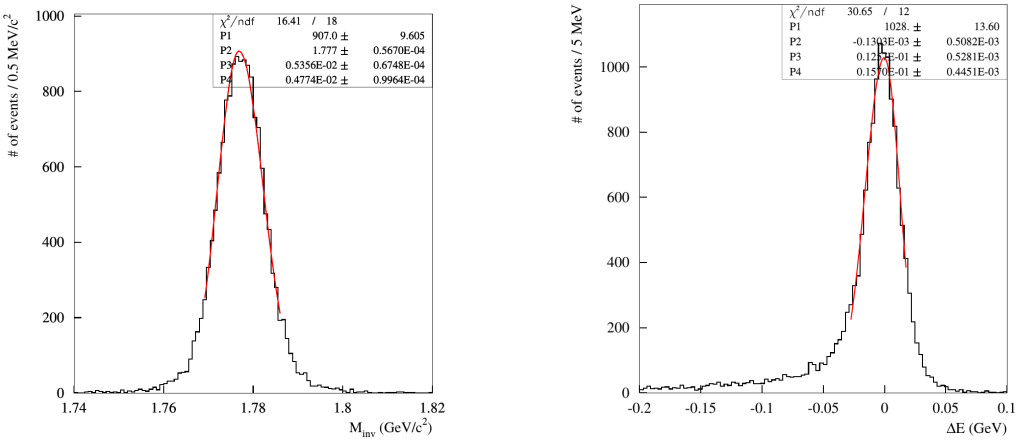

(a) (b)

Figure 5.1: Distributions of the reconstructed invariant mass $M_{\mu\mu\mu}$ of the three muon tracks (a) and ΔE (b) of the Belle experiment. Taken from Ref. [5]

The invariant-mass $M_{\mu\mu\mu}$ and ΔE distributions from the Belle measurement [5] are shown in Figure 5.1. The results of the present study for Belle II is shown in Figure 5.2 with the overlaid fits of peak shape from the Belle results. Since the signal side is fully composed by the three charged tracks, and their momenta are precisely measured by CDC and the vertex detector, a very good mass resolution

is obtained. The distribution of ΔE has a long tail to the negative side because of the initial-state radiation of the incoming beams.

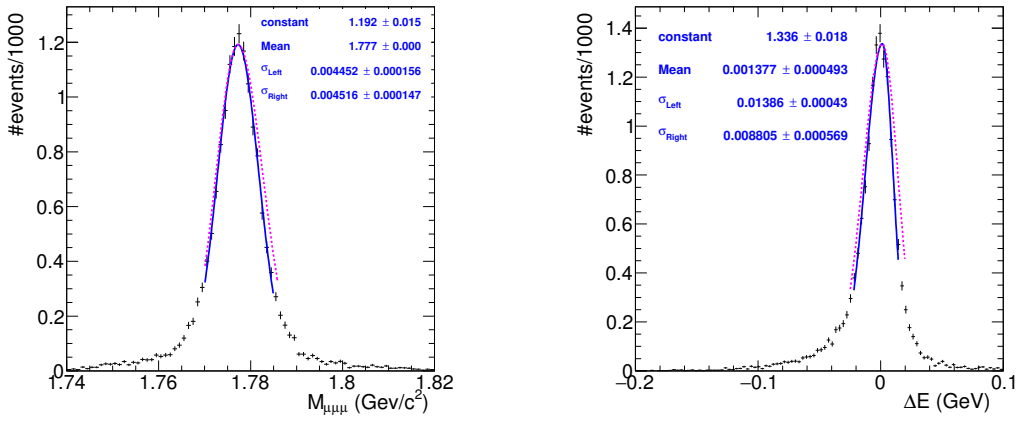

(a) (b)

Figure 5.2: Distributions of the reconstructed invariant mass $M_{\mu\mu\mu}$ of the three muon tracks (a) and ΔE (b) for Belle II (the cross plots). The Magenta lines are the fit results of the corresponding distributions from Belle which are drawn based on the normalization and peak position of the Belle II result.

In order to comparison with the Belle results, each distribution of the Belle II is fitted to an asymmetric Gaussian function for the peak region (the same as that done for the Belle). The results obtained by Belle are superimposed into the Belle II results using the normalization and mean of the distributions obtained by this analysis and the standard deviations from Belle. The results show that the distributions from Belle II are significantly narrower than those from Belle. The details of their numerical values are summarized in Table 5.1. The improvement is about 20% for ΔE and 11% for the invariant mass $M_{\mu\mu\mu}$. This improvement is smaller than that expected from the great improvement of the momentum resolution. It might be due to the impact of the beam-associated backgrounds in Belle II.

Table 5.1: Fit results for the ΔE and $M_{\mu\mu\mu}$ distributions

Parameters	Fitted value		Improvement
	Belle	Belle II	
$M_{\mu\mu\mu}$ distribution (MeV/c^2)			
Mean	1777.0±0.1	1777.0±0.1	
σ_{Left}	4.77 ± 0.10	4.45 ± 0.16	
σ_{Right}	5.36 ± 0.07	4.52 ± 0.15	
$(\sigma_{\text{Left}} + \sigma_{\text{Right}})/2$	5.07	4.49	$\sim 11\%$
ΔE distribution (MeV)			
Mean	-0.13 ± 0.51	1.38 ± 0.49	
σ_{Left}	15.70 ± 0.44	13.86 ± 0.43	
σ_{Right}	12.57 ± 0.53	8.81 ± 0.57	
$(\sigma_{\text{Left}} + \sigma_{\text{Right}})/2$	14.13	11.33	$\sim 20\%$

5.2 Signal Efficiency and Background

The remaining events of signal and background after applied all the selections are shown in Figure 5.3. There are 16341 signal events for 100 000 generated one and 255 background events for 0.8 ab^{-1} MC data. The backgrounds mainly come from two sources: $\tau^+\tau^-$-pair and the continuum $u\bar{u}$ process. The background events from $\tau^+\tau^-$ pair process are dominant. However, they mostly originate from the decay mode $\tau^- \to \pi^-\pi^+\pi^-\nu_\tau$, where a pion is misidentified as a muon. Their reconstructed mass is lower than that of LFV τ decay due to the missing neutrino. The remaining fraction of the $u\bar{u}$ process is small, but they distribute uniformly in the signal window. There is one event in the 5σ region. As can be seen in the previous sections, these events mainly belong to the remaining hadron tag mode. This tag mode contributes a small fraction to the efficiency of whole analysis ($\sim 1.7\%$), its selections can be tighten in the future analyses.

To evaluate the signal efficiency, the signal distribution in the $\Delta E - M_{\mu\mu\mu}$ window is fitted by a bivariate distribution to find the correlation parameters and the width (σ or the standard deviation) of distribution. The distribution has a long tail in the ΔE distribution. Its shape is more sophisticated than a bivariate distribution, However, it is good enough for purpose to roughly find the peak

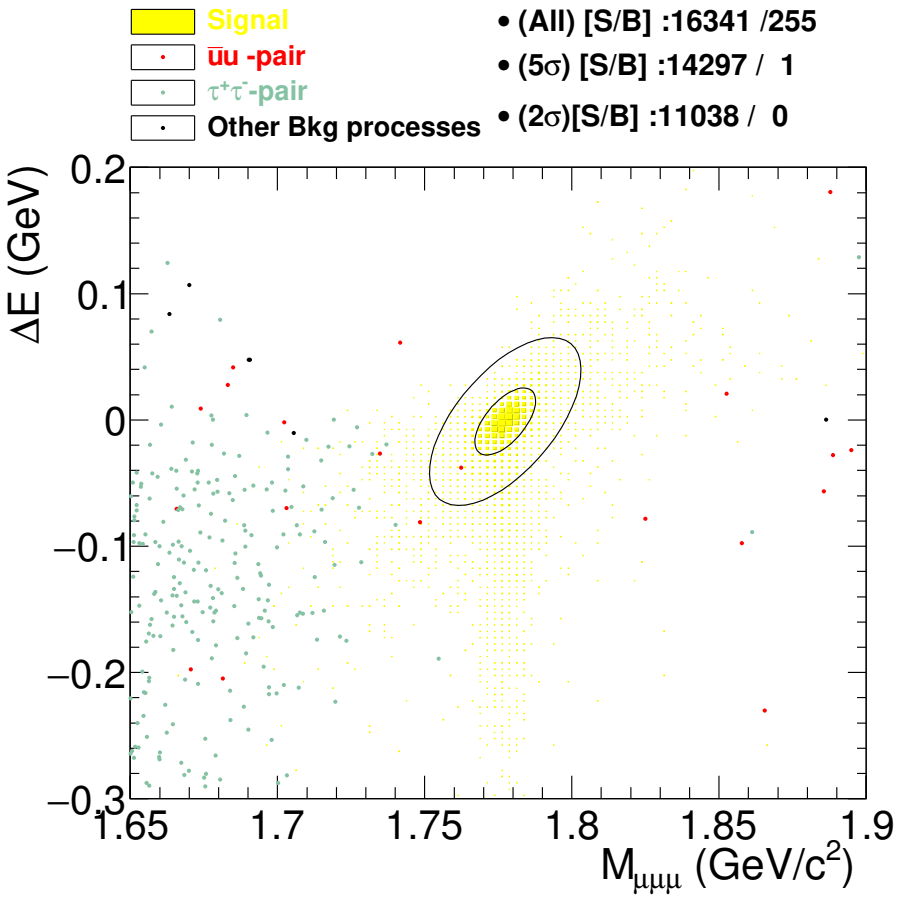

Figure 5.3: Scatter plot of ΔE and τ mass after applying selection criteria

position and the correlation factor (angle of the ellipse). The events in the 2σ region are selected for the signal as indicated by the smaller ellipse in the Figure 5.3. It contains of 11038 events, corresponding to the efficiency 11.04 %. In comparison with the efficiency of the past analysis of the Belle experiment [2], the efficiency of this analysis is 1.5 times better. Although beam background is very high in Belle II, the efficiency is improved significantly with the new selection criteria.

There is no any background event remained inside the 2σ signal ellipse. Assuming the remaining background appear uniformly near the 5σ signal region, the expected number of background events are estimated by loosening the selection criteria for particle ID of the first charged track and the average energy deposit in ECL crystal of the three charged tracks in the signal side. The results are then

propagated to the 2σ signal region with the relation:

$$\mathrm{N}_{\mathrm{bkg}}^{\mathrm{expect}} = \mathrm{N}_{5\sigma}^{\mathrm{tight}} \frac{\mathrm{N}_{2\sigma}^{\mathrm{loose}}}{\mathrm{N}_{5\sigma}^{\mathrm{loose}}},$$

where $\mathrm{N}_{\mathrm{bkg}}^{\mathrm{expect}}$ is the expected background event in the 2σ region, $\mathrm{N}_{2\sigma}^{\mathrm{loose}}$ and $\mathrm{N}_{5\sigma}^{\mathrm{loose}}$ are number of the observed background events in the 2σ and 5σ, respectively, with the loosened selection criteria, $\mathrm{N}_{5\sigma}^{\mathrm{tight}}$ is the number of observed backgrounds in the 5σ region at the final sample. Table 5.2 summarizes the observed background in the 2σ and 5σ regions with the loosened selections. Finally, the expected background in the 2σ region is estimated to be 0.14 ± 0.03 events. It is close to that in the Belle measurement, 0.13 ± 0.06 [2]. This number is scaled to 1 ab^{-1} data by a factor 1.2, the number of expected backgrounds for a 1 ab^{-1} is 0.17 ± 0.04 events.

Table 5.2: Number of expected backgrounds with loose selection criteria

loosened selections	Number of background events		Estimated background
	5σ	2σ	for final result
$\mathcal{L}(\mu/\pi) > 0.9 \to 0.1$	14	1	0.07
$\mathcal{L}(\mu/\pi) > 0.9 \to 0.1$ and E_{ecl}^{sig}	21	3	0.14
$\mathcal{L}(\mu/\pi) > 0.9 \to 0.$	61	9	0.15
$\mathcal{L}(\mu/\pi) > 0.9 \to 0.$ and E_{ecl}^{sig}	175	34	0.19
Average			0.14 ± 0.03

5.3 Upper Limits on the Branching Fraction

The upper limit for the branching fraction of the LFV decay $\mathcal{B}(\tau \to \mu\mu\mu)$ is estimated from the present study using the number of expected background events obtained above, 0.17 ± 0.04 events. The N_{90}^{UL}, the upper limit of the expected signal event in the signal region, is calculated using Feldman-Cousins method [47], for cases in which the number of observed events are 0, 1 and 2. The upper limit on the branching fraction is estimated using following formula:

$$\mathcal{B}(\tau \to \mu\mu\mu) < \frac{N_{90}^{UL}}{2N_{\tau\tau}\epsilon}, \tag{5.1}$$

where $N_{\tau\tau} = 919 \times 10^6$ is the number of $\tau^-\tau^+$ pairs which are produced in a 1 ab^{-1} data sample and calculated using the cross section of the τ pair production with the KKMC (0.919 ± 0.003 nb) [45], and ϵ is the efficiency of the analysis, $\epsilon = 11.04\%$. The upper limits for different numbers of observed events in the 2σ region are summarized in Table 5.3. For the case there is no signal in the 2σ region, the upper limit is set at $\mathcal{B}(\tau \to \mu\mu\mu) < 1.1 \times 10^{-8}$ at 90 % C.L., which is about two times lower than the current limit set by Belle, 2.1×10^{-8} [2].

Table 5.3: The upper limits for $\mathcal{B}(\tau \to \mu\mu\mu)$ with a 1 ab^{-1} data sample estimated for different numbers of observed events in the 2σ region.

Observed events	N_{90}^{UL}	Upper limits
0	2.3	1.1×10^{-8}
1	4.2	2.1×10^{-8}
2	5.7	2.8×10^{-8}

Chapter 6

Conclusions

The calibration and alignment procedures for the Belle II Central Drift Chamber (CDC) have been developed and presented in this thesis. The procedure is validated with both two types of the cosmic-ray data, with and without the magnetic field. This calibration procedure will be used to calibrate the CDC through the Belle II lifetime. The CDC alignment is thus once achieved, but the alignment procedure is still useful in the future for correction of new deformations which may be caused by possible new installation or removal of inner detectors.

The performance of the CDC has been verified with cosmic-ray data taken under a 1.5 T magnetic field. The results before the alignment show that the performance of Belle II is much improved comparing with results of the Belle CDC. After the alignment, the performance of the CDC is greatly improved. This improvement is larger than the expectation from an extrapolation of the Belle CDC results. This proves that our calibration and alignment procedures developed for Belle II is better than that used in Belle. The good performance of the CDC is an important key to obtain good physics results at the Belle II experiment in the future.

An analysis for the lepton flavor violation in decay $\tau^- \to \mu^-\mu^+\mu^-$ is demonstrated using 1 ab^{-1} Monte-Carlo data of the Belle II experiment. The analysis efficiency of 11.04% is achieved for this analysis, about 1.5 times higher than that achieved at Belle (7.6%), even with a huge beam-associated background in Belle II environment. The expected upper limit for the branching fraction is estimated as follows:

$$\mathcal{B}(\tau \to \mu\mu\mu) < 1.1 \times 10^{-8} \text{ at } 90 \text{ C.L.}$$

This is about 2 times lower than that obtained by Belle ($< 2.1 \times 10^{-8}$) [2]. This result is extrapolated to the 50 ab^{-1} data which is planned to be taken in the whole Belle II operation era as follows:

$$\mathcal{B}(\tau \to \mu\mu\mu) < 2.4 \times 10^{-10} \text{ at } 90 \text{ C.L.}$$

With this improvement of the analysis efficiency and a huge planned data of Belle II, we can deeply probe LFV processes in the Belle II experiment. Even if we do not meet the signal, an improvement of the current limit by a factor 100 will be useful to constrain many physics models.

Appendix A

Position Resolution Estimation

(Intrinsic) position resolution, σ, is defined as the standard deviation of the measured drift distance (measurement error) , $\sigma^2 = \mathrm{Var}(\Delta \mathrm{X_{mea}})$. The Belle II track fitting modules [33] can provide both biased and unbiased track fit results for each individual hit. Hence, the position resolution can be calculated from its relations with biased and unbiased resolutions. The biased (unbiased) is the track fitting in which the given hit is included (excluded) in the fit.

The measured, unbiased and biased drift distances are labeled as $\mathrm{X_{mea}}$, $\mathrm{X_{unbiaTrack}}$ and $\mathrm{X_{biaTrack}}$, respectively. The unbiased residual, $\Delta \mathrm{X_{unbia}}$, and biased residual, $\Delta \mathrm{X_{bia}}$, are defined as follows:

$$\Delta \mathrm{X_{unbia}} = \mathrm{X_{mea}} - \mathrm{X_{unbiaTrack}} = \Delta \mathrm{X_{mea}} - \Delta \mathrm{X_{unbiaTrack}}, \tag{A.1}$$

and

$$\Delta \mathrm{X_{bia}} = \mathrm{X_{mea}} - \mathrm{X_{biaTrack}} = \Delta \mathrm{X_{mea}} - \Delta \mathrm{X_{biaTrack}}, \tag{A.2}$$

where $\Delta X_{biaTrack}$, $\Delta X_{unbiaTrack}$, and ΔX_{mea} are the true errors of $X_{biaTrack}$, $X_{unbiaTrack}$ and X_{mea}, respectively. Because X_{mea} and $X_{unbiaTrack}$ are independent, we obtain:

$$\sigma^2_{unbia} = \sigma^2 + \sigma^2_{unbiaTrack} \tag{A.3}$$

For a given hit of a specific track, $X_{biaTrack}$ is weighted mean of $X_{unbiaTrack}$ and X_{mea}:

$$\Delta X_{biaTrack} = \frac{\Delta X_{unbiaTrack} w_{unbiaTrack} + \Delta X_{mea} w_{mea}}{w_{unbiaTrack} + w_{mea}}, \tag{A.4}$$

where $w_{unbiaTrack} = \frac{1}{\sigma^2_{unbiaTrack}}$ and $w_{mea} = \frac{1}{\sigma\prime^2}$ are weights of $X_{unbiaTrack}$ and X_{mea}, respectively; $\sigma\prime$ is the position resolution which is used in track fitting. Replacing $w_{unbiaTrack}$ and w_{mea} in Eq A.4 by σ^2 parameters:

$$\Delta X_{biaTrack} = \frac{\Delta X_{unbiaTrack}\sigma\prime^2 + \Delta X_{mea}\sigma_{unbiaTrack}}{\sigma\prime^2 + \sigma^2_{unbiaTrack}}. \tag{A.5}$$

Next, substituting $\Delta X_{biaTrack}$ in Eq. A.5 to Eq A.2:

$$\Delta X_{bia} = \Delta X_{mea} - \frac{\Delta X_{unbiaTrack}\sigma\prime^2 + \Delta X_{mea}\sigma_{unbiaTrack}}{\sigma\prime^2 + \sigma^2_{unbiaTrack}} = \frac{\sigma\prime^2\left(\Delta X_{mea} - \Delta X_{unbiaTrack}\right)}{\sigma\prime^2 + \sigma^2_{unbiaTrack}}, \tag{A.6}$$

$$\mathrm{Var}\left(\Delta X_{bia}\right) = \frac{\sigma\prime^4}{\sigma\prime^2 + \sigma^2_{unbiaTrack}}\mathrm{Var}\left(\Delta X_{mea}\right) + \mathrm{Var}\left(\Delta X_{unbiaTrack}\right) - 2\mathrm{Cov}\left(\Delta X_{mea}, \Delta X_{unbiaTrack}\right). \tag{A.7}$$

As mentioned above, ΔX_{mea} and $\Delta X_{unbiaTrack}$ are independent, so their covariance is zero, $\mathrm{Cov}\left(\Delta X_{mea}, \Delta X_{unbiaTrack}\right) = 0$. As defined $\mathrm{Var}\left(\Delta X_{bia}\right) = \sigma^2_{bia}$, $\mathrm{Var}\left(\Delta X_{mea}\right) = \sigma^2$ and $\mathrm{Var}\left(\Delta X_{unbiaTrack}\right) = \sigma^2_{unbiaTrack}$. Eq .A.7 is re-written as:

$$\sigma^2_{bia} = \frac{\sigma\prime^4\left(\sigma^2 + \sigma^2_{unbiaTrack}\right)}{\left(\sigma\prime^2 + \sigma^2_{unbiaTrack}\right)^2}. \tag{A.8}$$

Replacing $\sigma^2_{unbiaTrack}$ using the relation in Eq. A.3:

$$\sigma^2_{bia} = \frac{\sigma\prime^4\sigma^2_{unbia}}{\left(\sigma\prime^2 + \sigma^2_{unbia} - \sigma^2\right)^2}, \tag{A.9}$$

$$\sigma_{\text{bia}} = \frac{\sigma\prime^2 \sigma_{\text{unbia}}}{\sigma\prime^2 + \sigma^2_{\text{unbia}} - \sigma^2}. \tag{A.10}$$

For the Belle II CDC, the position resolution calibration is iterated, so $\sigma\prime^2 \sim \sigma^2$, Eq. A.10 becomes:

$$\sigma = \sqrt{\sigma_{\text{unbia}}\sigma_{\text{bia}}}. \tag{A.11}$$

Otherwise, position resolution should be estimated using the formula:

$$\sigma = \sqrt{\sigma\prime^2 \left(1 - \frac{\sigma_{\text{unbia}}}{\sigma_{\text{bia}}}\right) + \sigma^2_{\text{unbia}}}, \tag{A.12}$$

where σ_{bia} and σ_{unbia} are determined from experiment by fitting the biased and unbiased residuals with Gaussian functions.

Appendix B

Magnetic field measurement device

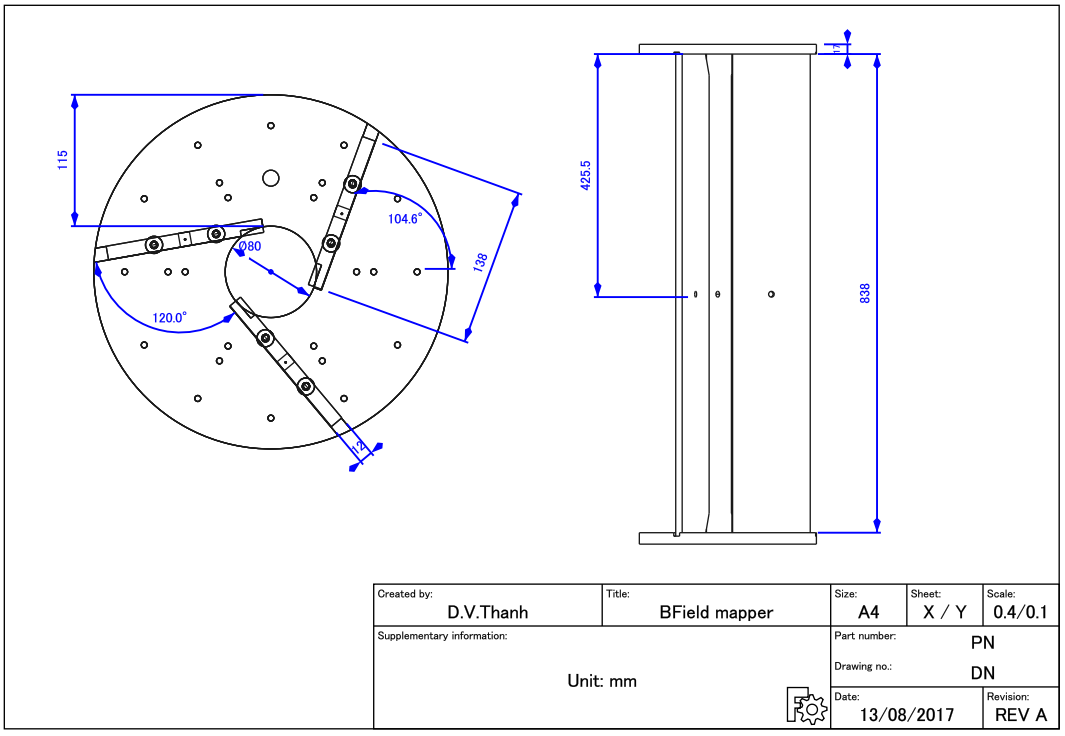

Figure B.1: Drawing of the B-field mapper.

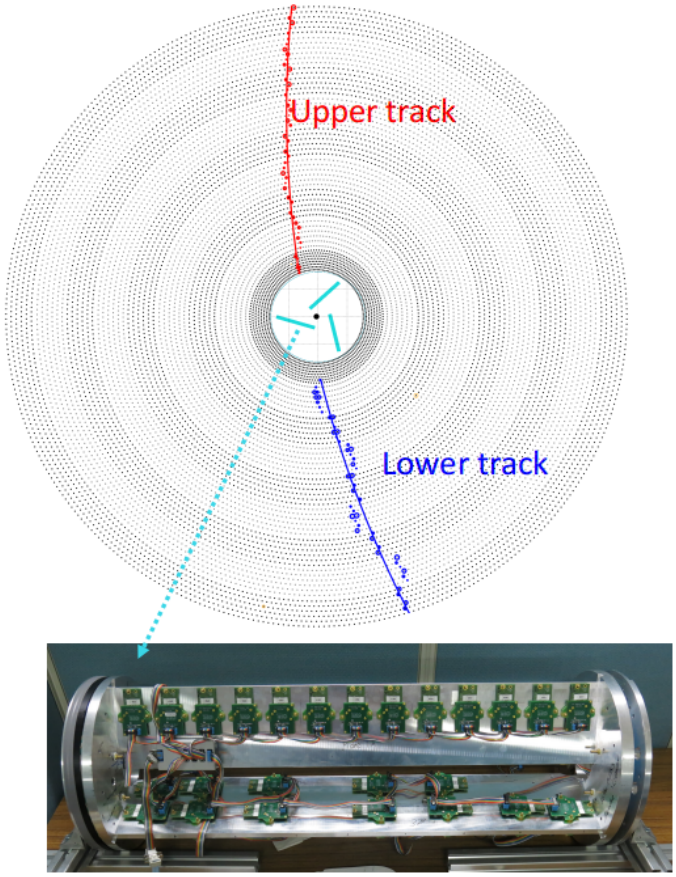

Figure B.2: Photo of the B-field mapper and its position inside CDC.

Bibliography

[1] Y. Amhis, S. Banerjee, et al., Averages of b-hadron, c-hadron, and τ-lepton properties as of summer 2016, The European Physical Journal C 77 (12) (2017) 895. doi:10.1140/epjc/s10052-017-5058-4.

[2] K. Hayasaka, K. Inami, et al., Search for lepton-flavor-violating τ decays into three leptons with 719 million produced $\tau^+\tau^-$ pairs, Phys. Lett. B 687 (2) (2010) 139 – 143. doi:10.1016/j.physletb.2010.03.037.

[3] T. Abe, et al., Belle II technical design report, Tech. rep., Belle II Collobration, arXiv:1011.0352 (2010).

[4] R. Veenhof, Garfield, a drift-chamber simulation program, CERN program library W5050, Ver. 4.29 (nov 1993).
URL http://garfield.web.cern.ch/garfield/

[5] Y. Miyazaki, Search for lepton flavor violating tau decays into three leptons, belle note 1002 (2007).

[6] G. Aad, et al., Observation of a new particle in the search for the Standard Model Higgs boson with the ATLAS detector at the LHC, Physics Letters B 716 (1) (2012) 1 – 29. doi:10.1016/j.physletb.2012.08.020.

[7] S. Chatrchyan, V. Khachatryan, et al., Observation of a new boson at a mass of 125 GeV with the CMS experiment at the LHC, Physics Letters B 716 (1) (2012) 30 – 61. doi:10.1016/j.physletb.2012.08.021.

[8] Y. Fukuda, et al., Evidence for Oscillation of Atmospheric Neutrinos, Phys. Rev. Lett. 81 (1998) 1562 – 1567. doi:10.1103/PhysRevLett.81.1562.

[9] K. S. Babu, C. Kolda, Higgs-Mediated $\tau \to 3\mu$ in the Supersymmetric Seesaw Model, Phys. Rev. Lett. 89 (2002) 241802. doi:10.1103/PhysRevLett.89.241802.

[10] A. J. Buras, B. Duling, T. Feldmann, T. Heidsieck, C. Promberger, Lepton flavour violation in the presence of a fourth generation of quarks and leptons, Journal of High Energy Physics 2010 (9) (2010) 104.

[11] C. Yue, Y. Zhang, L. Liu, Non-universal gauge bosons Z' and lepton flavor-violating tau decays, Physics Letters B 547 (3) (2002) 252 – 256. doi:10.1016/S0370-2693(02)02781-8.

[12] E. J. Konopinski, H. M. Mahmoud, The universal fermi interaction, Phys. Rev. 92 (1953) 1045–1049. doi:10.1103/PhysRev.92.1045.

[13] Q. R. Ahmad, R. C. Allen, et al., Direct Evidence for Neutrino Flavor Transformation from Neutral-Current Interactions in the Sudbury Neutrino Observatory, Phys. Rev. Lett. 89 (2002) 011301. doi:10.1103/PhysRevLett.89.011301.

[14] X.-Y. Pham, Lepton flavor changing in neutrinoless tau decays, Eur. Phys. J. C8 (1999) 513–516. arXiv:hep-ph/9810484, doi:10.1007/s100529901088.

[15] G. Cvetič, C. Dib, C. S. Kim, J. D. Kim, Lepton flavor violation in tau decays, Phys. Rev. D 66 (2002) 034008. doi:10.1103/PhysRevD.66.034008.

[16] R. da Rocha, C. H. Coimbra-Araújo, Extra dimensions at the CERN LHC via mini-black holes: Effective Kerr-Newman brane-world effects, Phys. Rev. D 74 (2006) 055006. doi:10.1103/PhysRevD.74.055006.

[17] S. Chatrchyan, et al., Search for dark matter and large extra dimensions in monojet events in pp collisions at $\sqrt{s} = 7$ TeV, JHEP 09 (2012) 094. arXiv:1206.5663, doi:10.1007/JHEP09(2012)094.

[18] J. P. Lees, et al., Limits on τ lepton-flavor violating decays into three charged leptons 81 (2010) 111101. doi:10.1103/PhysRevD.81.111101.

[19] D. W. Bliss, et al., New limits for neutrinoless tau decays, Phys. Rev. D 57 (1998) 5903–5907. doi:10.1103/PhysRevD.57.5903.

[20] G. Aad, B. Abbott, et al., Probing lepton flavour violation via neutrinoless decays with the ATLAS detector, The European Physical Journal C 76 (5) (2016) 232. doi:10.1140/epjc/s10052-016-4041-9.

[21] R. Aaij, et al., Search for the lepton flavour violating decay $\tau \to \mu\mu\mu$, JHEP 02 (2015) 121. arXiv:1409.8548, doi:10.1007/JHEP02(2015)121.

[22] T. Aushev, et al., Physics at Super B Factory, Tech. Rep. KEK-REPORT-2009-12 (2010). arXiv:arXiv:1002.5012.

[23] S. Hashimoto, et al., Letter of intent for KEK Super B Factory (KEK-REPORT-2004-4).
URL http://superb.kek.jp/documents/loi/img/LoI_accelerator.pdf

[24] P. Raimondi, Status of SuperB effort, talk given at the 2nd SuperB workshop at Frascati, Italia (March 16-18, 2006).
URL http://www.lnf.infn.it/conference/superb06/talks/raimondi1.ppt

[25] S. Kurokawa, E. Kikutani, Overview of the KEKB accelerators, Nucl. Instr. and Meth. A 499 (1) (2003) 1 – 7, KEK-B: The KEK B-factory. doi:10.1016/S0168-9002(02)01771-0.

[26] H. Hirano, M. Akatsu, et al., A high-resolution cylindrical drift chamber for the KEK b-factory, Nucl. Instr. and Meth. A 455 (2) (2000) 294 – 304. doi:10.1016/S0168-9002(00)00513-1.

[27] K. Chaiwongkhot, et al., Inner chamber of the Belle II central drift chamber, in: 2013 IEEE Nuclear Science Symposium and Medical Imaging Conference (2013 NSS/MIC), IEEE, Oct. 27 - Nov. 2, 2013, Seoul, Korea, pp. 1–3. doi:10.1109/NSSMIC.2013.6829461.

[28] T. Uchida, et al., Readout electronics for the central drift chamber of Belle II detector, IEEE Trans. on Nucl. Sci. 62 (4) (2015) 1741–1746.

[29] A. Abashian, K. Gotow, et al., The Belle detector, Nucl. Instr. and Meth. A 479 (1) (2002) 117 – 232. doi:10.1016/S0168-9002(01)02013-7.

[30] T. Alexopoulos, M. Bachtis, E. Gazis, G. Tsipolitis, Implementation of the Legendre Transform for track segment reconstruction in drift tube chambers, Nucl. Instr. and Meth. A 592 (3) (2008) 456 – 462. doi:10.1016/j.nima.2008.04.038.

[31] O. Frost, A local tracking algorithm for the central drift chamber of Belle II, Master's thesis, Karlsruhe Institute of Technology (KIT), http://www-ekp.physik.uni-karlsruhe.de/~thesis/data/iekp-ka2013-6.pdf, IEKP-KA/2013-06 (jun 2013).

[32] J. Lettenbichler, Pattern recognition in the Silicon Vertex Detector of the Belle II experiment, Ph.D. thesis, Vienna University (May 2012).

[33] J. Rauch, T. Schluter, GENFIT – a Generic Track-Fitting Toolkit, Journal of Physics: Conference Series 608 (1) (2015) 012042.
URL http://stacks.iop.org/1742-6596/608/i=1/a=012042

[34] R. Fruhwirth, A. Strandlie, Track fitting with ambiguities and noise: A study of elastic tracking and nonlinear filters, Computer Physics Communications 120 (2) (1999) 197 – 214. doi:10.1016/S0010-4655(99)00231-3.

[35] J. Allison, K. Amako, et al., Recent developments in Geant4, Nucl. Instr. and Meth. A 835 (2016) 186 – 225. doi:10.1016/j.nima.2016.06.125.

[36] S. Shimazaki, T. Taniguchi, T. Uchida, M. Ikeno, N. Taniguchi, M. M. Tanaka, Front-end electronics of the Belle II drift chamber, Nucl. Instr. and Meth. A 735 (2014) 193 – 197. doi:10.1016/j.nima.2013.09.050.

[37] Y. Iwasaki, B. Cheon, E. Won, X. Gao, L. Macchiarulo, K. Nishimura, G. Varner, Level 1 trigger system for the belle ii experiment, IEEE Trans. on Nucl. Sci. 58 (4) (2011) 1807–1815. doi:10.1109/TNS.2011.2119329.

[38] M. Nakao, T. Higuchi, R. Itoh, S. Y. Suzuki, Data acquisition system for Belle II, Journal of Instrumentation 5 (12) (2010) C12004.
URL http://stacks.iop.org/1748-0221/5/i=12/a=C12004

[39] C. Hagmann, D. Lange, D. Wright, Cosmic-ray shower generator (CRY) for Monte Carlo transport codes, in: 2007 IEEE Nuclear Science Symposium Conference Record, Vol. 2, Hawaii, Oct. 27 - Nov. 3, 2007, pp. 1143–1146. doi:10.1109/NSSMIC.2007.4437209.

[40] T. Kuhr, other, The Belle II Core Software, Computing and Software for Big Science 3 (1) (2018) 1. doi:10.1007/s41781-018-0017-9.

[41] V. Cindro, H. Kolanoski, et al., Measurement of spatial resolutions and drift velocities in a drift-chamber filled with a helium-DME mixture, Nucl. Instr. and Meth. A 309 (3) (1991) 411 – 421. doi:10.1016/0168-9002(91)90244-K.

[42] E. Kou, et al., The Belle II Physics Book, KEK Preprint 2018-27, BELLE2-PUB-PH-2018-001. arXiv:1808.10567.

[43] S. Jadach, B. Ward, Z. Was, The precision Monte Carlo event generator KK for two-fermion final states in e^+e^- collisions, Computer Physics Communications 130 (3) (2000) 260 – 325. doi:10.1016/S0010-4655(00)00048-5.

[44] C. Patrignani, et al., Review of Particle Physics, Chin. Phys. C40 (10) (2016) 100001. doi:10.1088/1674-1137/40/10/100001.

[45] S. Banerjee, B. Pietrzyk, J. M. Roney, Z. Was, Tau and muon pair production cross sections in electron-positron annihilations at $\sqrt{s} = 10.58$ GeV, Phys. Rev. D 77 (2008) 054012. doi:10.1103/PhysRevD.77.054012.

[46] C. Hearty, T. Ferber, ECL timing correction and resolution for simulated events in Release-00-07-00, BELLE2-NOTE-TE-2016-006 (2016).

[47] G. J. Feldman, R. D. Cousins, Unified approach to the classical statistical analysis of small signals, Phys. Rev. D 57 (1998) 3873–3889. doi:10.1103/PhysRevD.57.3873.